Fracture Dissolution of Carbonate Rock: An Innovative Process for Gas Storage

TOPICAL REPORT

February 1, 2004 – April 30, 2005

James W. Castle[1], Principal Investigator
Ronald W. Falta[1], Co-Investigator
David Bruce[2], Co-Investigator
Larry Murdoch[1], Co-Investigator
James Foley[1], Graduate Research Assistant
Scott E. Brame[1], Research Associate
Donald Brooks[3], Consultant

[1]Department of Geological Sciences, Clemson University, Clemson, SC
[2]Department of Chemical Engineering, Clemson University, Clemson, SC
[3]DB Consulting, Millington, NJ

May 2, 2005

DE-FC26-02NT41299

Submitted by:
Clemson University
300 Brackett Hall
Box 345702
Clemson, South Carolina 29634

DISCLAIMER

ABSTRACT

The goal of the project is to develop and assess the feasibility and economic viability of an innovative concept that may lead to commercialization of new gas-storage capacity near major markets. The investigation involves a new approach to developing underground gas storage in carbonate rock, which is present near major markets in many areas of the United States. Because of the lack of conventional gas storage and the projected growth in demand for storage capacity, many of these areas are likely to experience shortfalls in gas deliverability. Since depleted gas reservoirs and salt formations are nearly non-existent in many areas, alternatives to conventional methods of gas storage are required. The need for improved methods of gas storage, particularly for ways to meet peak demand, is increasing. Gas-market conditions are driving the need for higher deliverability and more flexibility in injection/withdrawal cycling. In order to meet these needs, the project involves an innovative approach to developing underground storage capacity by creating caverns in carbonate rock formations by hydraulic fracturing and acid dissolution.

The first phase of the project (Budget Period I) involved preliminary geologic and economic analysis of this new method for creating gas storage. The second phase (Budget Period 2), which is discussed in this report, includes analysis and modeling of the processes involved in creating storage capacity, including induced fracturing and acid dissolution of the rock.

Physical and chemical analysis of core samples taken from prospective geologic locations for the acid dissolution process confirmed that many of the limestone samples readily dissolved in concentrated hydrochloric acid. Further, some samples contained oily residues that may help to seal the walls of the final cavern structure. These results suggest that there exist carbonate rock formations well suited for the dissolution technology and that the presence of inert impurities had no noticeable effect on the dissolution rate for the carbonate rock.

A sensitivity analysis was performed for characteristics of hydraulic fractures induced in carbonate formations to enhance the dissolution process. A realistic range of physical parameters for Paleozoic limestone formations at 4000 to 8000 ft depth in the northeastern United States was estimated and used to predict the characteristics of fractures that could be created. Multiple fracture simulations were conducted using modeling software that has a fully 3-D fracture geometry package. The simulations, which predict the distribution of fracture geometry and fracture conductivity, show that the stress difference between adjacent beds is the physical property of the formations that has the greatest influence on fracture characteristics by restricting vertical growth. The results indicate that by modifying the fracturing fluid, proppant type, or pumping rate, a fracture can be created with characteristics within a predictable range, which contributes to predicting the geometry of storage caverns created by acid dissolution of carbonate formations.

The TOUGHREACT simulation code was selected as the optimal simulation package to examine the acid dissolution of limestone. A series of three-dimensional simulations were used to investigate three different dissolution configurations: a) injection into an open borehole with production from that same borehole and no fracture; b) injection into an open borehole with production from that same borehole, with an open fracture; and c) injection into an open borehole connected by a fracture to an adjacent borehole from which the fluids are

produced. The two-well configuration maximizes the overall mass transfer from the rock to the fluid, but it results in a complex cavern shape. We have gained useful insights into the acid dissolution process with the TOUGHREACT simulations so far. During the coming year, we will continue to use this code (with appropriate modifications) to model the dissolution process.

TABLE OF CONTENTS

INTRODUCTION

Currently, natural gas is in high demand in many regions of the United States, especially the Northeast. Hence, there is an increasing effort focused on developing new methodologies that will make natural gas more readily available, which should ultimately reduce the cost of natural gas to consumers. Of particular interest are more efficient and safe means for storing large quantities of natural gas close to major pipelines or high usage areas. The primary focus of this project is to evaluate the feasibility of creating underground natural gas storage capacity in optimal locations via the acid dissolution of carbonate rock formations. The analysis includes compilation of a large amount of data from carbonate formations in six states (Indiana, Ohio, Kentucky, West Virginia, Pennsylvania, and New York), which were selected in consultation with DOE based on location near major natural-gas markets and pipelines.

The basic concept of the fracture and acid-dissolution method is to drill to depth, fracture the carbonate rock layer, and then create a cavern using an aqueous acid to dissolve the carbonate rock. Following waste fluid removal, the resulting cavity can be used as a subsurface natural gas storage reservoir. Abundant carbonate rock formations worldwide make the project worthwhile for the entrepreneur and consumer alike, especially when the facility is to be located near large gas markets where current gas storage capacity is insufficient to meet demand. An additional benefit of the fracturing and acid-dissolution method is its suitability for developing storage capacity of specific volume near industrial facilities or power-generating plants.

The first phase of this project, which was documented in last year's report (Castle et al., 2004a), focused on developing guidelines and a cost estimate for developing gas storage facilities in carbonate rock formations that have negligible innate gas storage capacity (i.e., low permeability and/or porosity). The results showed that hydrochloric acid (HCl) is the most suitable for the proposed cavern creation process. For this reason, our attention focuses entirely on this acid in a carbonate rock. The reaction of HCl with carbonate rocks is well understood. The reaction of limestone with hydrochloric acid is:

$$2HCl + CaCO_3 \Leftrightarrow CaCl_2 + H_2O + CO_2$$

For limestone dissolution, two moles of HCl react with a mole of limestone to produce one mole of calcium chloride ($CaCl_2$), one mole of carbon dioxide (CO_2), and a mole of water. The reaction equilibrium for the above reaction very strongly favors the products, so at equilibrium, the reaction is essentially 100% complete (see, for example, Williams et al., 1979 for calculation method).

In last year's modeling report (Falta et al., 2004), we showed that for every kilogram of limestone that is dissolved, 728.7 g of HCl are consumed, producing 1109 g of $CaCl_2$, 439.7 g of CO_2, and 180 g of water. We also defined the volumetric dissolving power of HCl in terms of the acid strength and limestone density. Using the standard density of limestone of 2710 kg/m^3, and a 30% (by mass) HCl concentration, the volumetric dissolving power is 0.175 (Williams et al., 1979). Therefore, each liter of acid solution is capable of dissolving 0.175 liters of rock. The presence of insoluble residue such as silica affects the dissolution process, and several samples of carbonate formations were tested in the laboratory by conducting dissolution experiments.

We demonstrated that the large mass of CO_2 produced in this reaction is significant in terms of the engineering design of the cavern formation process, and it will be present in the subsurface as a supercritical fluid. The fluid densities will be highly variable during this process, depending on the phase and composition of the fluids. At a pressure of 3000 psi (20.8 MPa), and a temperature of 38 C, the supercritical CO_2 has a density of 863 kg/m^3, and it can dissolve into water at concentrations of 60-70 kg per 1000 kg of H_2O. The injected HCl acid, at a concentration of 30% by weight, has a density of 1149 kg/m^3, and the $CaCl_2$ brine that results from this reaction has a density of 1360 kg/m^3. Because the acid dissolution products (CO_2, H_2O, and $CaCl_2$) all have a lower density than limestone (ρ_{CaCl_2} =2710 kg/m^3), the reaction has the potential to cause very large pressure changes in the subsurface (Falta et al., 2004).

In last year's literature review, we found many studies that focused on matrix acidizing and acid fracturing. While these fields have some relevance to the current project, the goals of matrix acidizing and acid fracturing are much different from our goal of creating a large open cavern. The closest field process to our cavern creation method that is in wide use is solution mining of salt formations. Solution mining of salt formations is used to form cavities for hydrocarbon storage, and to mine the salt itself. In this process fresh water is injected into the formation, the rock salt dissolves, and brine is removed. The dissolution of the salt formation leaves a cavity that can be used for storage (including natural gas storage). We previously showed how a modified version of the DOE T2VOC code (Falta et al., 1995) was capable of accurately modeling the field scale salt cavern dissolution process. In the present report, we use this simulator to investigate three-dimensional rock dissolution patterns in both fractured and unfractured rock formations. As part of the work completed during the past year, the three-dimensional distribution of induced fractures was modeled.

A unique aspect of concentrated (~30%) acid dissolution of carbonates is the large volume of CO_2 that is produced in the reaction. At these high acid concentrations and volumes, this generated CO_2 will form a separate phase that is supercritical at the reservoir temperature and pressure. We are using the new DOE TOUGHREACT code (Xu et al., 2004) coupled with the ECO2 module (Pruess and Garcia, 2002; Xu et al., 2003a,b) to simulate the full geochemical reaction including the supercritical CO_2 phase behavior.

Creating a cavern that will reliably contain compressed natural gas is the primary objective of this research project. To that end, we undertook numerical simulations of the gas storage process in cylindrical caverns to evaluate the sensitivity of the process to formation permeability and gas pressure. These simulations were done using the DOE TMVOC code (Pruess and Battistelli, 2002) that allows for a real gas pressure-volume-temperature (PVT) treatment of methane and other hydrocarbon gases.

RESULTS AND DISCUSSION

Laboratory Testing of Limestone Samples (Task 6)

by David Bruce

In order to gain information about the chemical composition of carbonate rock formations in possible dissolution test sites, samples were collected from core sections maintained by companies, government institutions, and universities (see Table 1.1). Portions of these samples were treated with aqueous hydrochloric acid (35 wt%) in a well ventilated hood so as to ascertain the amounts of dissolvable products. An approximate time for dissolution (corresponding to the point where significant evolution of CO_2 gas ceased) was recorded for each rock sample, shown in Table 1.2, and the undissolved materials were washed with distilled water and dried at 150 °C for 24 hrs. These samples were then reweighed to determine by difference the percentage of carbonate rock (and soluble salts) in the rock samples. During acid treatment and upon drying the samples, it was observed that there were oily residues in several of the samples. Hence, some of the acid treated samples were calcined at 700 °C under a continuous flow of air, so as to determine the amount of organic (i.e., combustible) material in the samples. All of this data is shown in Table 1.3 below.

Table 1.1. Carbonate Core Sample Information

Well ID	County	State	Formation	Comments
Green-6	Greenbrier	WV	Helderberg	Sample taken at 7127-7128
Hamp-12	Hampshire	WV	Knox/ Beekmantown	Sample taken at 10524
Harr-79-HDG	Harrison	WV	Helderberg	Sample taken at 7458
Harr-79-SAL	Harrison	WV	Salina	Sample taken at 7908. Cherty, non-limestone.
Jack-1366	Jackson	WV	Black River	Sample taken at 9304
Lewis-57	Lewis	WV	Helderberg	Sample taken at 6986
Wetzel-408	Wetzel	WV	Big Lime	Sample taken at 1967-1968
8959R	Pike	KY	Big Lime	Sample depth 1888+, cored by United Fuel Gas. Taken at top of formation-visibly sandy
8792	Martin	KY	Big Lime	Sample depth unknown, cored by United Fuel Gas. Taken at top of formation-visibly sandy.

Table 1.2. Aqueous hydrochloric acid dissolution rates for carbonate rock samples.

Sample	Qualitative Dissolution Rates[a]
Lewis-57	inert
Green-6	rapid dissolution
Harr79-HDG	rapid dissolution
Harr-79SAL	inert
8792	moderate dissolution rate (oily residue)
Jack-1366	moderate dissolution rate (oily residue)
Hamp-12	moderate dissolution rate (oily residue)
Wetzel- 408	rapid dissolution
8959R	rapid dissolution

a - rapid dissolution (< 10 min.), moderate dissolution rate (<4 hrs), inert (minimal dissolution after 48 hrs)

Table 1.3. Weight of carbonate core samples before acid treatment, following acid treatment, and following calcination at 700 °C in air.

Sample	Initial Sample Weight (g)	Post Dissolution Results			
		Dried (100°C) Weight (g)	Insoluble (%)	Calcined (700 °C) Weight (g)	Combustible (%)
Lewis-57	53.135				
Green-6	23.8297	2.155	9.0		
Harr79-HDG	34.0793	6.9736	20.5	6.6807	0.9
Harr-79SAL	32.7239				
8792	31.2792	1.0143	3.2	0.9494	0.2
Jack-1366	21.5574	0.3859	1.8	0.3854	0.002
Hamp-12	23.8199	1.2488	5.2		
Wetzel-408	23.7258	7.4959	31.6		
8959R	32.4899	3.1142	9.6		

The acid treatment studies showed that several of the rock samples reacted very aggressively with aqueous hydrochloric acid (e.g., samples Green-6, Harr79-HDG, Wetzel-408, and 8959R). Formations of this type would be ideal for using acid dissolution to generate a gas storage cavern. Other less reactive rock samples included 8792, Jack-1366, and Hamp-12. Two rock samples showed no significant reaction with aqueous hydrochloric acid, specifically, Lewis-57 and Harr-79SAL. These core samples did not contain any significant carbonate rock forms; hence, the carbonate strata at these geographic locations are at depths different from where the samples were collected or the carbonate formations contain appreciable quantities of other rock types (e.g., shale, quartz, etc.).

Analysis of the weight loss data upon acid treatment showed that most of the samples that underwent dissolution had very low concentrations of non-dissolvable

impurities. However, two samples, Harr79-HDG and Wetzel-408, contained moderately large quantities (greater than 20%) of insoluble material. These impurities were present as small particles (less than 1 mm diameter) evenly dispersed in the rock sample; hence, their presence did not inhibit the dissolution of the carbonate rock sample.

In order to ascertain the nature (i.e., structure and composition) of the non-dissolvable components of the carbonate rock samples, the dried, post-dissolution samples were analyzed by powder X-ray diffraction (PXD). PXD experiments were performed on selected samples using a SCINTAG XDS-2000 diffractometer with Cu Kα radiation. The resulting diffraction data were used to ascertain the types of undissolved (following acid treatment) minerals that were present in the carbonate rock samples. The diffraction peaks occurring within the 2-theta range of 10° to 80° were compared to published X-ray diffraction data for product identification purposes. In each case, the primary insoluble component was a form of quartz (SiO_2). Shown in Figures 1.1 and 1.2 are the powder X-ray diffraction patterns for the non-dissolvable components of the two samples (which showed some level of dissolution) that had the highest concentration of impurities, Harr79-HDG and Wetzel-408. It was observed that the sample contained slightly different forms of quartz, which may suggest that there are trace impurity differences between the two core samples, though no effort was made to identify these impurities.

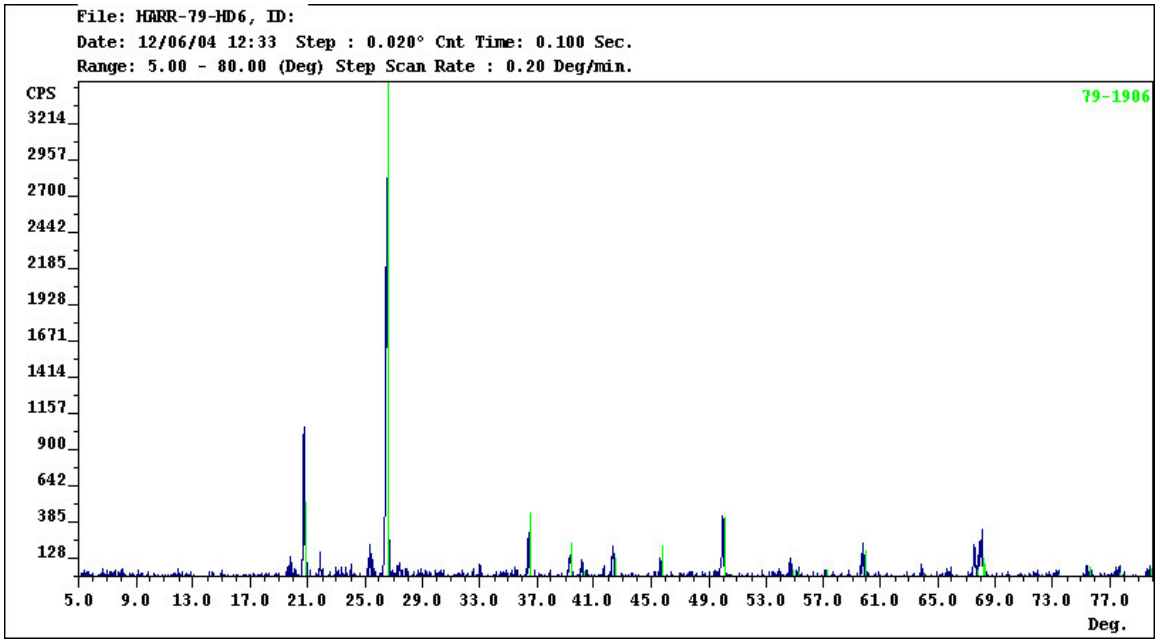

Figure 1.1. Powder X-ray diffraction pattern for quartz (green, reference file 79-1986) and the undissolved components from the acid treatment of rock sample Harr79-HDG.

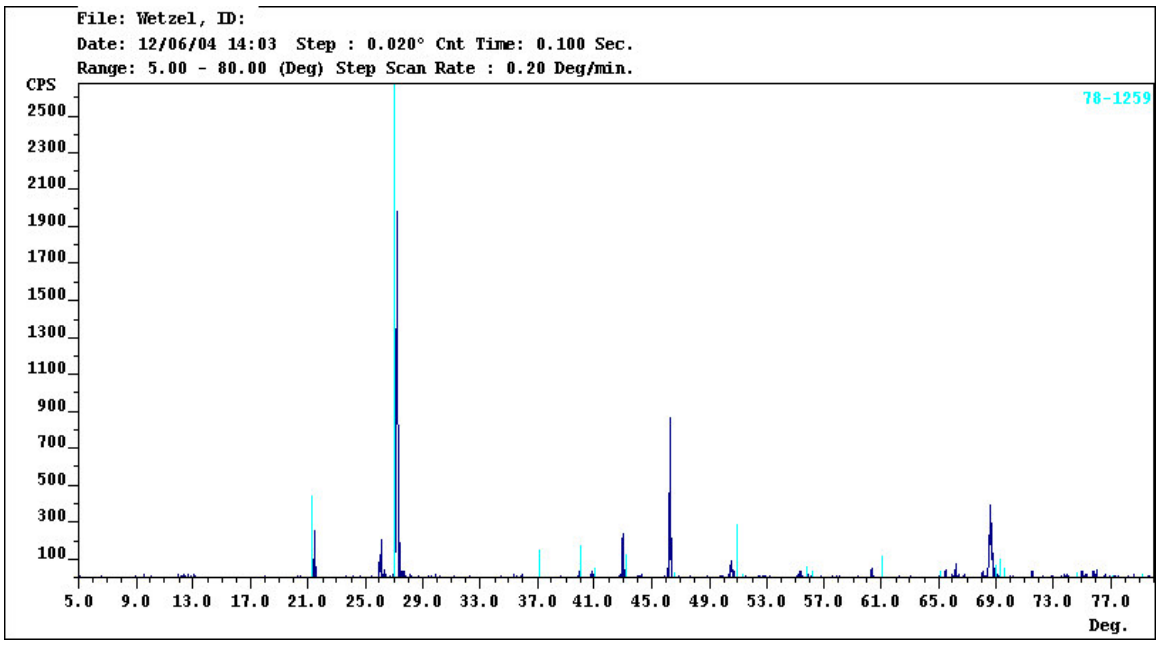

Figure 1.2. Powder X-ray diffraction pattern for quartz (pink, reference file 78-1259) and the undissolved components from the acid treatment of rock sample Wetzel-408.

Three-Dimensional Modeling of Distribution of Induced Fractures (Task 7)

by Jim Foley and Larry Murdoch

Introduction to the Fracture Modeling

Objectives

This report assesses the typical fractures that that would be expected as a result of hydraulic fracturing operations in carbonate formations found in the Appalachian basin. The purpose is to determine the size, shape and fluid flow characteristics of the resulting fracture to predict what could be available to enhance limestone dissolution. Simulations were run using a commercial fracture modeling software, and the results were analyzed to identify the expected range of fracture characteristics as well as the important parameters that influence fracture characteristics.

In practice the process of hydraulic fracturing is quite complicated because of the great number of variables that are involved. Analyzing hydraulic fracture propagation can also be complicated because there are four different types of mechanics that need to be evaluated: solid, fracture, fluid and thermal (Mack and Warpinski, 2000). To address these complications, this report is organized into three sections. Section 1 will present an overview on the inputs and processes of hydraulic fracturing as well as report on the expected physical properties of the limestone of the Appalachian basin. Section 2 presents the methods used to conduct the modeling simulations, and Section 3 presents the results of the model simulations.

Background and Overview

The knowledge that formations could be hydraulically fractured by pressuring wells developed in the 1930's through brine injection wells (Nolte, 2000). The first experimental fracture treatments conducted in the late 1940's lead to the use of sand proppants, which advanced the use of fracturing. By 1955, there were about 3,000 fracturing treatments conducted each month (Nolte, 2000). These initial fracturing treatments were primarily small volume fractures intended to bypass drilling fluid damage to formations.

Beginning in the 1950's there was considerable interest in research projects that advanced fracturing technology. Khristianovich and Zeltov (1955) were to first to demonstrate the coupled relationship of fluid flow to the elastic response of the rock formation. Hubbert and Willis (1957) demonstrated how to define the state of in-situ stress as well as the preference of fractures to propagate in the plane perpendicular to the minimum stress. Howard and Fast (1957) and Carter (1957) provided the framework for the current understanding of leakoff. The basis for contemporary width models began in 1961 when Perkins and Kern published their analysis of radial, penny shaped vertical fractures. They were also the first to consider turbulent flow and non-Newtonian fluids as well as the role of rock toughness. Building on the work of Perkins and Kern (1961),

Nordgren (1972) added leakoff and storage width to fracture models. Together these two papers are the basis of the PKN model. The other significant early work on fracture width modeling was accomplished by Geertsma and de Klerk (1969) by utilizing the Carter equation to include leakoff in the fractures. Their model is known as the KGD model and together with the PKN model, they make up the first generation of fracture models.

The preceding works on fracture modeling lead to a resurgence in the number of fracture treatments conducted and motivated the development of the next generation of fracturing: massive hydraulic fractures. Massive hydraulic fractures (MHF) are designed to increase recovery from tight gas formations. As the name implies, massive hydraulic fracturing involves large volumes of slurry that usually range in size from 100,000 gal to 1 million gal of fluid with over 3 million lbm of proppant (Veatch and Crowell, 1982), with the largest treatments over 7 million lbm (Nolte, 2000). The MHF treatments are designed to create fractures with a half length of at least 1500 ft and a height of about 2000 ft (Randolph, 1976). The cost of MHF treatments can be considerable so modeling is important to optimize their economic effectiveness (Ranostaj, 1976).

The third generation in hydraulic fracturing was the development of Tip-ScreenOut (TSO) designs. *Screenout* is a condition that occurs when the proppant creates a bridge across a restricted flow area, creating a sudden and significant restriction to fluid flow that causes a rapid rise in pump pressure (Marketec, 2005). The goal of the TSO is to create short, very wide, high permeability fractures (Nolte, 2000). The design of TSO involves intentionally screening out the tip of the fracture with sand. This occurs when the slurry is pumped in at a high rate or when the leakoff is high so the fracture tip fills with sand, retarding fracture propagation. Slurry continues to be pumped into the fracture, increasing the fracture width and packing the fracture with proppant to obtain high conductivity (Smith et al., 1987). There are some risks associated with TSO designs. One is early screenout and the other is failure to achieve screenout. Both can cause well damage or undesirable consequences. To avoid this, pretreatment tests need to be conducted to accurately determine fracture design variables (Smith et al., 1987).

With the advent of the three types of fracture methods: damage bypass, massive hydraulic fracture and TSO, a means to predict expected fracture characteristics was needed. Although the PKN and KGD models are effective at predicting some fracture characteristics, both make some significant geometric assumptions that limit the sensitivity of the models. 3D models were developed to address the limitations associated with the 2D models, like PKN and KGD.

Fracture Parameters

One of the main objectives in conducting hydraulic fracturing operations is to design a fracture that optimizes fluid flow to the well, without negatively affecting the integrity of the formation or reservoir. There is a relatively limited amount of control on what can be done to control fracture growth. The primary means of controlling fracture propagation involve choosing (1) the most effective materials (fluids and proppants), (2) the necessary volume of material, (3) the injection rate, and (4) the injection schedule (Veatch, 1983b). In order to effectively identify an optimal fracture design, detailed information about the lithology and fracturing components needs to be utilized. These data include: (1) formation permeability and porosity, (2) static reservoir pressure, (3)

formation temperature, (4) thermal conductivities of formations penetrated, (5) fracture closure pressure, (6) critical net fracturing pressure, (7) formation physical properties: modulus and fracture toughness, (8) fracturing fluid apparent viscosity, (9) fracturing fluid friction data, (10) leakoff coefficient, (11) fluid thermal conductivity, (12) proppant size distribution, (13) proppant density, (14) proppant fracture conductivity as a function of fracture closure stress, proppant type, proppant size distribution, proppant concentration in the fracture, and embedment in the formation, (14) formation embedment pressure, (15) perforation configuration, (16) stratigraphy, and (17) in-situ stresses (Veatch, 1983a; Veatch et al., 1989).

Models

Models have been created to integrate critical formation data and predict fracture geometry and aid in fracture design. There are four primary reasons that hydraulic fracturing models have been developed and used: (1) to simulate fracture geometry and proppant placement; (2) to design a pumping schedule; (3) evaluate how hydraulic fractures affect well performance, and (4) to perform an economic optimization (Mack and Warpinski, 2000). There are three main geometric categories of fracture models: two-dimensional (2D) models, pseudo three dimensional (P3D) models, and fully three dimensional (3D) models.

2D Models

There are two types of 2D models, the KGD that expresses fracture width in terms of height and the PKN that expresses fracture width in terms of length (Veatch et al., 1989). The KGD assumes that the vertical cross section perpendicular to flow is rectangular, whereas the horizontal cross section is elliptical (Figure 2.1). The vertical change in fracture width occurs more gradually than the horizontal change in width. The fracture cross section in the PKN model is elliptical perpendicular to flow (Figure 2.2) and it maintains this shape to the fracture tip. The width varies as a function of the horizontal pressure gradient away from the well (Mendelsohn, 1984a). Fractures calculated using the PKN models generally have smaller widths and are significantly longer than the fractures computed with the KGD model (Veatch, 1983a; Veatch et al., 1989).

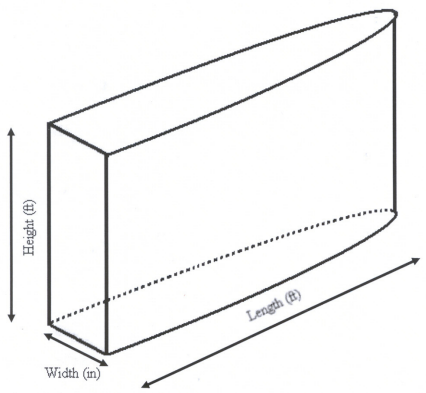

Figure 2.1 KGD idealized fracture geometry

The 2D models represent the first generation of fracture models and they assume that the height is constant and the fracture only varies in length and width (Veatch et al., 1989). There are also a number of other assumptions: the fractures are planar and perpendicular to the minimum stress, fluid flow is laminar; leakoff is a simple function derived from filtration theory and the fracture propagates in a continuous, homogeneous isotropic linear elastic solid (Geerstma and de Klerk, 1969; Mack and Warpinski, 2000). The major limiting factor of the 2D models is the assumption that the fracture height is constant. In order to account for vertical fracture growth, 3D models were developed.

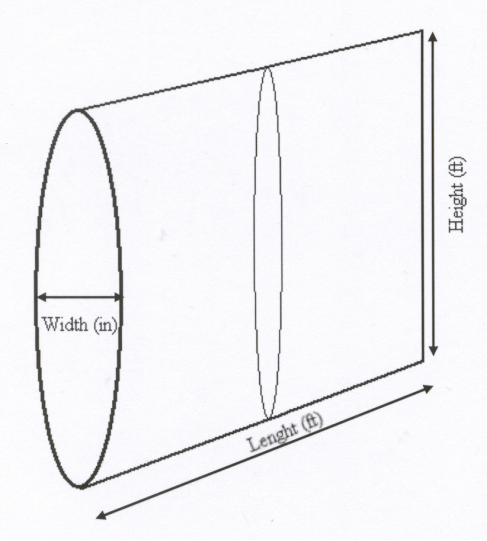

Figure 2.2 PKN Fracture geometry

P3D Models

P3D models attempt to account for the vertical variations in the formation parameters by utilizing approximation techniques. There are two types of P3D models, elliptical and cell-based (Mack and Warpinski, 2000). The elliptical models assume a vertical profile consisting of 2 half ellipses joined at the center. Horizontal length and vertical growth at the wellbore are calculated at each time step and the assumed ellipse is matched to these calculations (Mack and Warpinski, 2000; Mendelsohn, 1984b). Cell-based models assume that the fracture is forming in a grid of connected cells. There is no defined shape for the fracture as the shape is generated based on the calculations in each cell block. Cell-based models do not fully couple variations in fluid flow calculations to the fracture geometry calculations (Mack and Warpinski, 2000).

There are two major simplifications inherent in P3D models. One is that they ignore vertical fluid flow in the fracture. The other is that they do not consider the 3D elastic response of the formation as the horizontal length increases (Mendelsohn, 1984b). P3D models are an improvement on fixed height 2D models and are faster than fully 3D models, but lack the robust computations preformed by fully 3D models.

Fully 3D Models

Fully 3D fracture geometry models consist of state-of-the-art computer codes to calculate full 2D fluid flow in the fracture coupled to the 3D response of the rock formation. The coupling process is why 3D fracture models are quite complex. The simulations simultaneously solve for the shape of the fracture, the width profile of the shape generated and the fluid flow in the fracture that results from changes in geometry of the fracture (Mack and Warpinski, 2000). In order to simultaneously solve these problems, a 3D boundary element code, finite element code or implicit finite difference calculations are used to determine an influence matrix to relate fracture openings to fluid pressure in the fracture.

The discrete elements utilized by the boundary element codes solve a series of governing equations to calculate the fracture characteristics. The governing equations consist of (1) elasticity equations to relate pressure to width, (2) fluid flow equations that relate the flow of the slurry to pressure gradients in the fluid and (3) equations of fracture criteria that relate the stress intensity at the fracture tip to the critical intensity necessary to fracture the rock (Clifton, 1989). The governing equations utilize all of the input parameters listed above to predict fracture characteristics. Fully 3D models allow for predictions of fracture geometry in complex geological situations where the fracture penetrates layers of different lithology from the target formation. While the models are computationally demanding, advances in computer technology have allowed fully 3D models to become available for use on personal computers.

Review of Commercial Model Software

Eight commercially available codes were investigated as possible options for the project. The different codes had a variety of features and capabilities as well as a range of cost availability. The commercially available codes investigated include: StimPlan, FracCADE, TerraFRAC, @Frac, Taurusrs, MFRAC, GOHFER, and HyfracP3D. After reviewing the programs listed, StimPlan from NSI Technologies Inc. was selected to run the simulations. This program is an advanced software package with great versatility, and was the most economic choice.

StimPlan

STIMPLAN is a state-of-the-art 3D hydraulic fracture simulator for complex situations as well as a complete design tool kit produced by NSI Technologies Inc. of Tulsa Oklahoma (Warpinski et al., 1994; NSI, 2004a). The software package offers fully 3D fracture geometry solutions in layered environments, pseudo-3D numerical fracture modeling, 2D quick simulations, 2D numerical multi-phase flow, and can simulate the simultaneous growth of multiple fractures at different intervals. StimPlan incorporates numerical modeling technology with gridded fracture models to calculate fracture geometry in layered formations. Implicit finite difference calculations are used to solve equations of mass balance, height growth, and fluid flow. Fracture width is simulated through finite element calculations. Fluid flow and proppant transport in the fracture is calculated using 2D numeric multi-phase flow solutions. StimPlan also has the capability of simulating acid fractures and designing pump schedules. It includes a database of properties for fracturing fluids and proppants and offers data handling and analysis capabilities.

MFRAC

MFRAC is a 3D fracture simulator that is the core of a suite of software packages produced by Meyer and Associates, Inc. of Natrona Heights, PA. MFRAC features 3D fracture geometry with fully coupled proppant transport, integrated acid fracturing, pumping schedule design, multilayer fracturing, options for 2D solutions, simulation of horizontal fractures, and a database of proppant, fluid and rock properties (Meyer, 2004). The fracture simulator calculates fracture length, height, width and geometry parameters

as a function of time (Warpinski, et al., 1994). MFrac is a sophisticated and robust fracture simulator package.

GOHFER

GOHFER is a 3D planar fracture propagation and slurry transport simulator produced by Core Laboratories. GOHFER (Grid Oriented Hydraulic Fracture Extension Replicator) is a simulator that models proppant transport, acid fractures, multiple fractures, simulates fractures from horizontal and asymmetric wells, and can account for vertical and lateral variations in leakoff (Benson, 2004). The model is based on a regular grid structure to calculate elastic rock displacement and fluid flow solutions. Simulations are calculated by assigning each grid values for important parameters. Displacement of the fracture face at the nodes is determined by an integration of the pressure distribution over each node (Warpinski et al., 1994).

TerraFRAC

TerraFRAC is a 3D numerical software package for modeling and solving hydraulic fracturing, waste disposal and cuttings re-injection problems. The software is produced by TerraTek Inc. of Salt Lake City, UT. The program is also capable of solving complicated and non-standard fracturing treatments, including fractures in dipping layers with high stress contrast, and proppant or cuttings transport (Terratek, 2004). The drawbacks of this code are that it lacks a pumping schedule design option.

FracCADE

FracCADE is a hydraulic fracturing code available from Schlumberger as part of CADE Office, an integrated suite of engineering applications for well construction, production and stimulation (Schlumberger, 2004). The program features pseudo-3D and 2D numerical models that can model propped and acid hydraulic fractures FracCADE has the ability to predict the simultaneous growth of multiple fractures at different intervals as well as design capabilities for pump schedule generation. One of the drawbacks of this program is that it lacks fully 3D geometry simulations.

Frac3D

Frac3D is a three-dimensional finite element based fracture analysis program designed to model structural engineering problems. The software is produced by Lehigh University of Bethlehem, PA. The current version of the program is capable of conducting several structural analyses: (1) regular 3-D stress analysis, (2) 3-D fracture analysis, (3) stress and fracture analysis under "Generalized Plane Strain" conditions and (4) non-linear analysis of solid structures (for small strain plasticity) (Hu and Neid, 2003). While the program is capable of calculating a variety of 3D fracture geometries, there are some limitations that inhibit the applicability of the program to this project. The program lacks the ability to calculate multi-phase fluid flow, proppant transport, post-fracture fluid flow, acid fracturing, and fractures in complex geologic stratigraphy.

@FRAC

@FRAC is a 3D fracture modeling program that is under development by Advantek International. @FRAC is a consolidation of packages to simulate injection for waste disposal and petroleum related uses. The program is a 3D hybrid finite element-boundary integral model that treats the fracture tip with singular elements (Advantek, 2004). The software package incorporates 3D virtual reality visualization with fracture treatment and design performance. This code is currently under development and a commercially available version is not available yet.

Simfrac

Simfrac is a hydraulic fracturing program by TAURUS Reservoir Solutions Ltd. of Calgary, Alberta. The software features a conventional 3D hydraulic fracture simulation, is fully documented and runs under Windows, but does not have a graphical user interface (Settari, 2004).

HYFRACP3D

Hyfracp3d is a psudo-3D finite element hydraulic fracture geometry simulator that utilizes 2D planar solution. The model predicts the fracture geometry over time for a fracture propagating in a three-layered system of variable lithology (Advani et al., 1985). The model employs a finite element solution to numerically solve the non-linear partial equations for fracture fluid pressure and induced fracture dimensions. The software lacks proppant transport capabilities, is limited to a three layer system, only allows for psudo-3D simulations, and does not have a graphics package.

Model Selection

Warpinski et al., (1994) conducted a study of hydraulic fracture models to provide a practical comparison of available models. The results show that there was significant variability in predicted fracture geometries simulated with the same input parameters (Warpinski et al., 1994). Different options available as part of a software package can significantly alter results, however, consistent results can be obtained from a given model when run by different organizations (Warpinski et al., 1994). Based on the software review, Stimplan, MFrac, and Terrafrac would be the top three choices of software based on the 3D modeling capabilities, design functions, treatment of fracture geometry and materials database. Also, of the simulators tested by Warpinski et al., (1994) Stimplan, Terrafrac and MFrac seemed to be in general agreement of fracture geometry. For this study, StimPlan by NSI Technologies was selected on the basis of available features and cost.

Units

The majority of work on hydraulic fracturing and fracture modeling has been in the petroleum industry. Therefore, traditional oil field units were used in the study in order to relate to available literature (Table 2.1).

Table 2.1 Unit conversions for traditional oilfield units (Economides and Boney, 2000)

Variable	Oilfield Units	Conversion (multiply oilfield units)	SI Units
Length	ft	3.05×10^{-1}	m
Width	in	2.54	cm
Area	ft^2	9.29×10^{-2}	m^2
Permeability	md	9.9×10^{-16}	m^2
Pressure	psi	6.9×10^{3}	Pa
Viscosity	cp	1×10^{-3}	Pa-s
Pumping Rate	BPM	2.65×10^{-3}	m^3/s
Proppant Concentration	PPG	1.20×10^{-1}	kg/L

Physical Properties of Rock

The physical properties of the rock need to be known in order to predict the characteristics of hydraulically induced fractures. The important physical properties that are needed to input into the models are Young's modulus (E), Poisson's ratio (v), and the fracture toughness (K_{IC}). Published data were collected for the rock types of interest, and the reported range of physical characteristics was used to represent the physical properties in the model.

The plane strain modulus (E') referred to as *modulus*, is defined as:

$$E' = \frac{E}{(1-v^2)} \tag{2.1}$$

where E is Young's modulus and v is Poisson's ratio (Mack and Warpinski, 2000). A range of modulus values was calculated from reported values of E and v to represent a limestone formation as well as adjacent shale and sandstone layers.

Limestone Properties – Range of Published Data

Published data from laboratory tests were compiled to find the range of values for E, v, and K_{IC} in order to calculate the modulus and estimate the mechanical properties of the limestone formation. Data from 56 reported values of E, ν and 47 reports of K_{IC} were compiled from 7 sources (Robertson, 1959; Somerton et al. 1969; Schmidt, 1976; Atkinson and Meredith, 1987; Hatheway and Kiersch, 1989; Meredith, 1989; Ochterlony, 1989). Young's Modulus for limestone ranged from 0.31 to 14.1 Mpsi with an average of 6.27 Mpsi (Table 2.2, Figure 2.3). The reported values of Poisson's ratio

for limestone contained some data (Figure 2.4) that fall beyond the normal range of 0.0 to 0.5 (Goodman, 1980). These points were considered outliers and were removed for the calculation of summary statistics (Table 2.2). The modulus was calculated from reports of E and ν from the same material. Values for the modulus range from 0.2 to 15.4 Mpsi with an average of 6.6 Mpsi (Table 2.2). The distribution of the limestone elastic modulus indicates that 40% of the values lie between 4.6 to 8.9 Mpsi and that 21% are less than 2.5 Mpsi (Figure 2.5). The fracture toughness of limestone ranges from 325 to 1810 psi√in with an average of 1003 psi√in (Table 2.2, Figure 2.6).

Table 2.2 Range of physical properties expected for limestone

	Young's Modulus (*E*) (Mpsi)	Poisson's Ratio (*v*)	Modulus (*E'*) (Mpsi)	Fracture Toughness (psi√in)
Minimum	0.31	0.01	0.3	325
Maximum	14.1	0.32	15.4	1810
Average	6.3	0.18	6.6	1003
Std. Dev	3.5	0.1	3.7	293

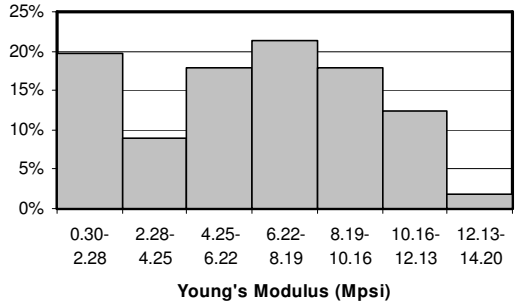

Figure 2.3 Distribution of Young's Modulus for limestone

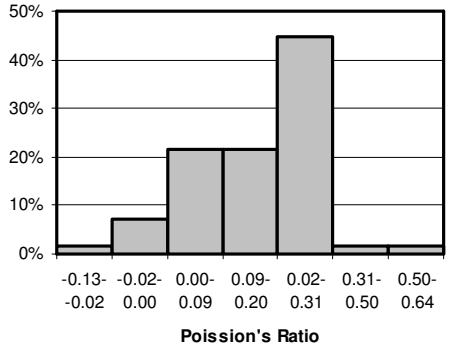

Figure 2.4 Distribution of Poisson's Ratio for limestone

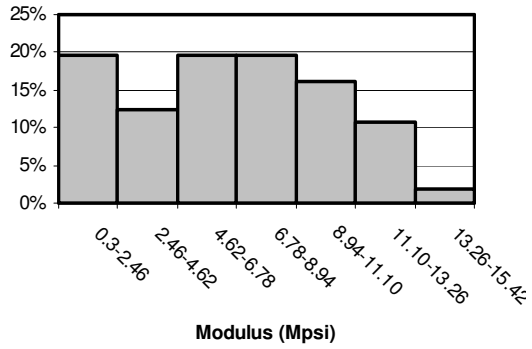

Figure 2.5 Distribution of limestone modulus

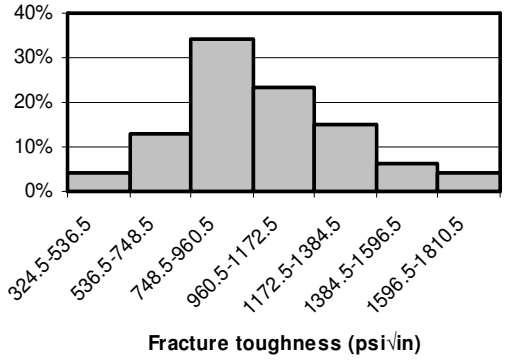

Figure 2.6 Distribution of limestone fracture toughness

Shale Properties

Published data was analyzed to find the range of values for E, v, and K_{IC} in order to estimate the mechanical properties of a shale formation. Data from 23 laboratory measurements of E and v and 32 measurements of K_{IC} were collected from 4 sources (Atkinson and Meredith, 1987; Hatheway and Kiersch, 1989; Ochterlony, 1989; Chen and Zhang, 2004). Young's modulus of shale ranged from 0.06 to 9.9 Mpsi with an average of 2.5 Mpsi (Figure 2.7, Table 2.3). The reported values of Poisson's ratio for shale contained some data (Figure 2.8) that fall beyond the normal range of 0.0 to 0.5 (Goodman, 1980). These points were considered outliers and were removed for the calculation of summary statistics (Table 2.3). Individual values of the modulus were calculated from E and v measurements from the same material. Values for the shale modulus range from 0.06 to 10.0 Mpsi with an average of 2.5 Mpsi (Table 2.3). The distribution of the shale elastic modulus is skewed to the left with 65% of the reported values less than 2.05 Mpsi (Figure 2.9). The shale fracture toughness ranges from 220 to 1177 psi√in with an average of 721 psi√in (Table 2.3, Figure 2.10).

Table 2.3 Range of physical properties expected for shale

	Young's Modulus (E) (psi)	Poisson's Ratio (v)	Modulus (E') (Mpsi)	Fracture Toughness (psi√in)
Minimum	0.06	0.01	0.1	220
Maximum	9.9	0.37	10	1177
Average	2.5	0.16	2.5	721
Std. Dev	3.1	0.12	3.1	260

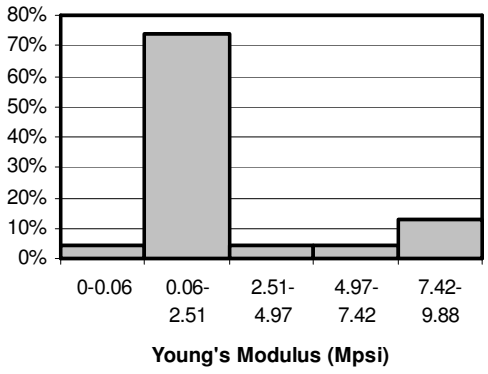

Figure 2.7 Distribution of Young's Modulus for shale

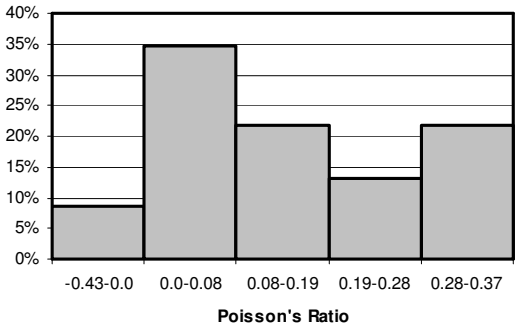

Figure 2.8 Distribution of Poisson's Ratio for shale

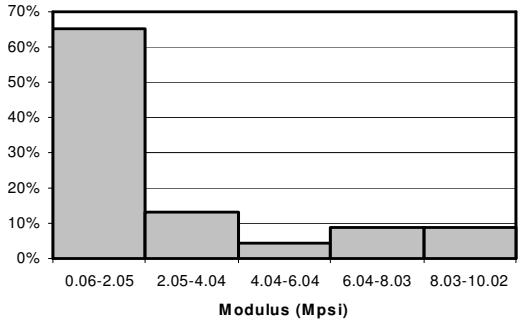

Figure 2.9 Distribution of shale modulus

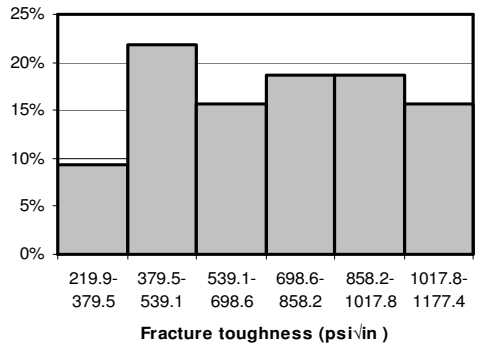

Figure 2.10 Distribution of shale fracture toughness

Sandstone Properties

Published data were analyzed to find the range of values for E, v, and K_{IC} in order to estimate the mechanical properties of a sandstone formation. Data from 25 laboratory measurements of E and v and 45 measurements of K_{IC} were collected from 8 sources (Baidyuk, 1967; Somerton et al. 1969; Atkinson and Meredith, 1987; Hatheway and Kiersch, 1989; Matsuki, 1989; Meredith, 1989; Ochterlony, 1989; Chen and Zhang, 2004). Young's modulus for sandstone ranged from 0.06 to 8.0 Mpsi with an average of 2.1 Mpsi (Figure 2.11). Poisson's ratio for sandstone ranges from 0.06 to 0.36 with an average of 0.16 (Figure 2.12, Table 2.4). Individual values of the modulus were calculated from E and v measurements from the same material. Values for the modulus of sandstone ranged from 0.06 to 8.2 Mpsi with an average of 2.2 Mpsi (Table 2.4). The distribution of the sandstone elastic modulus is skewed to the left with 39% of the reported values in the range of 1.2 to 2.4 Mpsi (Figure 2.13). The sandstone K_{IC} ranges from 193 to 2345 psi√in with an average of 1021 psi√in (Table 2.4, Figure 2.14).

Table 2.4 Range of physical properties expected for sandstone

	Young's Modulus (E) (psi)	Poisson's Ratio (v)	Modulus (E') (Mpsi)	Fracture Toughness (psi√in)
Minimum	0.1	0.01	0.06	193
Maximum	8.0	0.36	8.2	2345
Average	2.1	0.16	2.1	1021
Std. Dev	2.0	0.10	1.9	662

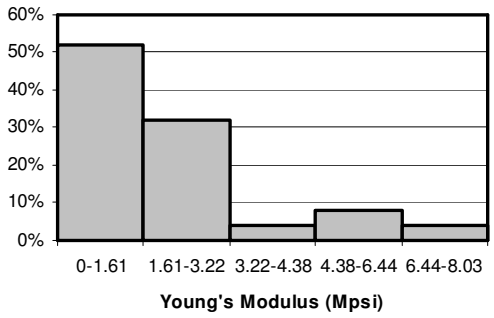

Figure 2.11 Distribution of Young's Modulus for sandstone

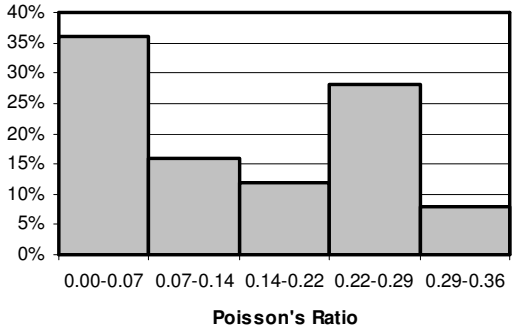

Figure 2.12 Distribution of Poisson's Ratio for sandstone

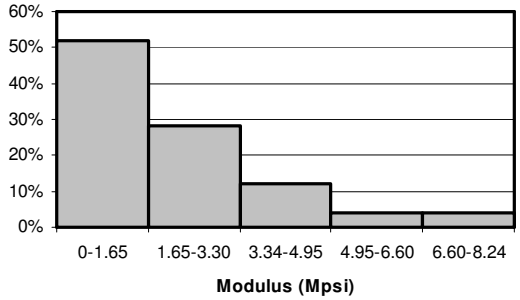

Figure 2.13 Distribution of sandstone modulus

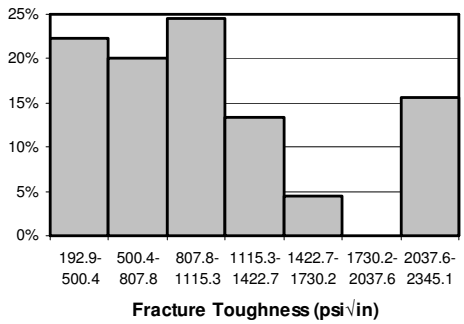

Figure 2.14 Distribution of sandstone fracture toughness

Methods of Fracture Modeling

In order to model the characteristics of a hydraulic fracture created in limestone, a commercially available code, StimPlan by NSI Technologies was selected to run the simulations. The model has more than 25 input variables that include formation bedding, formation type, mechanical properties of the rock, in-situ stress, fracturing fluid, proppant, pumping rate, leakoff coefficient and pumping schedule. The values for the model inputs were selected based on the ranges of reported data. A representative baseline scenario was designed to characterize an ideal situation and variations of high, middle and low values for key variables were tested to determine the sensitivity of parameters.

Conceptual Model

The conceptual model of the system in which hydraulic fractures were simulated is a three layer system consisting of a target limestone formation that has an overlying and underlying formation of shale (Figure 2.15). It is assumed that all of the formations are homogeneous and isotropic with horizontal bedding. The thickness of the adjacent formations for the majority of simulations is 500 ft. The fracture is initiated by pumping fluid through a vertical well bore that is open to the formations only at the perforated interval. A baseline case was set up as a fracture with an idealized half length of 300 ft in a 300 ft thick limestone formation. The thickness was selected to represent a realistic thickness for a limestone that would be suitable for the formation of caverns for gas storage by acid dissolution (Castle et al., 2004b). The fracture length was selected to represent a fracture with a half length equal to the height of the formation. Variations in the model inputs were tested to discover the range of possible fracture characteristics as well as to demonstrate the effects of the different variables on fracture geometry and flow.

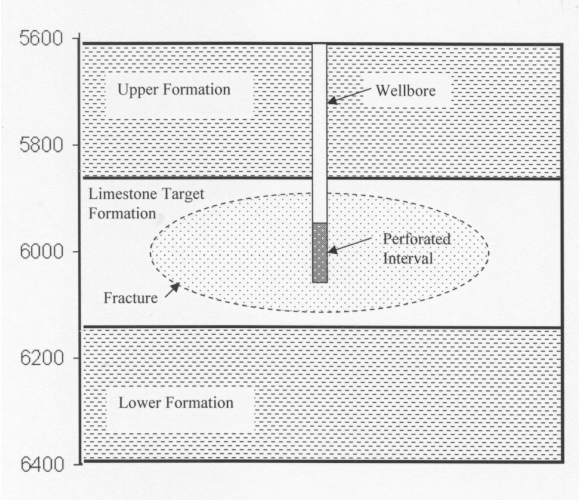

Figure 2.15 Conceptual model of radial fracture in a 300 ft limestone formation bounded by 500 ft thick shale formations.

Model Inputs

The fracture simulation portion of StimPlan by NSI technologies Inc. has more than 25 input variables, including detailed stratigraphy and mechanical properties. For the sensitivity analysis of fracturing a limestone formation the data input for the model was divided into three classes; inputs that were assumed to be constant, inputs that varied at a constant rate with depth and inputs that were systematically varied for the tests. The inputs that were held constant for all of the runs are: porosity, permeability, fluid temperature, minimum Bottom Hole Flowing Pressure (BHFP), drainage area, design concentration and pump schedule. The model inputs that varied at a constant rate with depth were: closure pressure, reservoir pressure, formation temperature, and the in-situ stress. The input variables that were systematically varied were: limestone thickness, stress difference between limestone and adjacent layers, perforated interval length, limestone modulus, limestone fracture toughness, type of adjacent layer, adjacent layer modulus, adjacent layer fracture toughness, pumping rate, depth, fluid type, and proppant type.

Constant Inputs

The porosity of the limestone was assumed to be 0.1 and the permeability 0.1 md (Table 2.5). These values were selected to characterize the properties expected for the limestone target formation as well as represent the properties observed in limestone at the target depth (Robertson 1959). The assumed values of porosity are conservatively high, but were held standard for continuity of the model. Variations in porosity and permeability are accounted for by variations of the leakoff coefficient. The temperature of the fracturing fluid was set at a constant 70˚ F, a reasonable ambient temperature at the surface (Table 2.5). BHPF is the fluid pressure in the well, usually measured at the top of the target formation. The BHFP and drainage area are parameters that are specifically used in the model for simulations of petroleum reservoir productivity and have little effect on fracture geometry simulations. To maintain continuity of the simulations, the BHFP was set to 500 psi and the drainage area was set to 400 acres, the defaults of the model (Table 2.5).

Table 2.5 Constant input parameters and gradients used for simulations

Porosity	0.1
Permeability	0.1 md
Fluid Temperature	70 °F
BHFP	500 psi
Dranage area	400 acres
Proppant Concentration	11 PPG
Pumping Schedule	Table 2.6
Formation Temperature	48 °F/mile
In-Situ Stress	0.7 psi/ft
Reservoir Pressure	0.45 psi/ft

Design Concentration/Pumping Schedule

The design concentration for the mass of the proppant in the slurry for all of the simulations was 11 PPG (Table 2.5). That is, there are 11 pounds of proppant for every gallon of fluid. The typical range for design concentration is 6 to 14 PPG, and 11 PPG is on the high side of the mid-point of this range. The pumping schedule used for the baseline fracture simulations was derived from the design function that is part of the StimPlan software. It was created by using the baseline data to calculate a pump schedule for a fracture with an intended 300 ft half length (Table 2.6). This pump schedule was used for all of the simulations that were variations of the baseline case. A different pumping schedule was designed for simulations of a fracture with a 30 ft idealized length (Table 2.7). There was also a pumping schedule generated for a fracture with a proposed length of 1500 ft (Table 2.8).

Table 2.6 Pumping schedule for 300 ft horizontal half-length fracture

Stage	Slurry Volume (Mgal)	Fluid Volume (Mgal)	Concentration (PPG)	Rate (BPM)	Cumulative Proppant (MLbs)	Pump Time (min)
1	6.08	6.08	0	30	0	4.8
2	0.1	0.09	2	30	0.2	0.1
3	0.29	0.25	3	30	1	0.2
4	1	0.84	4	30	4.3	0.8
5	2.77	2.18	6	30	17.4	2.2
6	4.74	3.47	8	30	45.2	3.8
7	4.93	3.39	10	30	79.1	3.9
8	1.87	1.25	11	30	92.9	1.5
Total Slurry		21.8 Mgal		Total Pump Time		17.3 min
Total Proppant		92.9 MLbs		Avg. Conc.		5.3 PPG
Total Fluid		17.6 Mgal		Pad %		27.90%

Table 2.7 Pumping schedule for 30 ft horizontal half-length

Stage	Slurry Volume (Mgal)	Fluid Volume (Mgal)	Concentration (PPG)	Rate (BPM)	Cumulative Proppant (MLbs)	Pump Time (min)
1	0.22	0.22	0	30	0	0.2
2	0.11	0.08	8	30	0.7	0.1
3	0.28	0.19	10	30	2.6	0.2
4	0.16	0.11	11	30	3.7	0.1
Total Slurry		21.8 Mgal		Total Pump Time		17.3 min
Total Proppant		92.9 MLbs		Avg. Conc.		5.3 PPG
Total Fluid		17.6 Mgal		Pad %		27.90%

Table 2.8 Pumping schedule for a 1500 ft horizontal half-length fracture

Stage	Slurry Volume (Mgal)	Fluid Volume (Mgal)	Concentration (PPG)	Rate (BPM)	Cumulative Proppant (MLbs)	Pump Time (min)
1	75.1	75.1	0	30	0	59.6
2	0.77	0.74	1	30	0.7	0.6
3	2.45	2.24	2	30	5.2	1.9
4	4.61	4.06	3	30	17.4	3.7
5	11.32	9.58	4	30	55.7	9
6	23.05	18.12	6	30	164.5	18.3
7	30.95	22.72	8	30	346.2	24.6
8	27.54	18.95	10	30	535.7	21.9
9	9.72	6.49	11	30	607.1	7.7
Total Slurry		185.5 Mgal		Total Pump Time		158.0 min
Total Proppant		607.1 MLbs		Avg. Conc.		3.8 PPG
Total Fluid		142.2 Mgal		Pad %		40.50%

Constant Rate Variables

Reservoir pressure, closure pressure, formation temperature and in-situ stress are all model inputs that were used in the models as variables that changed at a constant rate with depth. The gradient used for reservoir fluid pressure is 0.43 psi/ft, a characteristic value for the reservoir pressure gradient (Smith and Shalyapobersky, 2000). The closure pressure (σ_{cl}) was calculated as a function of the pressure that results from the weight of the overburden (σ_v), the reservoir pressure (P_{res}) and a poro-elastic formation constant (K_o).

$$\sigma_{cl} \approx K_o * (\sigma_v - P_{res}) + P_{res} \qquad (2.2)$$

The pressure that is generated by the weight of the overburden was calculated from the gradient of 1.0 psi/ft (Nolte, 2000, Thiercelin and Roegiers, 2000) and K_o equals 0.33 (Smith and Shlyapobersky, 2000). The formation temperature was calculated from the average geothermal gradient for the Eastern states of 48˚F/mile (25˚C/km) (Nathenson and Guffaint, 1988). The typical in-situ stress gradient is 0.7 psi/ft (Smith and Shalyapobersky, 2000).

Variables Tested

The model inputs that were systematically varied to represent the range of expected values can be divided into to categories: in-situ parameters and parameters that can be adjusted at the surface. The in-situ parameters tested were depth, limestone thickness, stress difference, mechanical properties of the rock formations and the leakoff coefficient (Table 2.9). The parameters that can be adjusted from the surface are the pumping rate, perforated interval, fracturing fluid type, and proppant type (Table 2.10). The depth selected for the baseline simulation is 6000 ft. A shallower fracture at 4000 ft

Table 2.9 In-situ parameters tested

	Low	Baseline	High
Depth	4000 ft	6000 ft	8000 ft
Limestone Thickness	30 ft	300 ft	1500 ft
Stress Difference	-900 psi	-300 psi	900 psi
Limestone Modulus	0.5 Mpsi	6.5 Mpsi	15 Mpsi
Limestone Fracture Toughness	350 psi$\sqrt{in}$	1000 psi$\sqrt{in}$	1800 psi$\sqrt{in}$
Adjacent Layer Modulus	0.1 Mpsi	2.5 Mpsi	4.3 Mpsi
Adjacent Layer Fracture Toughness	246 psi$\sqrt{in}$	730 psi$\sqrt{in}$	1292 psi$\sqrt{in}$
Leakoff Coefficient	1.0×10^{-5} ft$\sqrt{min}$	1.0×10^{-4} ft$\sqrt{min}$	1.0×10^{-2} ft$\sqrt{min}$

Table 2.10 Range of adjustable parameters tested

	Low	Baseline	High
Pumping Rate	6 BPM	30 BPM	150 BPM
Perforated Interval	20 ft	150 ft	300 ft
Fracturing Fluid Viscosity	45 cp	320 cp	840 cp
Proppant Size/Strength	12-20 Sand	20-40 Sand	20-40 Bauxite

and a deeper fracture at 8000 ft were also simulated to test fracture characteristics within the optimal range for natural gas storage (Castle et. al., 2004b). A limestone thickness of 300 ft was selected as the baseline value. A thicker limestone of 1500 ft and a thinner limestone of 30 ft were also tested (Table 2.9).

Limestone Properties-Values Used in Model

The elastic modulus selected for the baseline case is 6.60 Mpsi to represent the average value of modulus based on the data collected (Table 2.2). A high modulus value of 15 Mpsi and a low modulus value of 0.5 psi were tested (Table 2.9). These values were

chosen to represent the range of values possible as well as provide a broad-spectrum representation of the modulus. The value for fracture toughness used in the baseline simulation was 1000 psi√in. The variation in fracture toughness used to represent the reported range of values was 1800 psi√in for the high end of the range and 350 psi√in for the low end of the range (Table 2.9). The values selected to represent the limestone modulus and fracture toughness represent the range of values from reported data (Table 2.2).

Adjacent Layers

The adjacent layers for the baseline simulation were designed to represent a 500-ft-thick shale unit with a modulus of 2.50 Mpsi, a fracture toughness of 730 psi√in and an in-situ stress that was 300 psi greater than the stress in the limestone unit. These values were selected because they are typical for shale. The values of modulus and fracture toughness for shale are also within the range of the values for sandstone, and therefore could represent sandstone as well. A high, middle and low value of the modulus and fracture toughness were selected to test the affects on fracture characteristics (Table 2.11). Each of the selected values of modulus was simulated with each of the values for fracture toughness so that nine simulations were run to demonstrate the effects of modulus with different values for toughness within the expected range for shale and limestone. The nine tests were run twice, once with the stress in the limestone 300 psi less than the in-situ stress in the shale, and once with no stress difference between the units.

Table 2.11 Modulus and Fracture Toughness values used for adjacent layer

Modulus (Mpsi)	Fracture Toughness (psi√in)
0.1	246
4.3	1292
8.5	2337

Stress Difference

For the baseline scenario, the adjacent shale layers had a stress difference of 300 psi greater than the limestone formation. Four other values of the stress difference were also simulated. The values input for the limestone formation were: -900 psi, -300 psi, 0 psi, 300 psi, and 900 psi. Negative values indicate situations where the stress in the adjacent formations was greater than the limestone formation and positive values indicate situations where the stress in the limestone was greater than in the adjacent formations.

Leakoff Coefficient

The leakoff coefficient input into StimPlan is the total leakoff coefficient and is related to resistance to fluid loss due to the fracturing fluid filtrate viscosity, a resistance to fluid loss from the reservoir fluid, and to the fracturing fluid system itself forming a filter cake which retards fluid loss (NSI, 2004b). The range of the fluid loss coefficient was 1.0×10^{-5} ft√min to 1.0×10^{-1} ft√min. The entire range was tested in steps of half order of magnitude. The values of leakoff coefficient simulated were: 1.0×10^{-5} ft√min;

5.5 x 10^{-5} ft√min; 1.0 x 10^{-4} ft√min; 5.5 x 10^{-4} ft√min; 1.0 x 10^{-3} ft√min; 5.5 x 10^{-3} ft√min; 1.0 x 10^{-2} ft√min; 5.5 x 10^{-2} ft√min; and 1.0 x 10^{-1} ft√min.

Perforated Interval

It was assumed that fracture initiation occurred at the same length of perforated interval for all of the simulations. Also, the midpoint of the perforated interval was located at the midpoint of the limestone formation height. The baseline perforated interval was set at 150 ft, one half of the limestone thickness. A longer perforated interval of 300 ft, perforated throughout the limestone formation, and a shorter perforated interval of 30 ft were also simulated (Table 2.10).

Pumping Rate

The pumping rate for the baseline model was set at 30 barrels per minute (BPM) based on the average injection rates from 53 published fracture treatments (Ranostaj, 1976; Horton, 1981, Miller and Smith, 1989; Smith and Shalyapobersky, 2000). A pumping rate of approximately 30 BPM is also predicted to be the most cost effective (Lacy and Smith, 1989). The pumping rate can range from 0.5 BPM to several hundred BPM. To test the effects of variations in pumping rate on fracture formation, a low pumping rate of 6 BPM and a high rate of 150 BPM were simulated (Table 2.10).

Fluid Properties

The fracturing fluid chosen for the baseline runs was 30# X-Link. This is one of eight fluids included in the model database and is the fluid with the median viscosity. 30# X-Link is a fracturing fluid that has 30 pounds of a polymer per 1000 gallons of water with a crosslinker added. A total of five different fluid types were used to evaluate the effect of fracturing fluid rheology on fracture characteristics (Table 2.12). 60Q/40#fm is 60 Quality foam using 40 pounds of gel per 1000 gallons of water as the liquid phase of the foam, and 60 Quality means that the foam is 60% Nitrogen or Carbon Dioxide by volume. The data pertaining to fluid type in the model falls into two main inputs, fluid type and fluid temperature. The injection temperature for the fluid was assumed to be at an average ambient air temperature of 70°F. Variations of fluid temperature should have a negligible effect on the fracture characteristics, so the fluid temperature was held constant.

Table 2.12 Different fracturing fluids tested and their viscosities at formation temperature

Fracturing Fluid	Viscosity (cp) @ Formation Temp
60Q/40#fm	45
70Q/40#fm	52
30#_X-Link	320
40#_X-Link	640
50#_X-Link	840

Proppant

The proppant used in the baseline simulation is 20/40 sand with a design concentration of 11 ppg. The 20/40 sand was chosen because the particle size is small enough to enter into fractures with a width of 0.066 in and can be transported to deeper formations than larger sized proppants (Anderson et al., 1989). A range of proppant sizes and types were tested to evaluate how differences in proppant size and strength affect the fracture characteristics (Table 2.5).

Table 2.5 Characteristics of proppants used in simulations.

Proppant	Mesh range (in)	Specific Gravity	Damage Factor
12-20 Sand	0.066-0.033	2.65	0.70
16-30 Sand	0.047-0.023	2.65	0.70
16-30 RCSandPC	0.047-0.024	2.55	0.80
20-40 Sand	0.033-0.017	2.65	0.70
20-40 Int_Strength	0.033-0.017	3.15	0.80

Adjacent Formation Thickness

The thickness of the adjacent layers was 500 ft for the majority of the simulations. The data for these simulations was used to calculate the distribution of fracture characteristics. The thickness of the adjacent layer was varied to test the effect of the adjacent formation thickness on vertical fracture growth. The adjacent layer thickness tested were 1 ft, 10 ft, 25 ft, 50 ft, 75 ft, 100 ft, 150 ft and 200 ft. The material on the above and below the shale layers is assumed to be limestone.

Results of Fracture Modeling

Baseline Fracture

The fracture predicted by the baseline case is an elliptical shaped feature with a half-length of 291 ft and a height of 363 ft at the borehole that penetrated 115 ft into the upper shale layer and 98 ft into the lower shale layer. The pressurized fracture width is 0.33 in near the well bore and it tapers to the fracture termination at 291 ft (Figure 2.16).

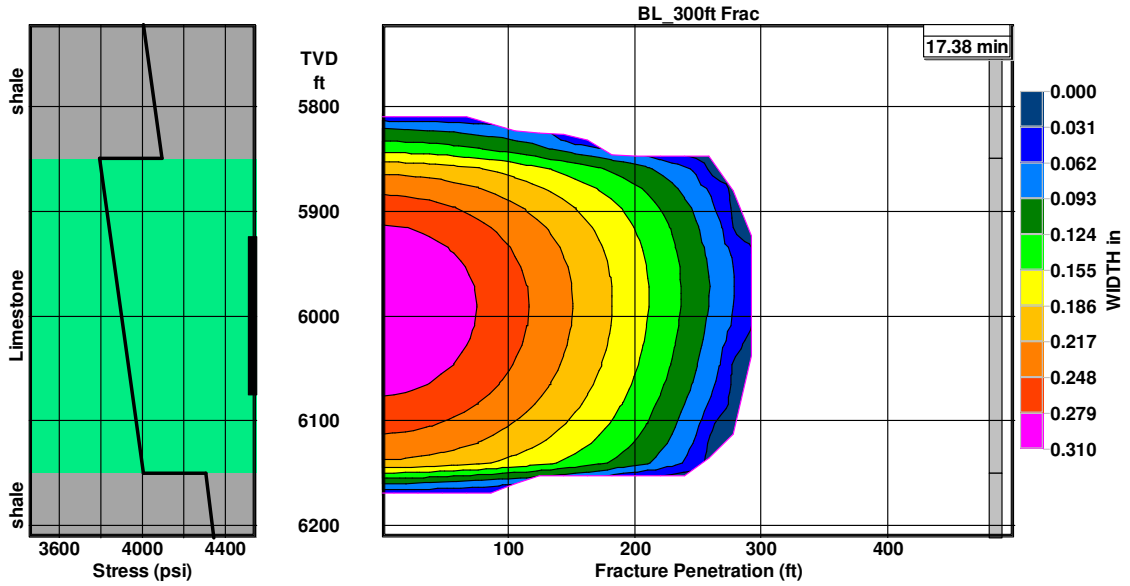

Figure 2.16 Pressurized width (in) for baseline fracture model with stress profile. The thick black line on right side of stress plot indicates perforated interval.

The in-situ stress is 4095 psi at the bottom of the shale and it abruptly drops to 3795 psi at the top of the limestone. The stress increases with depth according to the stress gradient of 0.7 psi/ft until the stress at the bottom of the limestone layer is 4005 psi. The stress is 4305 psi at the top of the underlying shale. The perforated interval for the baseline case is 150 ft, initiating from the middle of the limestone layer (Figure 2.16). The net pressure calculated for this fracture geometry is 358 psi above closure pressure.

The cross section of the baseline fracture at the bore hole is roughly oval shaped with the long axis vertical (Figure 2.17). The oval pinches and become more pointed near the top and bottom, at depths of 5850 ft and 6150 ft. These are the depths of the contacts between limestone and shale. The maximum pressurized width is 0.32 in at a depth of 6000 ft (Figure 2.17).

The fracture half-length that remains propped at closure is 200 ft, approximately 70% of the total fracture half-length. The effective width of the propped fracture is 0.148 inches in the vicinity of the perforated interval (Figure 2.18). The large dark blue area on Figure 2.18 indicates the region that was fractured during injection, but was not filled

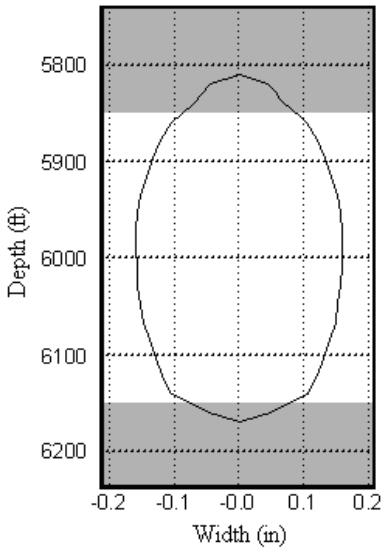

Figure 2.17 Cross section of baseline fracture. Grey boxes indicate adjacent layers

with proppant. At fracture closure, this area is held open only by asperities on the fracture wall.

The average conductivity for the baseline fracture is 396 md-ft, but the distribution of conductivity is variable throughout the fracture (Figure 2.19). *Conductivity* as used in this paper refers to the product of fracture permeability and fracture width (Economides et al., 2004). There is a region around the initiation area where the conductivity is greatest (1224 md-ft), but it decreases away from the fracture and is less than 122 md-ft in the region in dark blue (Figure 2.19). The contours of conductivity are nearly identical to the contours for effective width because fracture width is used in the calculation of conductivity. The dark green line (Figure 2.19) represents the contour that has the average value for conductivity developed over the entire fracture area. This contour approaches 150 ft from the well bore. This indicates that the region near the well bore, representing almost 1/2 of the facture, has a higher conductivity than the more distal parts.

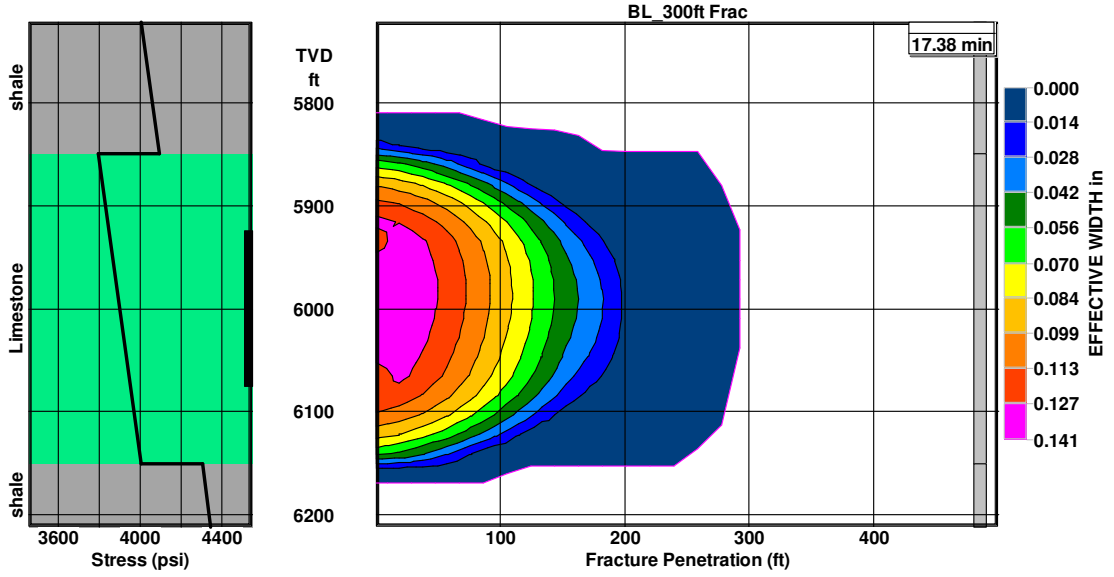

Figure 2.18 Effective width (in) for the baseline fracture with stress profile. The thick black line on right side of stress plot indicates perforated interval.

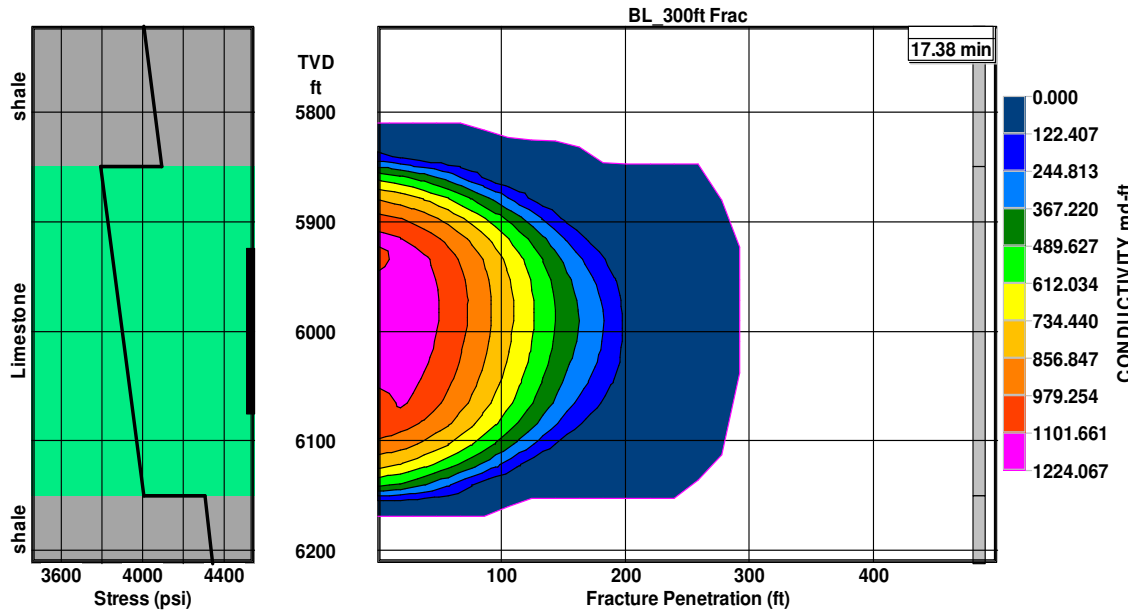

Figure 2.19 Conductivity for baseline fracture model with stress profile. The thick black line on right side of stress plot indicates perforated interval.

Net Pressure

The net pressure is the pressure greater than the closure pressure that is necessary to cause the fracture to propagate, assuming that a crack already exists in the rock. When plotted with time, the net pressure is a function of fracture geometry. For radial geometry, the net pressure declines versus time, thus the highest net pressure would be initially. If the geometry is a confined height fracture that is growing in length, then net pressure tends to increase with time, and the highest P-Net would be at the end of pumping (Smith, 2004a).

The net pressure for the baseline simulation is initially 613 psi and decreases rapidly to the lowest pressure of 308 psi at a time of 5 min (Figure 2.20). As pumping continues, the net pressure increases to 372 psi at 17 min and the fracture closes at the end of the pumping schedule (Figure 2.20). The initial decrease in pressure indicates that the fracture propagates with radial geometry until a time of 5 min when it begins to interact with the adjacent layers, confining the fracture height.

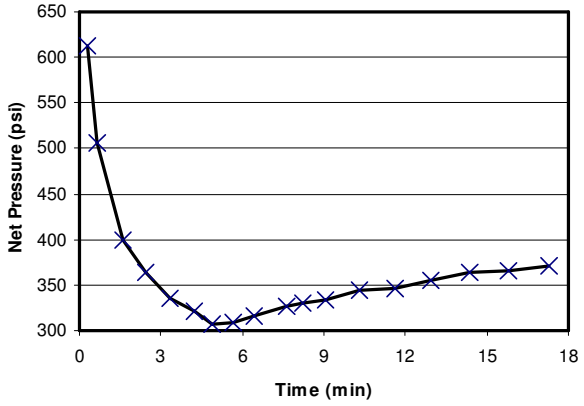

Figure 2.20 Net pressure vs. time for baseline simulation

Deviations from Baseline Model

The baseline fracture was assumed to represent a standard to which the results of systematic variations in the input parameters would be compared. Thirteen of the model input values were systematically varied in order to understand the range of possible fracture geometries as well as to understand the effects of the different variables on fracture geometry. The variables modified are: leakoff coefficient, formation depth, stress contrast between formations, elastic modulus and fracture toughness of adjacent formation, elastic modulus and fracture toughness of limestone, limestone thickness, perforated interval, pumping rate, fracturing fluid, and proppant type (Table 2.13). The inputs for the baseline case were average values for the parameters. For each input variable one trial was conducted where the variable was five times the average and one trial was conducted where the variable was one-fifth of the average. This resulted in a high, medium and low value for each of the variables. The distribution of fracture half-length, height and conductivity of the simulations were analyzed.

Half-length Distribution

The fracture half-length for the fractures simulated (Table 2.13) were recorded and summary statistics were calculated (Table 2.14). The baseline half-length of 291 ft was 3 feet longer than the average value, within the 79 ft standard deviation and 291ft is the mode of the data set (Table 2.14). Forty-seven percent of the simulations resulted in fractures with a half-length in the range of 232 to 295 ft with the majority of fracture half-lengths (83%) ranging between 169 ft to 358 ft (Figure 2.21). Four percent of the results have a half-length less than 106 ft (Figure 2.36). For these two cases, the leakoff coefficient was relatively high (1.0×10^{-3} ft$\sqrt{}$min and 5.5×10^{-3} ft$\sqrt{}$min) and tip screenout occurred. Four of the trials (9%) resulted in a fracture with a half-length greater than 421 ft (Figure 2.21). For two of the cases, greater lengths occurred when fracturing fluids with a lower viscosity were used (70Q/40#fm and 60Q/40#fm), one case occurred when leakoff coefficient was 1.0×10^{-4} ft$\sqrt{}$min and one case was the result of reducing the pumping rate to 6 BPM.

Table 2.14 Statistics of fracture half-length distribution

Minimum	43	ft
Maximum	481	ft
Median	293	ft
Mode	291	ft
Average	288	ft
Std. Dev.	79	ft
Count	47	

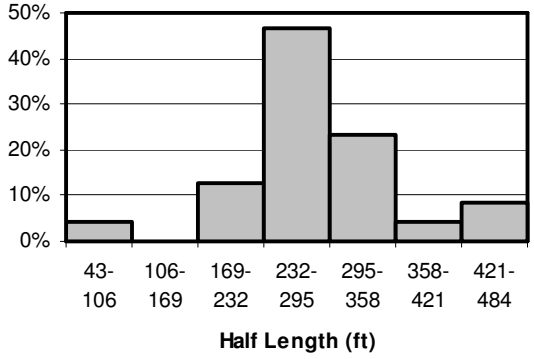

Figure 2.21 Distribution of horizontal half-length

Table 2.13 Variables tested for distribution analysis

		Low	Baseline	High			
Limestone Thickness (ft)		30 ft.	300 ft.	1500 ft.			
Pumping Rate (BPM)		6 BPM	30 BPM	300 BPM			
Perforated Interval (ft)	20 ft.	30 ft.	300 ft.	1500 ft.			
Depth (ft)		4000 ft.	6000 ft.	8000 ft.			
Stress Difference (psi)		-900 psi	-300 psi	0 psi	300 psi	900 psi	
Limestone Modulus (Mpsi)		0.5 Mpsi	6.5 Mpsi	15 Mpsi			
Limestone Fracture Toughness (psi$\sqrt{in}$)		350 psi$\sqrt{in}$	1000 psi$\sqrt{in}$	1800 psi$\sqrt{in}$			
Boundary Layer Modulus (Mpsi)		0.1 Mpsi	2.5 Mpsi	4.3 Mpsi	8.5 Mpsi		
Boundary Layer Fracture Toughness (psi$\sqrt{in}$)		246 psi$\sqrt{in}$	730 psi$\sqrt{in}$	1292 psi$\sqrt{in}$	2337 psi$\sqrt{in}$		
Fracturing Fluid	60Q/40#fm	70Q/40#fm	30#_X-Link	40#_X-Link	50#_X-Link		
Proppant 12-20 Sand	16-30 Sand	16-30 RCSandPC	20-40 Sand	20-40 Int_Strength	20-40 Bauxite		
Leakoff Coefficient (ft$\sqrt{min}$)	1.0×10^{-5}	5.5×10^{-5}	1.0×10^{-4}	5.5×10^{-4}	1.0×10^{-3}	5.5×10^{-3}	1.0×10^{-2}

Propped Length Distribution

The propped length of the fracture was determined to be the furthest contour from the borehole where both the conductivity and the proppant concentration were greater than zero. The propped length for the baseline fracture is 200 ft, which corresponds with the mean, median and mode of all the trials (Table 2.15). More than half the results for propped length range from 166 ft to 212 ft and 83% ranges from 120 ft to 258 ft (Figure 2.22). Four percent of the trials resulted in fractures with half lengths less than 74 ft. The shortest propped lengths occurred during simulations using relatively large leakoff coefficients (1.0 x 10^{-3} ft√min and 5.5 x 10^{-3} ft√min) which resulted in tip screen out. These are the same two models that resulted in the shortest fracture half-lengths. The four situations that resulted in the greatest half-lengths are the same trials that had the four longest propped lengths. The fractures with a propped length greater than 304 ft result from a case where the leakoff coefficient was 1.0 x 10^{-4} ft√min and where the pumping rate was reduced (6 BPM). The four trials that had a predicted propped length of 258 to 304 ft occurred when fracturing fluids with a lower viscosity were used (70Q/40#fm and 60Q/40#fm), when the leakoff coefficient was decreased to 5.5 x 10^{-5} ft√min and one case occurred when a 300 ft half- length was simulated in a 60 ft thick limestone formation.

There appears to be a relationship between half-length and the propped length (Figure 2.23). The propped length averages 70% +/- 5% of the half-length. For the five simulations where the ratio of the propped length to half-

Table 2.15 Statistics of propped length distribution.

Minimum	28	ft
Maximum	348	ft
Median	200	ft
Mode	200	ft
Average	201	ft
Stdev	54	ft
Count	47	

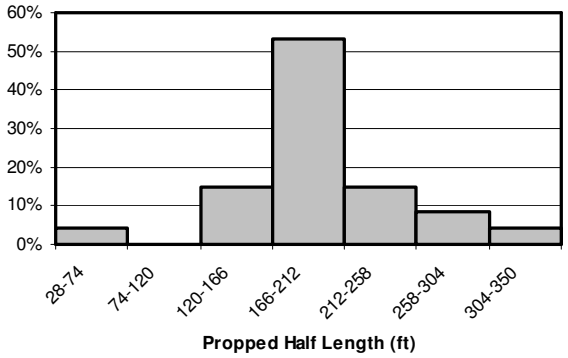

Figure 2.22 Distribution of propped fracture length

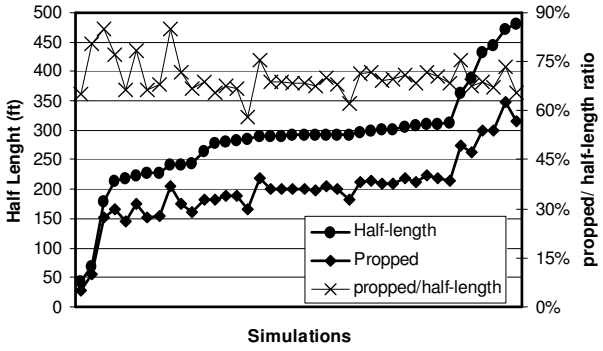

Figure 2.23 Half-length and propped length for models that vary from the 300 ft baseline case

length was greater than 75%, three of the cases occurred when the leakoff coefficient was increased to the range of 5.5×10^{-4} ft$\sqrt{}$min to 5.5×10^{-3} ft$\sqrt{}$min. The other two cases occurred when the limestone modulus was lower (0.5 Mpsi) and when the stress in the limestone was 300 psi greater than in the shale. There were two cases where the ratio of the propped length to half-length was less than 65%. For one of these cases, the stress difference between formations was increased from 300 psi less to 900 psi greater in the limestone. For the other case the perforated interval was increased from 150 ft to 300 ft, corresponding to the formation height.

Fracture Height Distribution

The fracture height is reported as the total height of the fracture with the center located at the specified target depth. The baseline case resulted in fracture with 363 ft vertical growth which corresponds to the median and mode of all the trials (Table 2.16). The average fracture height is 21 ft taller than the median and the mode. This is because a few of the trials resulted in very tall fractures that increase the average. 72% of the fracture heights occur in a range of 278 ft to 372 ft whereas only 10% of the fractures exhibited a height growth greater than 482 ft (Figure 2.24). For the four cases where height growth was greater than 485 ft,

Table 2.16 Statistics for fracture height distribution

Minimum	175	ft
Maximum	789	ft
Median	363	ft
Mode	363	ft
Average	384	ft
Stdev	120	ft
Count	47	

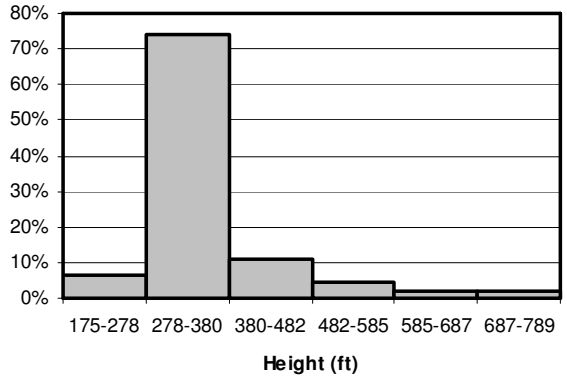

Figure 2.24 Distribution of fracture height for simulations based on baseline case

three of them were due to stress difference between the formations. These cases occurred when the stress in the adjacent layers decreased, resulting in the stress difference for the limestone increasing from -300 psi to 0 psi, 300 psi and 900 psi. The other case occurred when the limestone thickness was increased to 1500 ft.

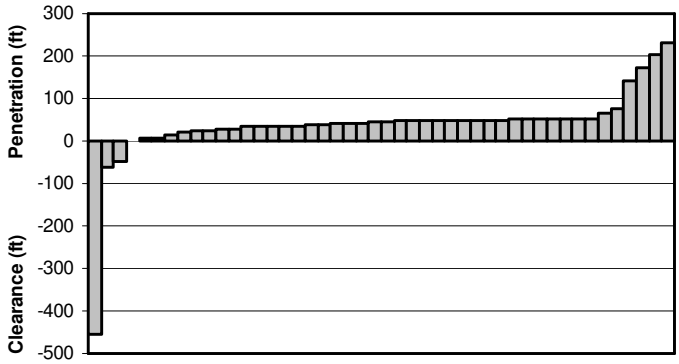

Figure 2.25 Fracture intrusion into upper adjacent layer. Negative values indicate clearance between fracture and overlying formation

One of the concerns relating to fracture height growth is intrusion into an overlying confining formation. For the fracture simulations based on the baseline case 93% had some intrusion into the upper confining layer with only 7% having some un-fractured limestone clearance between the overlying formation (Figure 2.25). Of the three cases where there was some clearance between the fracture and the overlying formation, one occurred in a simulation of a 300 ft fracture half length in a 1500 ft limestone formation. The other two cases occurred when the leakoff coefficient was increased (1.0 x 10^{-2} ft$\sqrt{}$min and 5.5 x 10^{-2} ft$\sqrt{}$min) and tip screen out occurred.

Fracture Width Distribution

The average fracture width was less than 0.32 in for 94% of simulations (Figure 2.26). Of the three cases that had widths greater than 0.32 in, two were beyond one standard deviation (+/- 0.25 in) of the mean (0.23 in). These two cases occurred when the leakoff coefficient was increased to 1.0 x 10^{-2} ft$\sqrt{}$min and 5.5 x 10^{-2} ft$\sqrt{}$min. These cases resulted in tip screenout. Although tip screenout is an effective method to increase fracture width and conductivity, these two cases were considered outliers and disregarded in order to calculate a fracture width distribution with higher resolution. The remaining fracture width calculations had a mean of 0.18 in and a median and mode of 0.19 in (Table 2.17). The average width for the baseline case is 0.19 in. Sixty-two percent of the width calculations occur within the 0.15 in to 0.19 in range when the outliers are

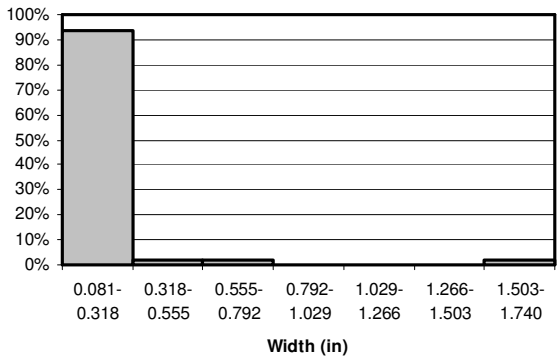

Figure 2.26 Average width distribution for all simulations run from the baseline case

Table 2.17 Statistics of average width with outliers disregarded

Minimum	0.08	in
Maximum	0.34	in
Median	0.19	in
Mode	0.19	in
Average	0.18	in
Std. Dev.	0.04	in
Count	45	

disregarded (Figure 2.27). Of the three cases that comprise the outliers with an average width less than 0.12 in, two of them occur with an increase of the leakoff coefficient (1.0 x 10^{-4} ft√min and 5.5 x 10^{-4} ft√min). The other case occurred when the pumping rate was decreased to 6 BPM. The largest width (0.34 in) occurred when the limestone modulus was decreased to 0.5 Mpsi.

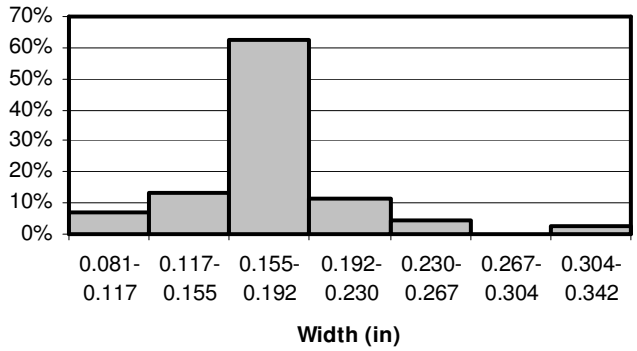

Figure 2.27 Distribution of average fracture width with outliers disregarded

Fracture Conductivity Distribution

Ninety-four percent of the trials resulted in a fracture with an average conductivity of less than 1305 md-ft (Figure 2.28). The average conductivity for all of the simulations is skewed to the left due to some exceedingly high values for cases where the leakoff coefficient was increased to1.0 x 10^{-2} ft√min and 5.5 x 10^{-2} ft√min and tip screenout occurred. These two simulations fall beyond one standard deviation (+/- 1284 md-ft) of the mean (718 md-ft) and were treated as outliers. Ignoring these two simulations, the average conductivity for the remaining trials is 470 md-ft with a median value of 394 md-ft and a mode of 396 md-ft, the same average conductivity as the baseline case (Table 2.18). Fifty-one percent of the average conductivity values occur in the range of 338 md-ft to 514 md-ft and 80% of the values are less than 514 md-ft (Figure 2.29). The five cases where the average conductivity is greater than 866 md-ft occurred when proppants of varying size and strength were used (12-20 sand, 16-30 sand, 16-30

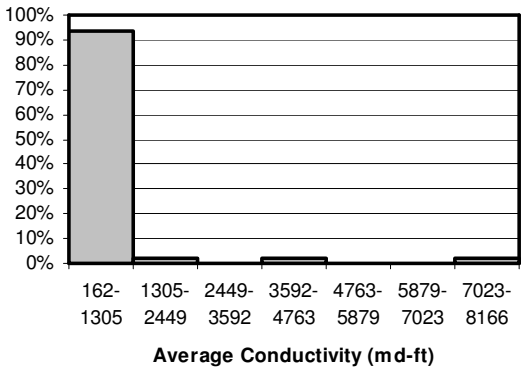

Figure 2.28 Average conductivity for all simulations run from baseline case

Table 2.18 Statistics of average conductivity

Minimum	162	md-ft
Maximum	1394	md-ft
Median	394	md-ft
Mode	396	md-ft
Average	470	md-ft
Stdev	292	md-ft
Count	45	

RCSandPC, 20-40 Int_Strength, and 20-40 Bauxite). The four cases where the average conductivity is between 514 and 866 md-ft occur with an increase of the leakoff coefficient (1.0 x 10^{-3} ft√min), an increased pumping rate (150 BPM), the fracturing fluid with the highest viscosity (50# X-Link), as well as a the case with the lowest value for limestone modulus (0.5 Mpsi).

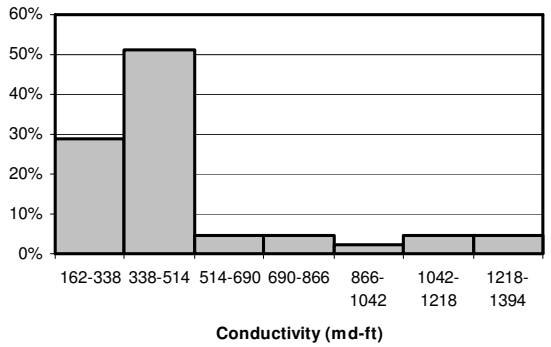

Figure 2.29 Distribution of fracture conductivity with outliers disregarded

Length vs. Width relationship

The average width was plotted against propped length for all of the trials run from the baseline case, with the exception of the two outlier cases where tip screen out occurred. There is a trend where the width decreases as length increases (Figure 2.30). There is considerable variation at lengths less than 225 ft. The correlation between width and length increases as lengths exceed 225 ft. One notable outlier occurs at a half length of 175 ft and a width of 0.35 in. This fracture geometry is predicted in the run using a low limestone modulus (0.5 Mpsi).

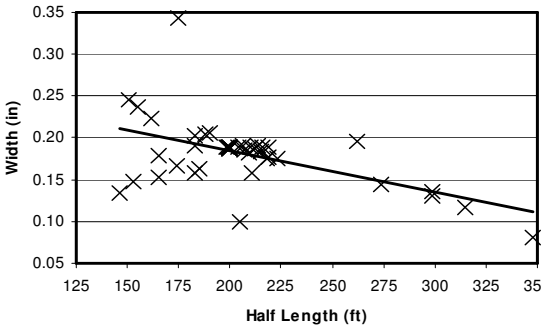

Figure 2.30 Average fracture width vs. propped length. Line represents a general trend of reduction in fracture width with increase in length.

Width vs. Conductivity Relationship

The average conductivity was plotted against the average width for all simulations except the two tests that resulted in outliers (Figure 2.31). The general trend is an increase in conductivity with an increase in fracture width. However, five trials resulted in a large increase in conductivity without an increase in fracture width (box in Figure 2.31). These

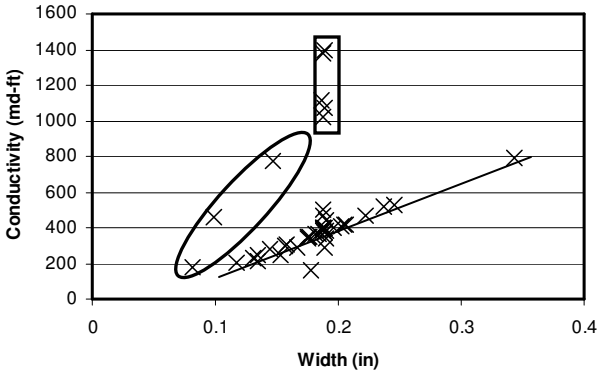

Figure 2.31 Relationship between average width and average conductivity. Points within box are trials were the proppant varied. Points within the oval are tests where the leakoff varied.

results occurred when different proppants were simulated (12-20 sand, 16-30 sand, 16-30 RCSandPC, 20-40 Int_Strength, and 20-40 Bauxite). The conductivity tended to increase with increasing proppant strength and decreasing size. Three other simulations appear to have a greater increase in conductivity as width increases than the majority of the trials (oval in Figure 2.31). These trials occur when the leakoff coefficient increased (1.0×10^{-4} ft√min, 5.5×10^{-4} ft√min, and 1.0×10^{-3} ft√min).

Net Pressure Distribution

The log transform distribution of the net pressure was calculated for all of the time steps output from the simulation trials (Figure 2.32). The calculated net pressure ranged from 31 psi for a simulation where the limestone modulus was low (0.5 Mpsi) to 38582 psi for a simulation with a high leakoff coefficient (1.0×10^{-2} ft√min) and tip screenout occurred. Ninety-three percent of the net pressure values range from 160 psi to 1500 psi (Figure 2.32). There were 21 values of net pressure less than 80 psi that occurred when the limestone modulus was low (0.5 Mpsi). Net pressures in the range of 80 psi to 160 psi occurred when the leakoff coefficient was near the midpoint of the range tested (1.0×10^{-4} ft√min, 5.5×10^{-4} ft√min) or in the 1500 ft thick limestone formation. All of the net pressures greater than 1500 psi are a result of high leakoff coefficients (5.5×10^{-3} ft√min, 1.0×10^{-2} ft√min) where tip screenout occurred.

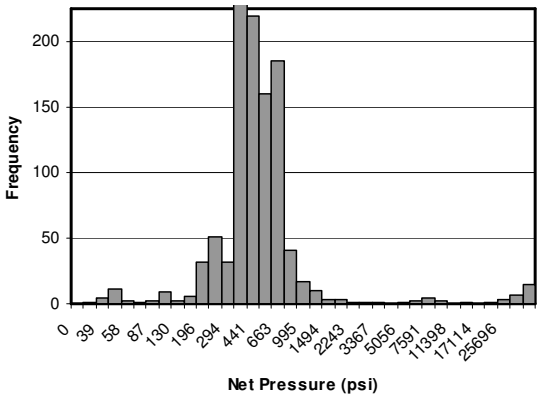

Figure 2.32 Distribution of log net pressure for all simulations. The category 294 psi to 360 psi has 410 occurrences.

In order for the fracture to propagate in the simulation with the low limestone modulus (0.5 Mpsi), the pressure needed to be 30 psi greater than confining pressure. A net pressure of 160 psi was needed to propagate the majority of fractures. To prevent unintentional propagation of fractures in the limestone formation during acid dissolution, pressures should not exceed 30 psi above the confining pressure for low modulus formations and should not exceed 80 psi for formations with a higher modulus. If tip screenout treatments are planned, higher pressures within the fracture are predicted. This would influence the tolerances needed for the equipment used in creating the fracture.

Fluid Loss Coefficient

The fracture properties of half-length, propped length and average fracture conductivity were plotted against the seven variations in the leakoff coefficient (Figure 2.33). For the trials where the leakoff coefficient was greater than 1.0×10^{-4} ft√min, the fracture half length decreased with increasing leakoff coefficient. Conversely, the average

fracture conductivity increased from 176 md-ft to 8166 md-ft as the leakoff coefficient increased from 1.0 x 10^{-4} ft√min to 1.0 x 10^{-2} ft√min. The increase in conductivity was steeper for higher values of the leakoff coefficient. The conductivity increased from 4432 md-ft at a leakoff of 5.5 x 10^{-3} ft√min to 8166 md-ft at a leakoff of 1.0 x 10^{-2} ft√min.

Values of leakoff coefficient less than 1.0 x 10^{-4} ft√min exhibit more detail (Figure 2.34). The fracture half- length is greatest at a leakoff coefficient of 1.0 x 10^{-4} ft√min and decreases as the leakoff coefficient increases. The average fracture conductivity is the least (176 ft√min) at a leakoff coefficient of 1.0 x 10^{-4} ft√min. The conductivity increases as fracture conductivity increases and decreases.

The fracture half-length at the time pumping was stopped as well as the final length was plotted against the leakoff coefficient (Figure 2.35) to explain the maximum fracture length at a leakoff coefficient of 1.0 x 10^{-4} ft√min (Figures 3.18, 3.19). The curve created by length at "pump off" is relatively smooth with fracture half-length decreasing as the leakoff coefficient increases. The final length deviates from the length at pump off for leakoff coefficients less than 1.0 x 10^{-3} ft√min (Figure 2.35). For these cases the fracture continued to propagate after the pumping schedule in the simulation was completed. The fracture continued to grow for approximately 196 ft when the leakoff was 1.0 x 10^{-4} ft√min.

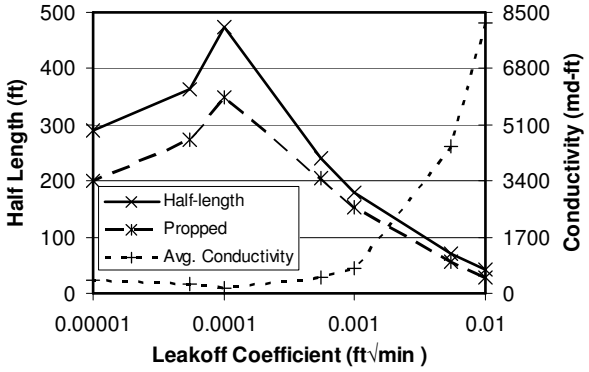

Figure 2.33 Relationship between leakoff coefficient and fracture properties.

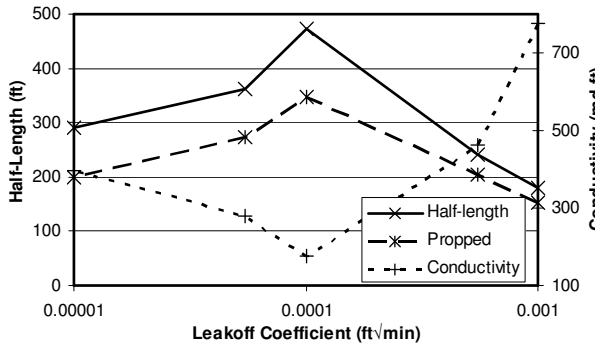

Figure 2.34 Leakoff coefficients less than 0.001 ft√min and fracture characteristics.

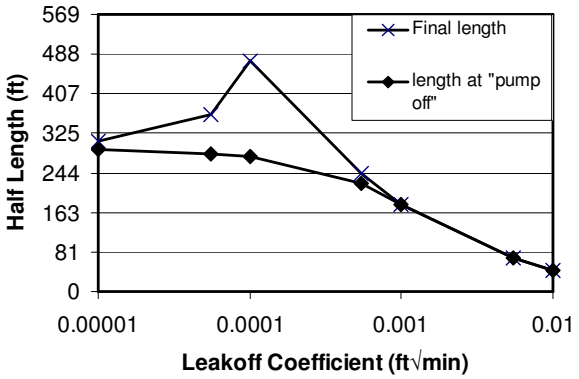

Figure 2.35 Fracture half-length at end of pumping and final length for varying leakoff coefficients.

Fracture growth after "pump off" is a result of the low leakoff and the compressive stress of the formation. During pumping, the fracture width increased because the pumping pressure exceeded the compressive stress. The pressure within the fracture remains high when the pressure from the pump is shut off because the fracturing fluid is unable to leak into the formation. The fracturing fluid is slow to leak into the formation because of the low leakoff coefficient. In response to the pressure difference between the fracturing fluid and the formation, the fracture continues to propagate.

Depth

The fracture half-length, propped length and average conductivity were calculated for target depths of 4000, 6000 and 8000 ft. The fracture half-length and propped length remain constant as the depth of the fracture increases (Figure 2.36). For all of the cases, the total fracture half-length is about 100 ft greater than the propped length. However, the fracture conductivity decreases from 499 md-ft at a depth of 4000 ft to 293 md-ft at a depth of 8000 ft. Stress on the proppant increases with depth and results in elastic deformation of the proppant as well as

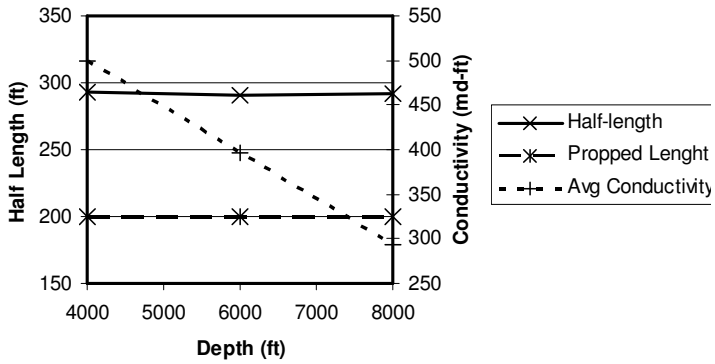

Figure 2.36 Variations in fracture properties with changes in depth

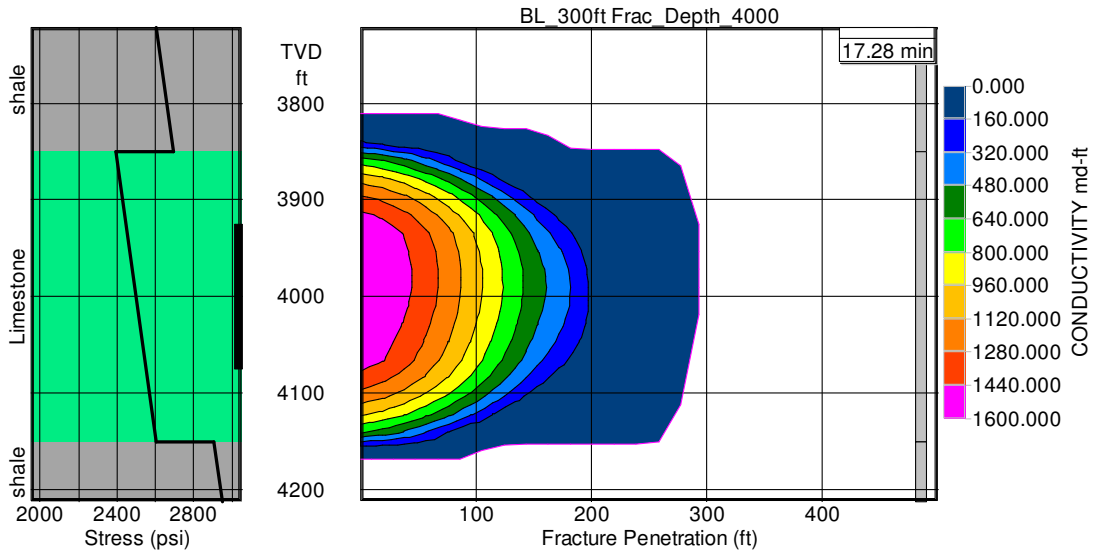

Figure 2.37 Conductivity for a fracture at a target depth of 4000 ft.

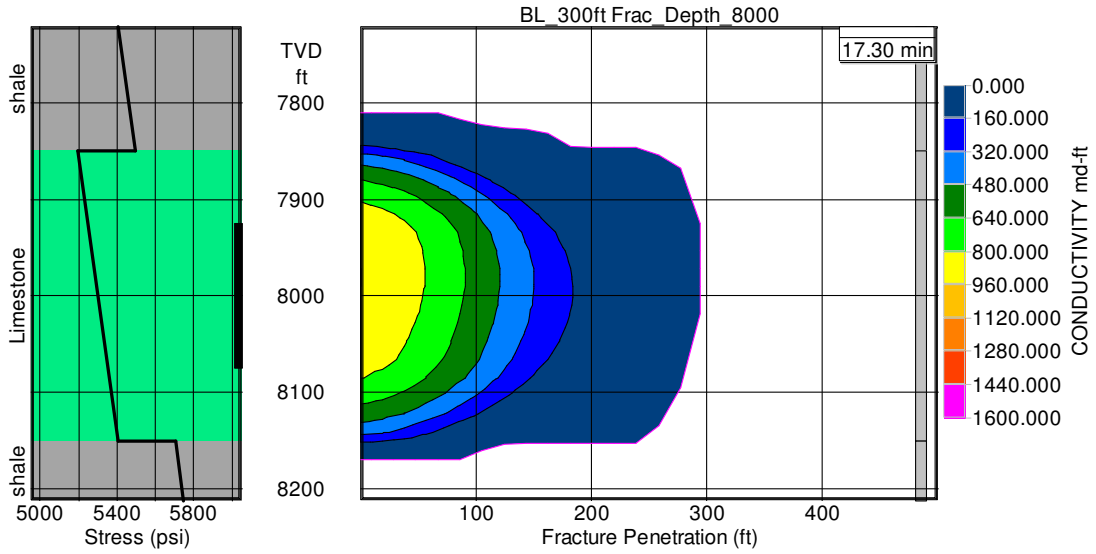

Figure 2.38 Conductivity for a fracture at a target depth of 8000 ft.

increased embedment of the proppant into the fracture walls, reducing fracture conductivity.

The fractures at 4000 ft and 8000 ft have similar length and width dimensions, but the distribution of fracture conductivity is different. The average conductivity for the fracture at the 4000 ft depth (Figure 2.37) is greater than the average fracture conductivity at the 8000 ft depth (Figure 2.38). There is also a difference in the stress profiles between the two different depths. Both stress profiles vary by the same gradient, but the average compressive stress at 4000 ft is 2500 psi while the average compressive stress at 8000 ft is 5300 psi. As the stress increases, the fracture conductivity decreases.

Stress Contrast

The variation of the difference in stress between the limestone target formation and the adjacent layer affected horizontal fracture length as well as vertical height growth (Figure 2.39). Where the stress difference is negative, the stress in the limestone is less compressive than the stress in the adjacent layers. As the stress in the limestone increased to match that of the adjacent layer, the fracture half-length decreased from 313

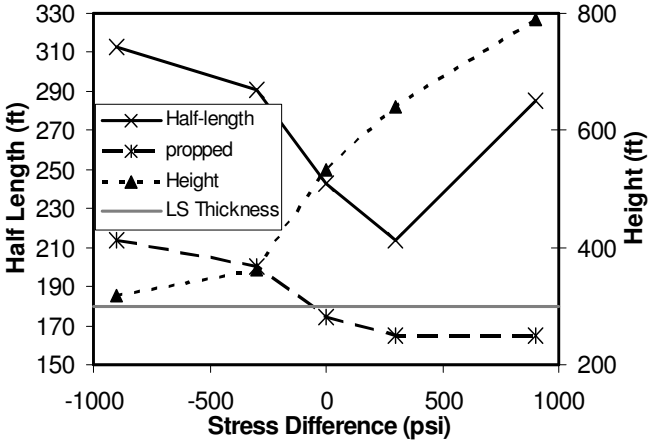

Figure 2.39 Effect of stress differences between adjacent layers and fracture dimensions

ft for the baseline to 243 ft for zero stress difference while the propped length decreased from 214 ft for the baseline to 174 ft. For these cases, the overall fracture height growth increased from 318 ft for the baseline to 533 ft for zero stress difference (Figures 3.22). The fracture half-length decreases to 214 ft at a stress difference of 300 psi then increases to 285 ft at a stress difference of 900 psi. The propped length decreases to 165 ft at a stress difference of 300 psi and 900 psi.

The fracture half-length is 313 ft and the fracture intrudes 14 ft vertically into the upper formation and 4 feet into the lower formation when the compressive stress in the limestone is 900 psi less than that the stress in the adjacent layers (Figure 2.40). Decreasing the stress difference to 300 psi reduces the fracture half-length to 291 ft, and extends the vertical intrusion 50 ft into the upper layer and 13 feet into the lower layer (Figure 2.41).

This trend is maintained when the stresses are continuous between the limestone and the adjacent layers. In this case, the half-length is 243 ft, and it intrudes 140 ft vertically into the upper shale layer and 93 feet into the lower formation (Figure 2.42). For this simulation, the fracture was generally radially symmetric with the vertical fracture growth slightly greater than the horizontal length. The upward vertical growth is greater than the downward growth because of the gradient (0.7 psi/ft) in confining stress (Figure 2.42).

The fracture half-length is 214 ft and the fracture intrudes 204 ft vertically into the upper shale layer and 135 feet into the lower formation when the stress difference is 300 psi (Figure 2.43). There are two lobes of increased conductivity, one in the limestone formation and one in the upper formation (Figure 2.43).

The fracture half-length is 285 ft with 233 ft of intrusion into the upper layer and 257 feet into the lower formation when the stress difference is 900 psi (Figure 2.44). The predicted fracture has a greater lateral intrusion into the lower formation, but has higher

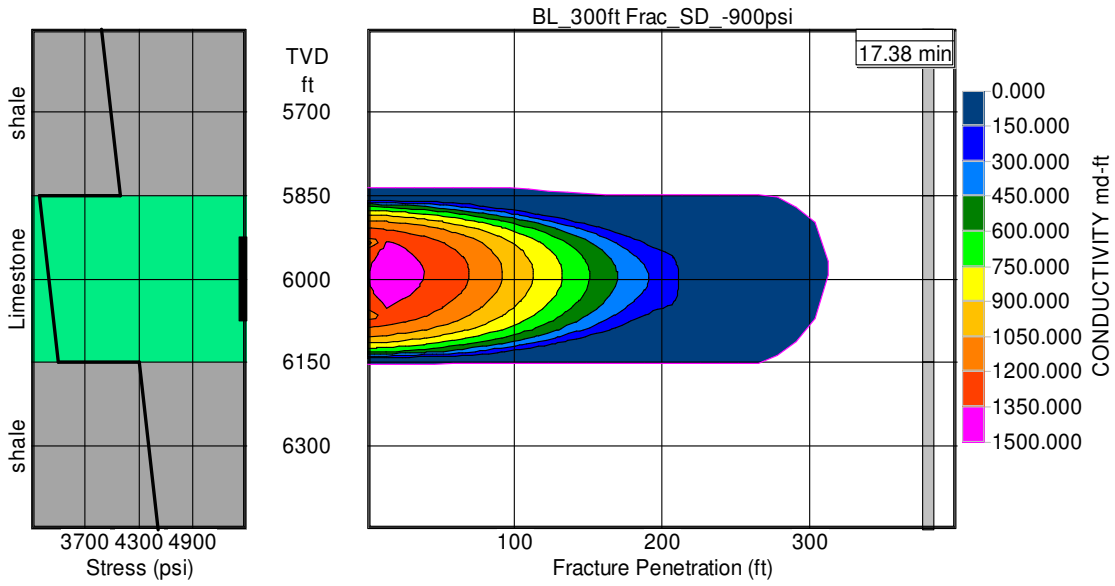

Figure 2.40 Fracture conductivity for a simulation where the limestone stress is 900 psi less than the shale layers, 3:1 horizontal exaggeration.

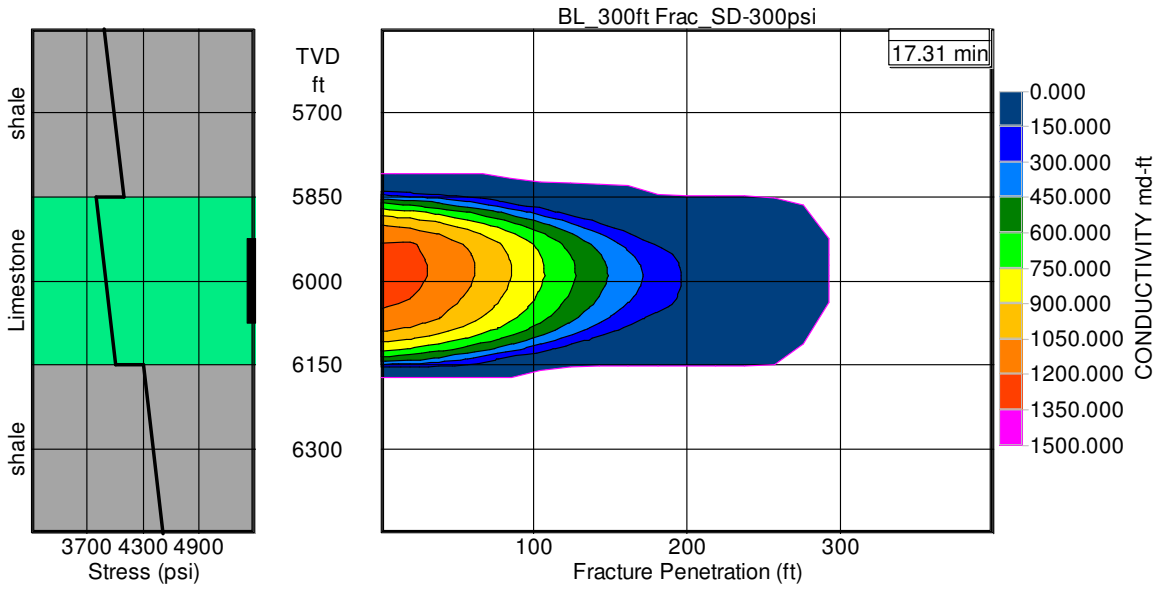

Figure 2.41 Fracture conductivity for a simulation where the limestone stress is 300 psi less than the shale layers, 3:1 horizontal exaggeration.

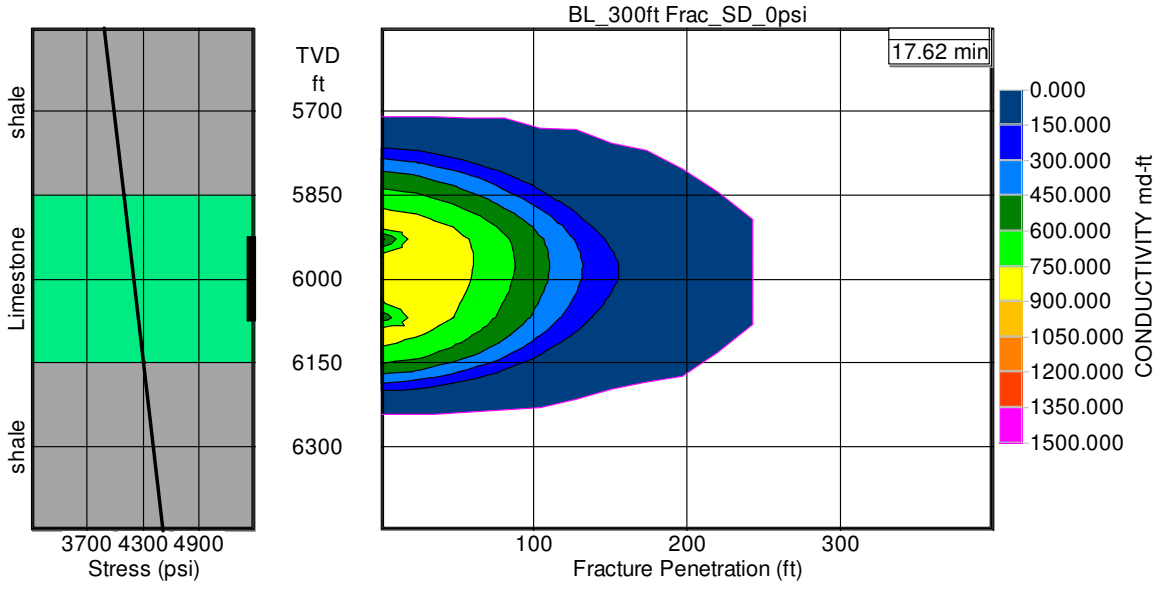

Figure 2.42 Fracture conductivity for a simulation with no stress difference between the limestone and the shale layers, 3:1 horizontal exaggeration.

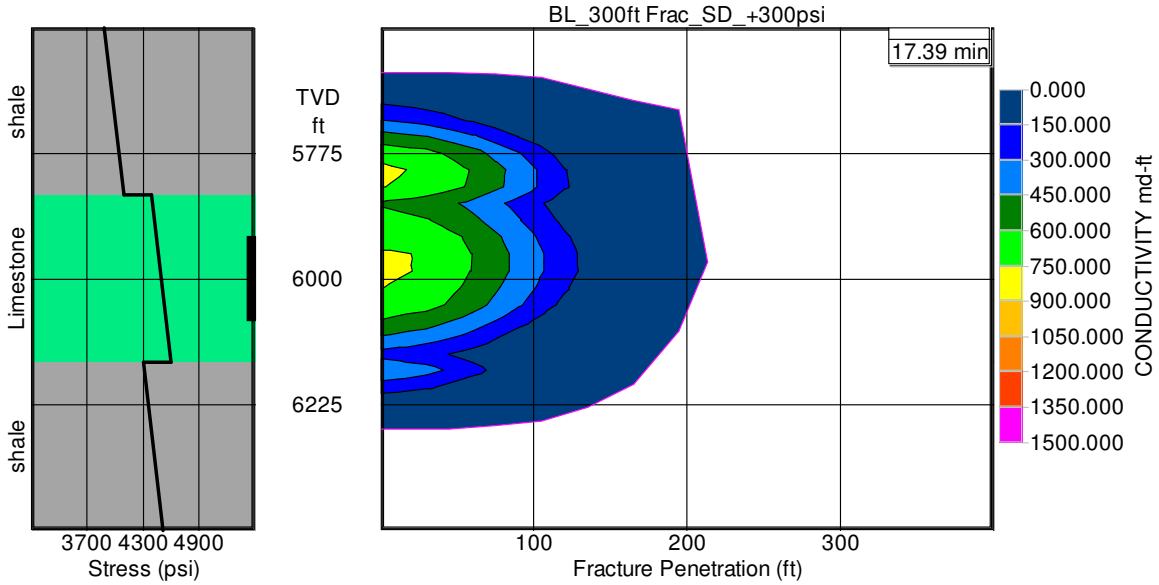

Figure 2.43 Fracture conductivity for a simulation where the limestone stress is 300 psi greater than the shale layers, 3:1 horizontal exaggeration.

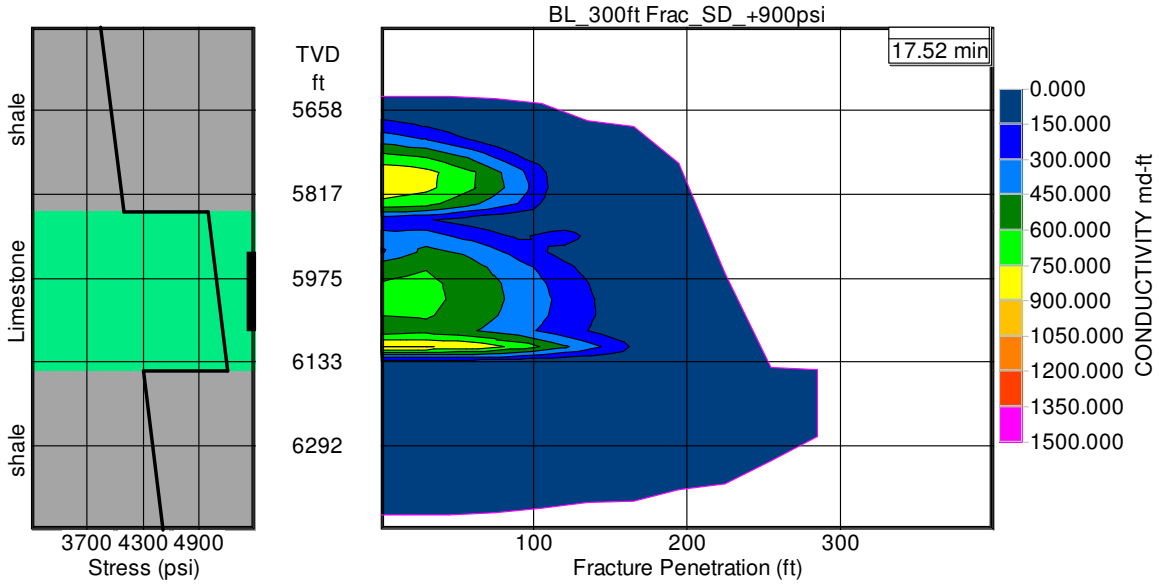

Figure 2.44 Fracture conductivity for a simulation where the limestone stress is 900 psi greater than the shale layers, 3:1 horizontal exaggeration.

conductivity regions in the upper formation (Figure 2.44). For both of the cases where the stress in the limestone is greater than the stress in the adjacent layers, the fracture has lobes of higher conductivity, indicating different lobes of proppant placement. Due to the higher stress in the limestone, the fracturing slurry migrates to areas of least stress,

resulting in the taller fractures and lobes in the adjacent layers where the proppant flowed (Figures 2.43, 2.44). Shale normally has a higher in-situ stress; however, inversions of this relationship have been reported (Shumbera et al., 2003).

The simulations where the stress in the limestone was less than the stress in the adjacent shale resulted in fractures with intrusion less than 50 ft into the upper layer. Also, the fracture conductivity is greater than 750 md-ft for most of the fractures in these simulations (Figure 2.40, 2.41). When there was no stress difference between the layers, vertical fracture growth was unimpeded and the fracture was nearly radially symmetric with a fracture conductivity 750 md-ft out to approximately 60 ft (Figure 2.42). The simulations where the stress in the limestone was greater than the stress in the adjacent shale layers resulted in fractures with increased vertical fracture growth with lobes where the conductivity was 750 md-ft, but the overall conductivity is less than in the other simulations (Figure 2.43, 2.44).

For variations in the stress difference between layers, when the stress in the limestone is less than the stress in the adjacent layer, the fractures were vertically confined, had longer half-length, and areas of higher fracture conductivity (Figure 2.40, 2.41). When the stress between the formations was the same, the fracture was generally radially symmetric with the fracture conductivity in all areas of the fracture less than 900 md-ft (Figure 2.42). When the stress in the limestone is greater than the stress in the adjacent layers, there was greater vertical growth than horizontal length and the fracture conductivity was less than 900 md-ft for the entire fracture with small regions were the conductivity is greater than 750 md-ft (Figures 2.43, 2.44)

Adjacent Formation Physical Properties

The modulus and fracture toughness for the adjacent layers were varied to represent the range of these properties reported for shale (Table 2.3) and sandstone (Table 2.4). The intrusion of the fracture into the upper formation was plotted as a function of elastic modulus for different values of fracture toughness (Figure 2.45). The intrusion into the upper layer is 35 ft when the modulus is 0.1 Mpsi, 48 ft when the modulus is 4.3 Mpsi and 51 ft when the modulus is 8.5 Mpsi and the fracture toughness is 246 psi√in (Figure 2.45). As shown in Figure 2.45, the intrusion into the upper layer is 25 ft when the modulus is 0.1 Mpsi, 43 ft when the modulus is 4.3 Mpsi and 46 ft when the modulus is 8.5 Mpsi and the fracture toughness is 1292 psi√in. The intrusion into the upper layer is 27 ft when the modulus is 0.1 Mpsi, 36 ft when the modulus is 4.3 Mpsi and 43 ft when the modulus is 8.5 Mpsi and the

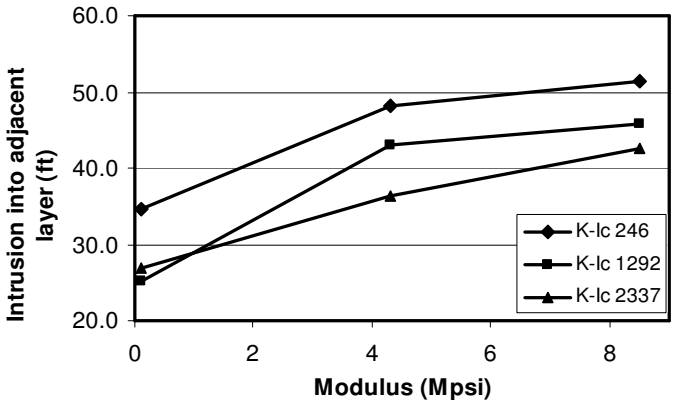

Figure 2.45 Intrusion into upper layer as a function of fracture toughness for different moduli

fracture toughness is 2337 psi√in (Figure 2.45). The intrusion into the upper layer generally increases with an increase in modulus of the upper layer. The increase in intrusion is approximately 20 ft with an increase in modulus of 8 Mpsi. Lower values of fracture toughness in the adjacent layers resulted in greater intrusion into the upper formation.

Fracture intrusion into the upper formation was plotted against fracture toughness variations in the adjacent layer for different values of the elastic modulus of the adjacent layer (Figure 2.46). As shown in Figure 2.46, the fracture intrudes 35 ft into the upper layer when the K_{IC} is 246 psi√in, 25 ft when the K_{IC} is 1292 psi√in and 27 ft when the K_{IC} is 2337 psi√in and the modulus is 0.1 Mpsi. The fracture intruded 48 ft into the upper layer when the K_{IC} is 246 psi√in, 43 ft when the K_{IC} is 1292 psi√in and 36 ft when the K_{IC} is 2337 psi√in and the modulus is 4.3 Mpsi (Figure 2.46). The fracture intruded 51 ft into the upper layer when the K_{IC} is 246 psi√in, 46 ft when the K_{IC} is 1292 psi√in and 43 ft when the K_{IC} is 2337 psi√in and the modulus is 8.5 Mpsi (Figure 2.46). Intrusion into the upper formation decreased as the adjacent layer fracture toughness increased. The fracture intrusion increased with increasing modulus. The least intrusion into the upper layer (25 ft) occurred when the elastic modulus was the smallest and the fracture toughness was 1292 psi√in. The greatest fracture intrusion (51 ft) occurred when the elastic modulus was the greatest and the fracture toughness was the least (Figure 2.46).

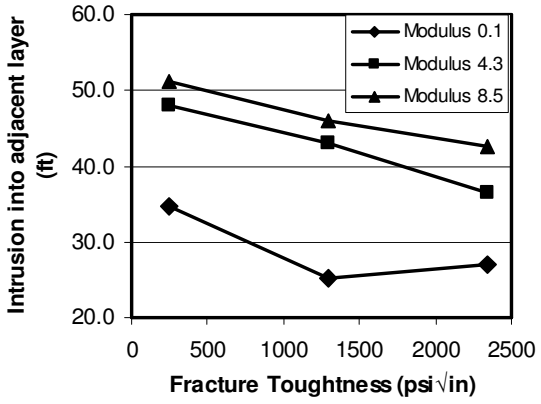

Figure 2.46 Intrusion into upper layer for different moduli and fracture toughness values of the adjacent layers

The results of variations of physical properties of the limestone were calculated when the lateral stress in the limestone was 300 psi less than the adjacent layers. The simulations were rerun with zero stress difference between the layers to isolate the effects of the modulus and fracture toughness. The results of intrusion into the upper adjacent layer as a functions of elastic modulus and fracture toughness (Figure 2.47) and fracture intrusion into the upper layer as a function of fracture toughness for different values of the elastic modulus (Figure

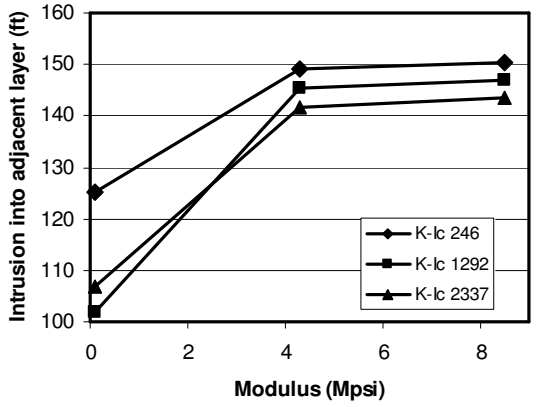

Figure 2.47 Intrusion into upper adjacent layer as a function of modulus and fracture toughness (adjacent layer) with zero stress difference between layers

2.48) exhibit the same trends as the trials with a stress contrast. Fracture intrusion into the upper layer increased with an increasing modulus and decreased with an increase of fracture toughness. The major difference is that the fracture penetrated about 3.5 times farther into the upper adjacent layer when the stresses are equal. Based on these results, the stress difference between layers has a greater effect on vertical height growth than the elastic modulus and fracture toughness of the overlying formation.

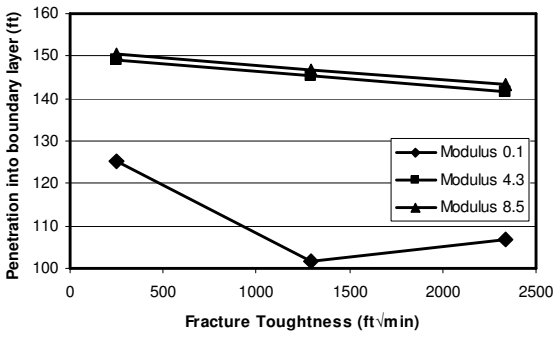

Figure 2.48 Intrusion into upper adjacent layer as a function of Modulus for different values of fracture toughness with zero stress difference between the layers

Limestone Physical Properties

The elastic modulus and fracture toughness were varied according to the expected range for limestone. The fracture half-length increased from 223 ft to 308 ft as the limestone modulus increased (Figure 2.49). The propped length of the fracture increased as well from 161 ft to 298 ft, approximately 70% of the penetrated length for the same simulations. The average conductivity decreased from 794 md-ft to 298 md-ft as the limestone elastic modulus increased.

The variation in the limestone fracture toughness had a minor effect on fracture half-length and propped length. The horizontal fracture half-length increased approximately 10 ft, from 291 ft to 301 ft, as the fracture toughness varied from 350 psi√in to 1800 psi√in (Figure 2.50). There was an increase in average fracture conductivity

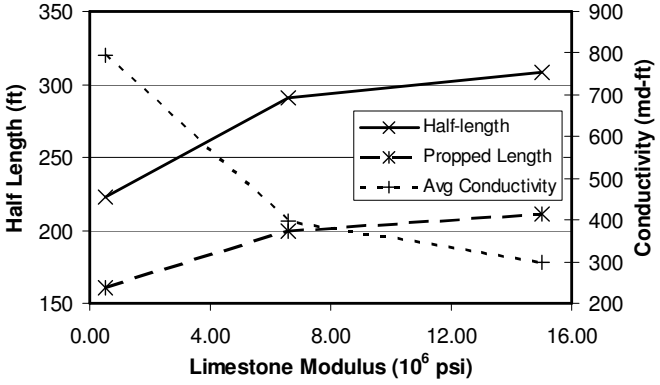

Figure 2.49 Effects of variations in limestone modulus on half-length, propped length and average conductivity

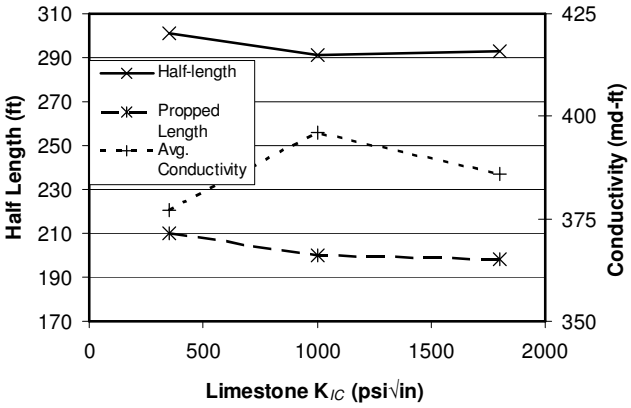

Figure 2.50 Effect of expected variations in limestone fracture toughness on half-length and conductivity.

from 377 md-ft at a fracture toughness of 350 ft√min to 396 md-ft when the fracture conductivity is 1000 ft√min. When the fracture toughness increased to 1800 ft√min, the fracture conductivity was 386 md-ft, resulting in a gentle maximum in conductivity when the fracture toughness is 1000 ft√min. The range of conductivity for the trials of fracture toughness is 25 md-ft so the spike is minor. The elastic modulus has a greater effect than the fracture toughness on fracture geometry for the range evaluated here.

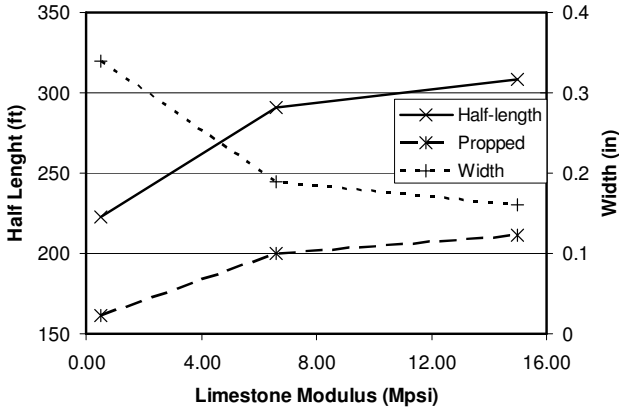

Figure 2.51 Effects of variations in Limestone modulus on fracture half-length and width.

To examine the effect of variations in limestone modulus in more detail, the fracture half-length and width were plotted against limestone modulus (Figure 2.51). The fracture width was greater at lower values of the limestone modulus and the width decreased as the modulus increased. Increasing the modulus reduces the opening of mode I fractures.

Limestone Thickness

Variations in the thickness of the limestone formation were also simulated. Reducing the limestone thickness to 60 ft with a fracture design length of 300 ft represents a situation where the ideal fracture length is 5 times greater than the formation thickness. The result is a triangular-shaped fracture significantly intrudes into the adjacent layers (Figure 2.52). The fracture laterally penetrates 388 ft, 30% farther than the baseline case, but it penetrates 173 ft into the upper layer and 151 ft into the lower layer. There is a wedge of higher conductivity that cuts 100 ft into the limestone formation as well as intruding into the upper and lower layers.

The baseline case represents a situation where the proposed fracture length is the same as the formation thickness and was described above (Figure 2.53). A third simulation was run where the limestone thickness was 1500 ft, five times greater than the proposed fracture length. This situation results in a fracture that has a half-length of 265 ft and a total vertical height of 512 ft (Figure 2.54). The vertical height was 40% larger than the baseline case, yet there was more than 450 ft of clearance from the upper formation and 530 ft of clearance from the lower formation. There is a region of higher fracture conductivity near the borehole that decreases in a radial pattern from the center.

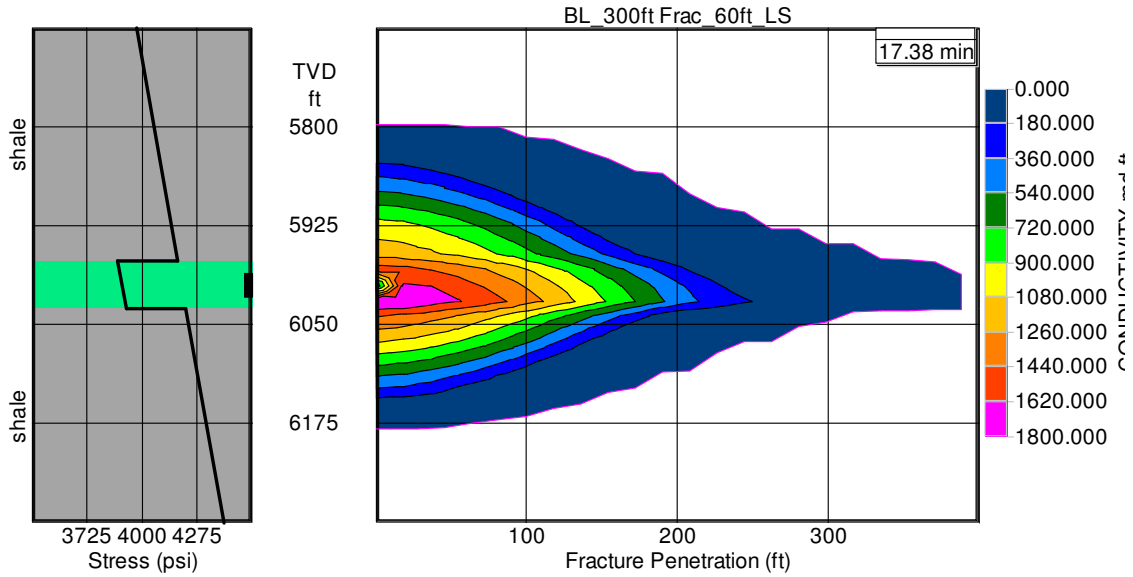

Figure 2.52 Conductivity for a fracture in a 60 ft thick limestone formation.

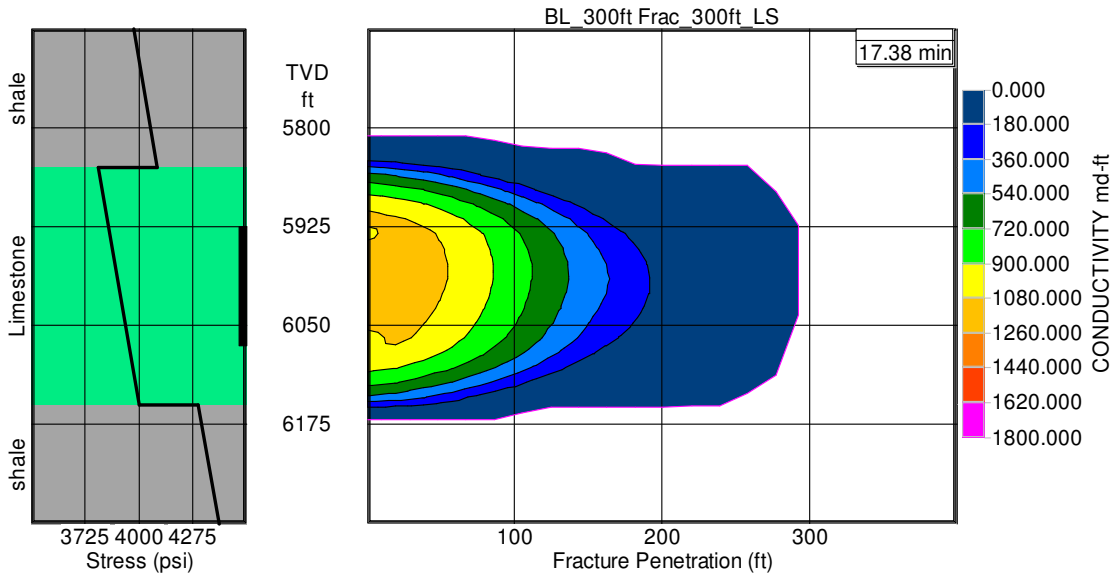

Figure 2.53 Conductivity for a fracture in 300 ft thick limestone.

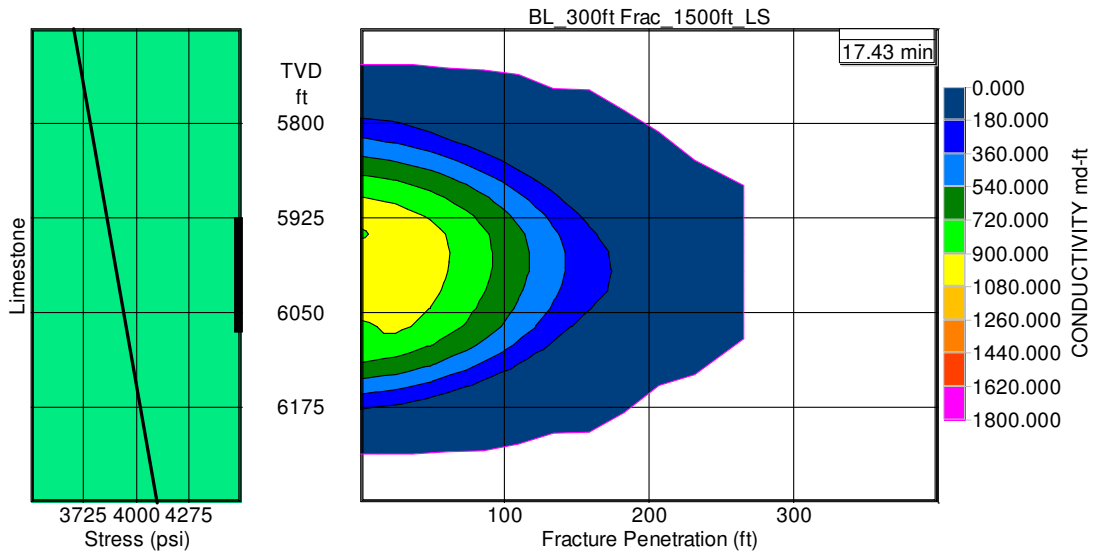

Figure 2.54 Conductivity for a fracture in 1500 ft thick limestone.

Perforated Interval

The perforated interval where the fracture was initiated was varied to understand how it can affect fracture dimensions. The fracture half-length exhibited minimal variation, but the propped length decreased as the perforated interval increased (Figure 2.55). The fracture height increased from 356 ft to 383 ft as the perforated interval increased from 30 ft to 300 ft. A ten-fold increase in the perforated interval resulted in increased height growth of only 27 ft. Although there was minimal variation in fracture height when the perforated interval was changed, reducing the perforated interval from 300 ft to 30 ft did reduce the intrusion into the upper formation from 64 ft to 36 ft (Figure 2.56).

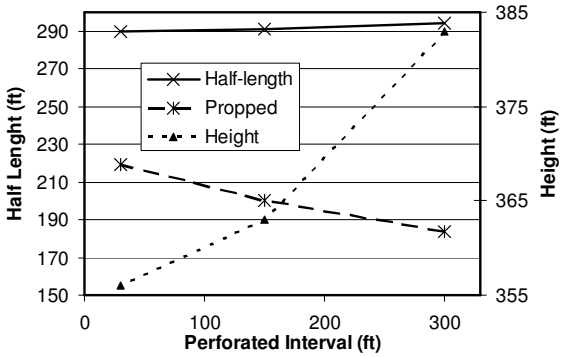

Figure 2.55 Effects of different perforated intervals on fracture half-length and height.

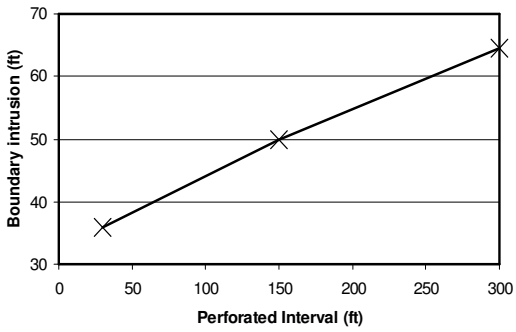

Figure 2.56 Intrusion into upper layer with variation of the perforated interval length.

Pumping Rate

Fracture half-length and propped length decrease as the pumping rate increases (Figure 2.57). There is a steep decline in fracture length when the pumping rate increases from 6 BPM to 30 BPM, but the decrease in fracture length is less steep when the pumping rate increased from 30 BPM to 150 BPM. The average conductivity increases from 208 md-ft to 525 md-ft as the pumping increases. There is a sharp increase in average conductivity when the pumping rate increased from 6 BPM to 30 BPM and the increase was less steep as the pumping rate increased from 30 BPM to 150 BPM. There appears to be more variability in fracture properties at lower pumping rates that at higher pumping rates.

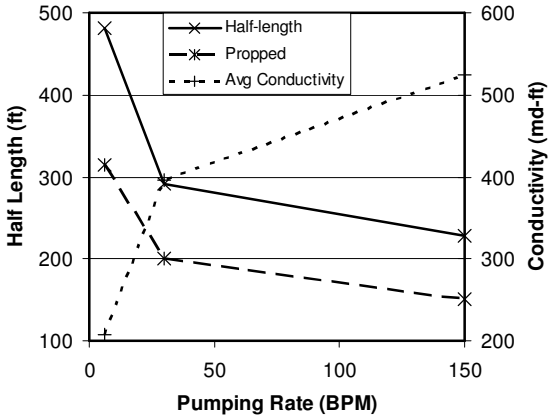

Figure 2.57 Effects of different pumping rate on fracture length and conductivity.

The lower pumping rate of 6 BPM produces a longer fracture with a lower average conductivity and a lower conductivity distribution (Figure 2.58). The pumping rate of 30 BPM is the baseline case and the half-length is less than when the pumping rate is 6 BPM, and the average conductivity is greater (Figure 2.59). A pumping rate of 150 BPM resulted in the shortest fracture half-length with the highest conductivity (Figure 2.60). The time needed to create the fracture and deliver the proppant decreased as

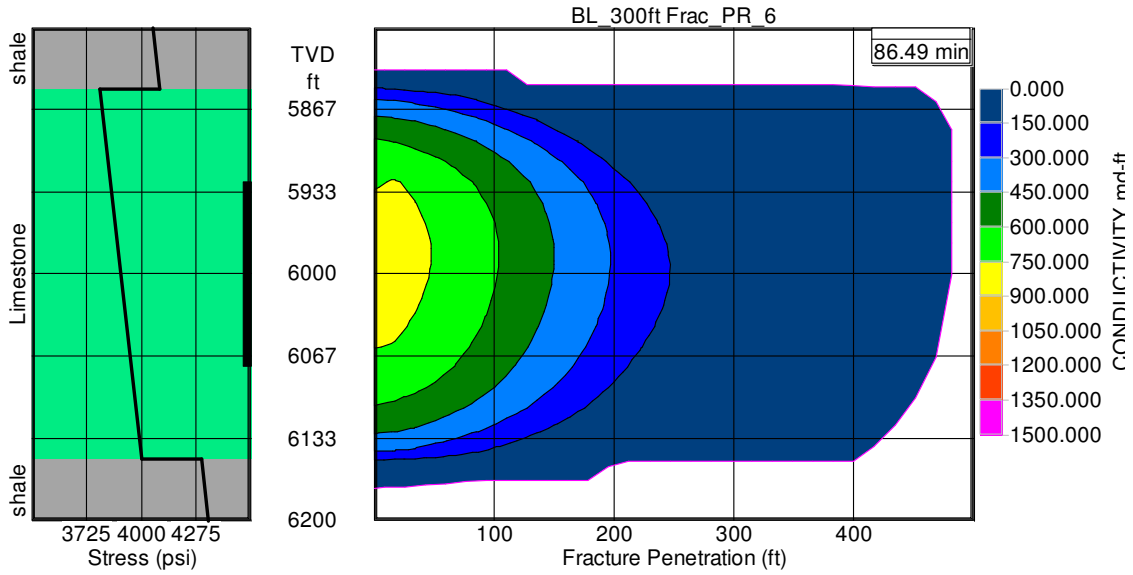

Figure 2.58 Conductivity with a pumping rate of 6 BPM

pumping rate increased. The time required to create the fracture also changed from 86.5 min with a pumping rate of 6 BPM, to 17.3 min for a pumping rate of 30 BPM at 3.5 min for a pumping rate of 150 BPM.

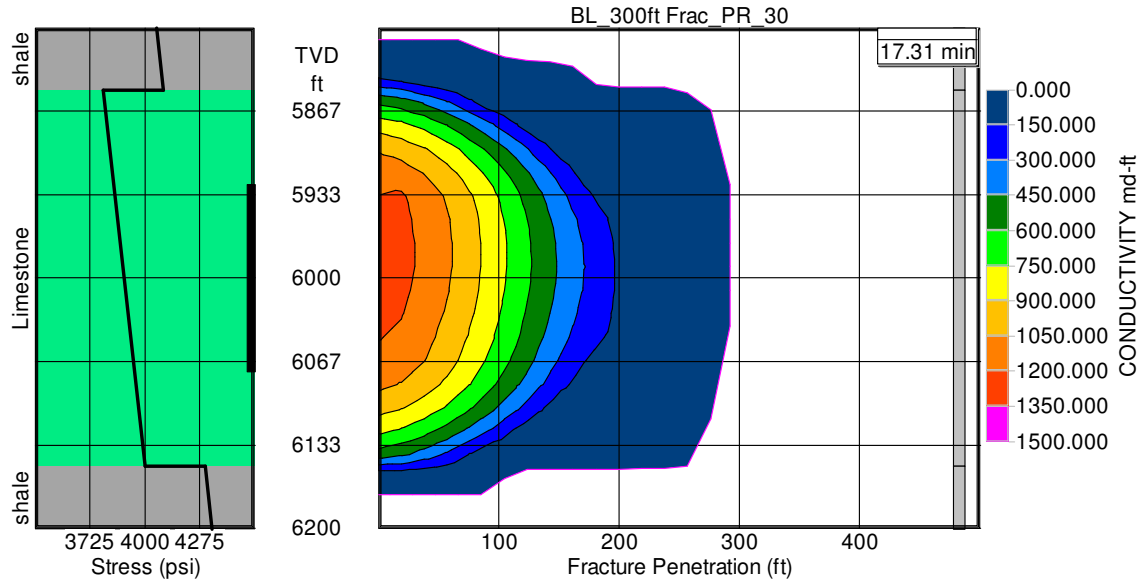

Figure 2.59 Conductivity with a pumping rate of 30 BPM

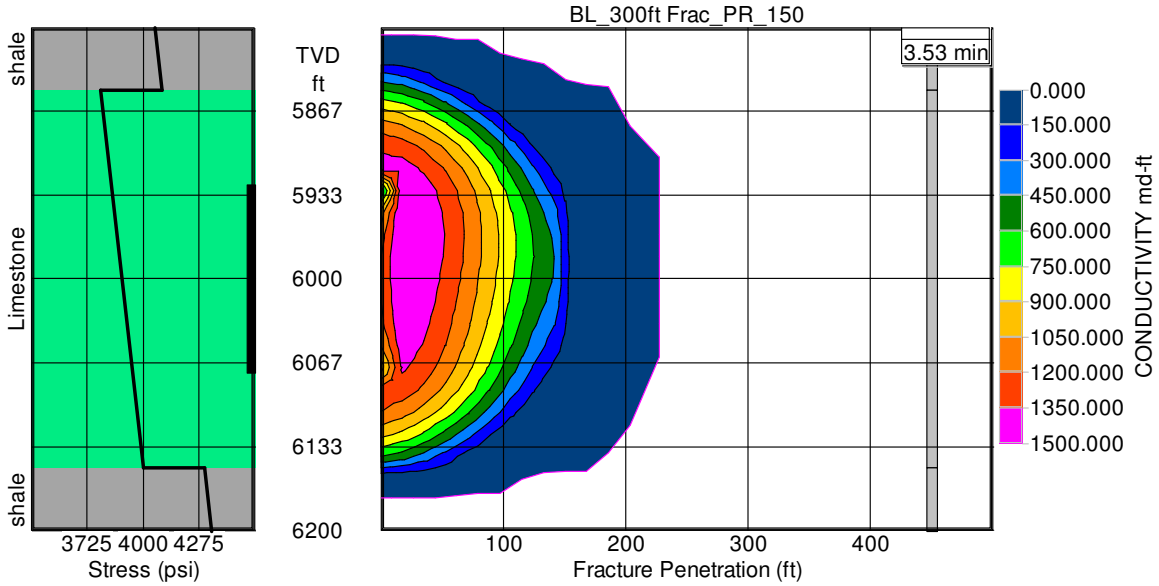

Figure 2.60 Conductivity with a pumping rate of 150 BPM

Fracturing Fluid

The fracturing fluid viscosity at formation temperature was used as the distinguishing characteristic of the different fluids in order to quantify the variation of the type of fracturing fluid utilized in the model. Fracture half-length, propped length and average conductivity were plotted against the viscosity of the fracturing fluid (Figure 2.61). As the viscosity of the fluid increased, the half-length decreased. At a viscosity of 45 cp the fracture half-length was 444 ft. When the viscosity increases to 840 cp the fracture length decreases to 227 ft. However, as the fluid viscosity increased the average fracture conductivity increased as well. At a viscosity of 45 cp the average conductivity was 243 md-ft. When the viscosity was increased to 840 cp, the average conductivity nearly doubles to 519 md-ft.

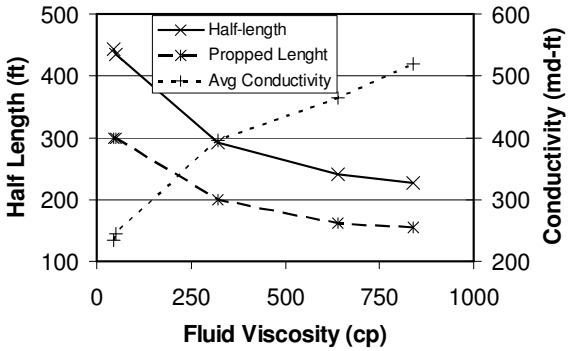

Figure 2.61 Effect of fracturing fluid viscosity on fracture half-length and average conductivity

Proppant Type

Proppant size and damage factor were the two characteristics used to quantify the effects of different proppants on fracture formation. The proppant size relates to a range of mesh sizes that the proppant falls between (Table 2.5). The damage factor is a dimensionless variable that relates to the strength of the proppant. A damage factor of 1 represents a material that is un-deformable or not crushed at any pressure (Table 2.5).

The average fracture conductivity was plotted as a function of the damage factor for different mesh sizes (Figure 2.62). Sand with a damage factor of 0.70 and a 20-40 mesh (0.066 in -0.033 in) size produces a fracture with an average conductivity of 470 md-ft. For the same sized bauxite with a damage factor of 0.85, the average conductivity increased to 1113 md-ft. For proppants of the same grain size, the average conductivity increases with an increasing damage factor.

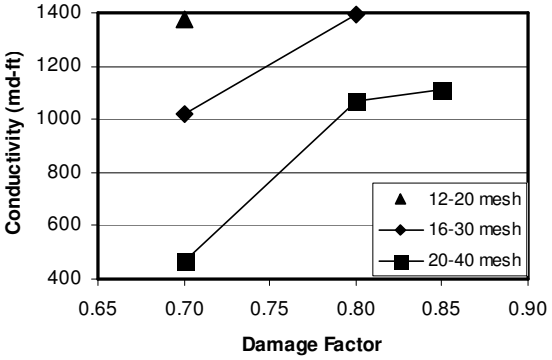

Figure 2.62 Average fracture conductivity as a function of damage factor for different sized proppants.

For proppants with the same damage factor, the average fracture conductivity increased with increasing mesh size for proppants. For sand with a damage factor of 0.70, the average conductivity is 470 md-ft for the 20-40 mesh (0.066 in -0.033 in). The average conductivity increases to 1019 md-ft for 16-30 mesh (0.047 in-0.023 in) and to 1377 md-ft for 12-20 mesh (0.033 in -0.017 in) (Figure 2.62).

1500 ft Fracture

A simulation was set up to create a fracture where the ideal half-length length was five times the thickness of the formation. For this case, all of the variables were the same as the baseline case with the exception of a pumping schedule intended to create at least a 1500 ft fracture half-length. This simulation resulted in a fracture with a half-length of 1731 ft and a vertical growth of 591 ft at the wellbore (Figure 2.63). The fracture intrudes more than 300 ft into the upper layer out to a horizontal distance of 255 ft where the intrusion height decreases to 50 ft. The intrusion into the upper layer is 20 ft beyond 700 ft from the well bore. The pressurized width of the fracture is greater than 0.4 in for the limestone formation out to a distance of 200 ft from the well bore. The fracture width decreases with length but the average width is greater than 0.19 in out to 1250 ft from the well bore.

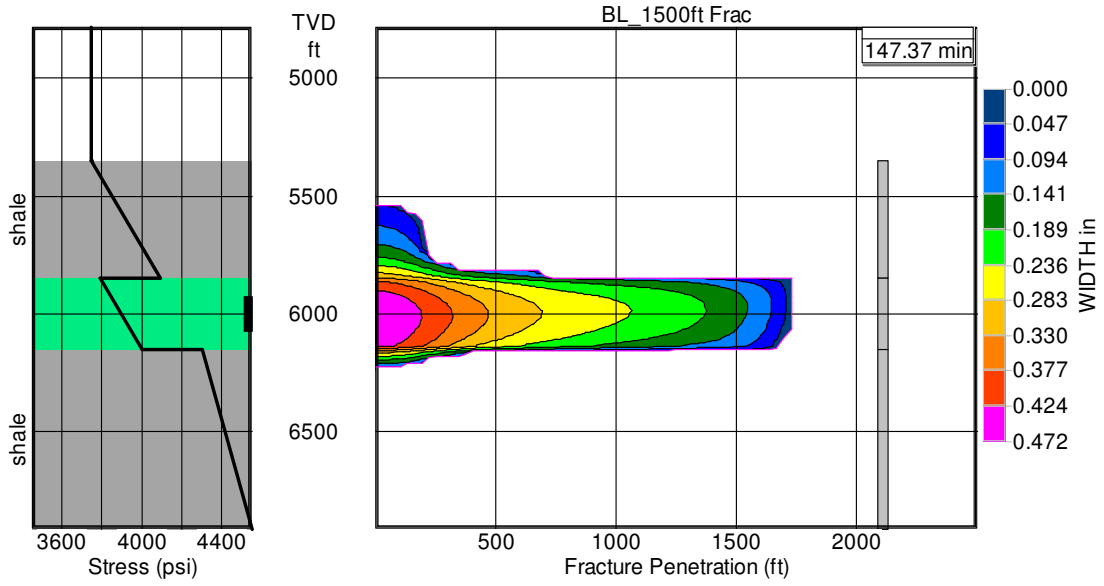

Figure 2.63 Fracture width for a fracture with a half-length greater than 1500 ft in a 300 ft thick limestone layer

The cross section of fracture width at the borehole is tear-drop shaped with a maximum width of 0.48 in at a depth of 6000 ft. The fracture width is generally greater than 0.40 in throughout the limestone formation but decreases as the fracture approaches the adjacent layer (Figure 2.64). The cross section is triangular-shaped in the upper formation, decreasing in width and reaching a maximum height at 5524 ft. There is less

intrusion into the lower layer than into the upper one. The predicted fracture intrudes 60 ft into the lower layer and 362 ft into the upper layer.

The fracture length that remains propped at closure is 915 ft, approximately 50% of the total half-length (1731 ft). The effective width of the propped fracture is 0.223 in in the vicinity of the perforated interval, tapering to a closed fracture with no proppant 915 ft from the borehole (Figure 2.65). The large dark blue area (Figure 2.65) indicates that the region was fractured during injection, but was not filled with proppant. At fracture closure, this area is held open only by asperities on the fracture wall.

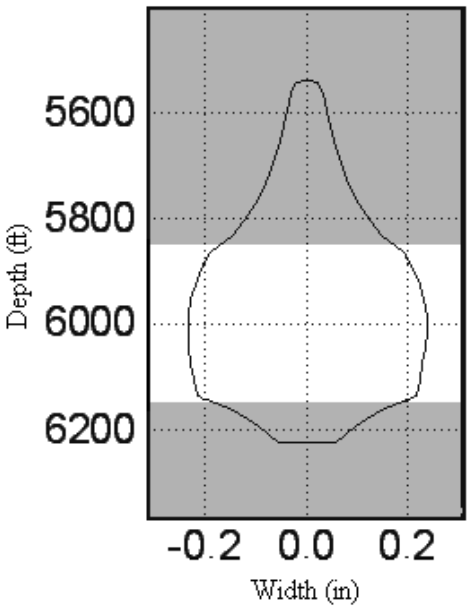

Figure 2.64 Cross section of fracture width at the well bore for the 1500 ft fracture case. The grey area represents the shale layers.

The average conductivity for the "1500 ft" fracture is 405 md-ft, but the distribution of conductivity is variable throughout the fracture (Figure 2.66). There is a region of higher conductivity around the initiation area where the conductivity is greater than 1700 md-ft out to an approximate horizontal distance of 130 ft from the well bore. Beyond 130 ft the fracture conductivity decreases away from the well bore and is less than 213 md-ft in the dark blue region (Figure 2.66). The region of the fracture where conductivity is greater than 213 md-ft is delta-shaped, penetrating into the upper and lower adjacent formations.

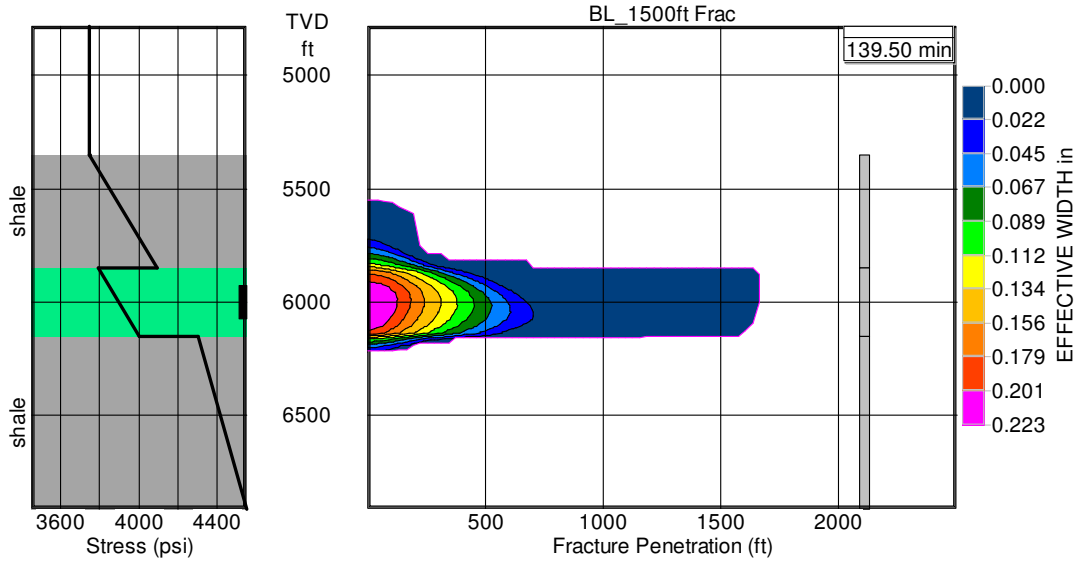

Figure 2.65 Effective width for a proposed 1500 ft fracture in a 300 ft thick limestone formation.

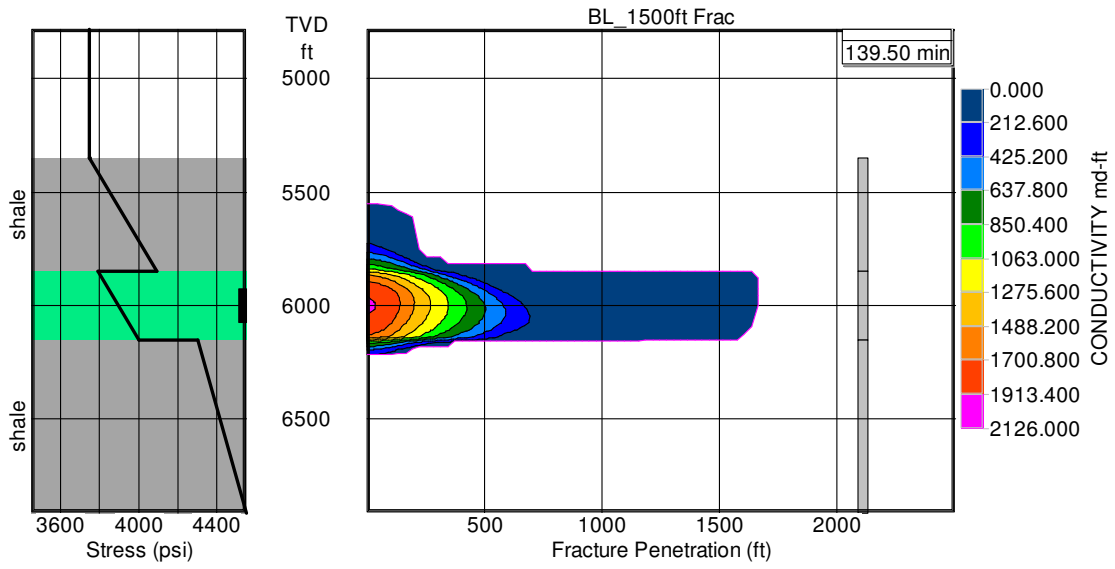

Figure 2.66 Conductivity for a 1500 ft fracture in a 300 ft limestone formation

30 ft Fracture

A simulation was set up to create a fracture where the ideal half- length was one fifth the thickness of the formation. For this case, all of the variables were the same as the baseline case with the exception of a pumping schedule intended to create at least a 30 ft fracture. This situation resulted in a fracture that penetrated 47 ft into the limestone formation and had a vertical growth of 184 ft at the well bore (Figure 2.67). The fracture was contained within the limestone formation with 56 ft of clearance between the

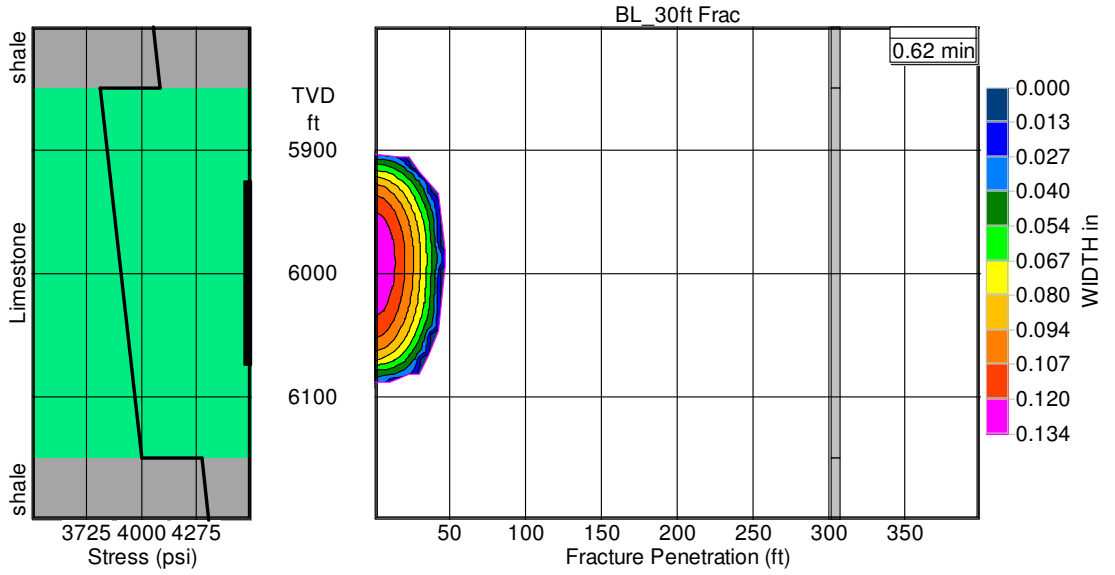

Figure 2.67 Contour plot of pressurized width (in) for a proposed 30 ft fracture in a 300 ft thick limestone formation.

overlying formation and 59 ft of clearance between the underlying formation. The pressurized fracture width is 0.134 in near the well bore and decreases rapidly to fracture closure at 47 ft (Figure 2.67).

The cross section of the fracture is roughly oval shaped at the bore hole (Figure 2.68). The fracture reaches a maximum upward growth at a depth of 5909 ft and the maximum downward growth is reached a 6091 ft. The maximum pressurized width is 0.14 in at a depth of 6000 ft (Figure 2.68).

The fracture length that remains propped at closure after injection pressure decreases is 23 ft, approximately 50% of the penetrated half length (47 ft). The effective width of the propped fracture is 0.047 in near the center of the perforated interval, tapering to a closed fracture with no proppant 23 ft from the borehole (Figure 2.69).

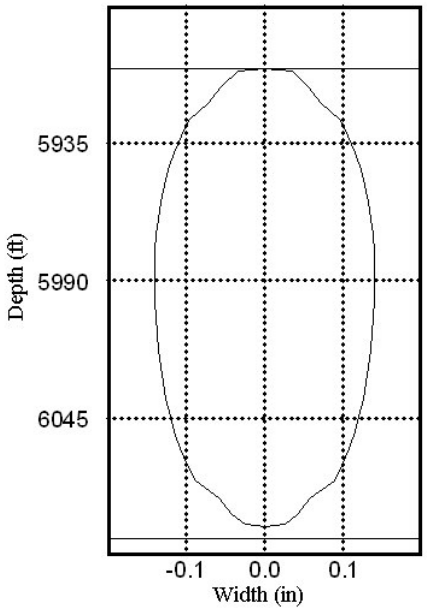

Figure 2.68 Cross section of fracture width for 30 ft target fracture.

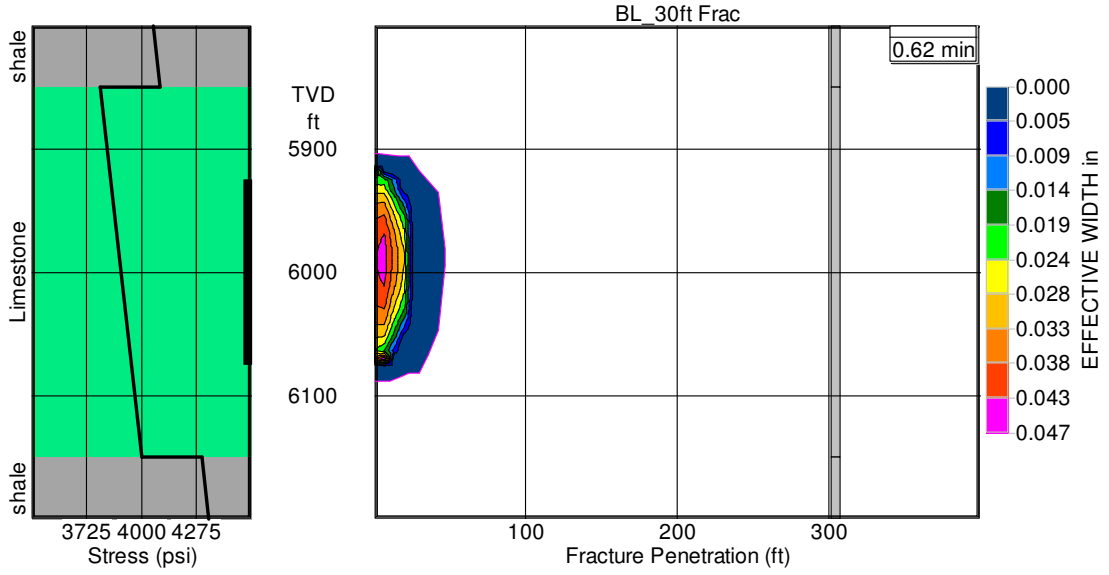

Figure 2.69 Effective width (in) for a proposed 30 ft fracture in a 300 ft limestone formation.

The average conductivity for the proposed 30 ft fracture is 143 md-ft. There is a small region of relatively high conductivity (408 md-ft) near the center of the perforated interval, but it decreases rapidly and the conductivity is less than 40 md-ft only 23 ft from the well bore (Figure 2.70). Overall, the fracture conductivity for the 30 ft fracture case is less than the baseline case (Figure 3.4).

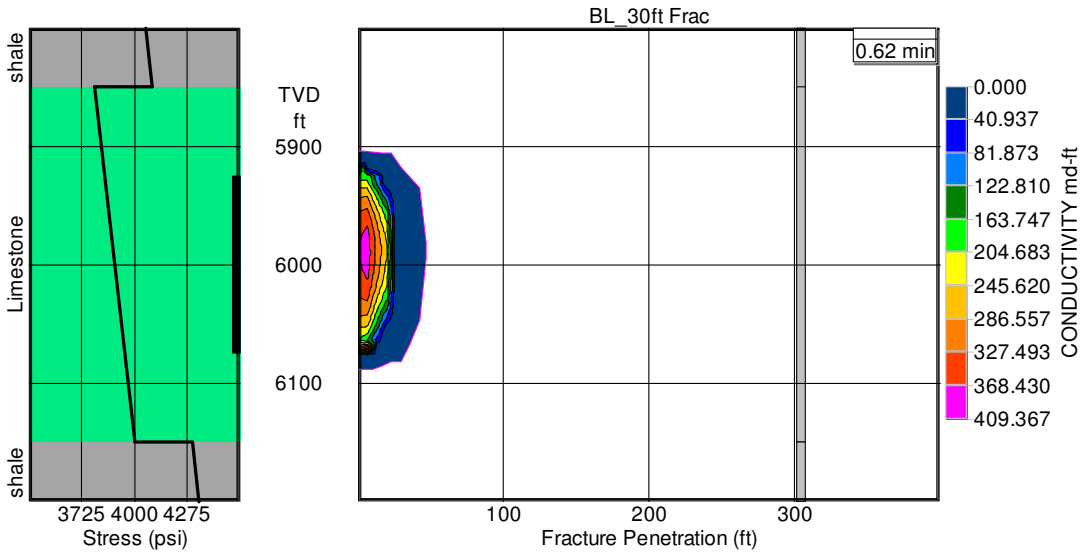

Figure 2.70 Conductivity for a proposed 30 ft fracture in a 300 ft limestone formation

Adjacent Layer 1 Foot Thick

The simulation of a fracture in a 300-ft-thick limestone formation bounded by shale layers 1 ft thick results in a fracture with a half-length of 384 ft with a propped length of 255 ft and an average conductivity of 120 md-ft (Figure 2.71). The maximum fracture height at the wellbore is 594 ft and the fracture completely breaches the shale layer. There is an increase in the conductivity around the shale layers (Figure 2.71).

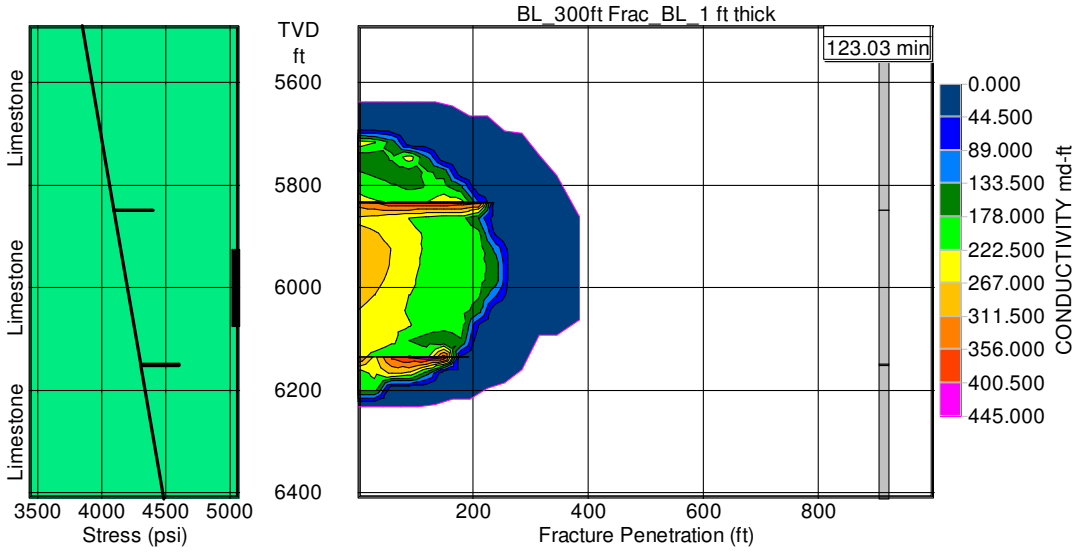

Figure 2.71 Conductivity for fracture simulated in 300 ft thick limestone formation with 1 ft thick adjacent layer

The cross section of fracture width for a fracture in a 300 ft thick limestone formation bounded by shale layers 1 ft thick is roughly oval shaped with indentations in the oval occurring near the shale layers (Figure 2.72). The fracture extends about 122 ft above the upper shale layer and approximately 36 ft below the lower shale layer. The maximum pressurized width is 0.28 in at a depth of 6000 ft (Figure 2.72).

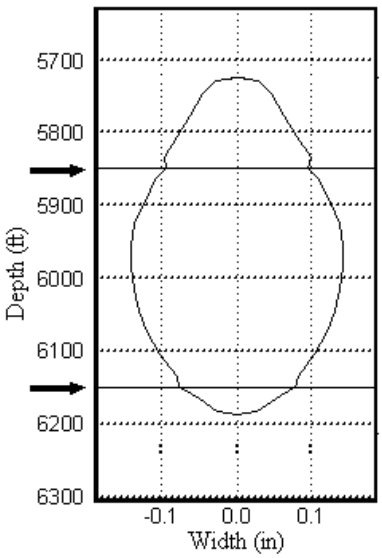

Figure 2.72 Cross section of fracture width for a fracture simulated in a 300 ft thick limestone formation with a 1 ft thick adjacent layer. Lines indicated by arrows represent the shale layer.

Compared to a simulation where the limestone thickness is 1500 ft and there is clearance between the fracture and the adjacent layer (Figure 2.54), the effect of the 1 ft shale layer is more apparent. The conductivity contours in the 1500 ft formation are relatively smooth curves that radiate out from the perforated interval with a gradual, uniform decrease in fracture conductivity (Figure 2.54). For the simulation of a fracture in a 300 ft limestone formation with a 1 ft thick adjacent layer, the conductivity distribution is inconsistent with regions of higher conductivity in the vicinity of the shale layers (Figure 2.71).

Adjacent Layer 10 Feet Thick

The simulation of a fracture in a 300-ft-thick limestone formation bounded by shale layers 10 ft thick results in a fracture with a half-length of 379 ft with a propped length of 255 ft and an average conductivity of 115 md-ft (Figure 2.73). The maximum fracture height at the wellbore is 631 ft and the fracture completely breaches the shale layer. There is a region of higher conductivity near the perforated interval that extends into a lobe that is bounded by the upper shale layer (Figure 2.73).

The cross section of fracture width in a 300 ft thick limestone formation bounded by shale layers 10 ft thick is roughly oval shaped within the limestone formation. When the fracture encounters the upper shale layer, the fracture width is reduced 20% from 0.2 to 0.16 in. Above the shale layer the fracture width increases to 0.18 in and closes in an arch shape that extends 110 ft into the layer above the shale (Figure 2.74). When the fracture crosses the lower shale layer, the change in fracture width is less than across the upper layer. However, the width continues to decrease below the shale layer with the fracture penetrating 64 ft into the formation underlying the shale layer. The maximum pressurized width is 0.29 in at a depth of 6000 ft (Figure 2.74).

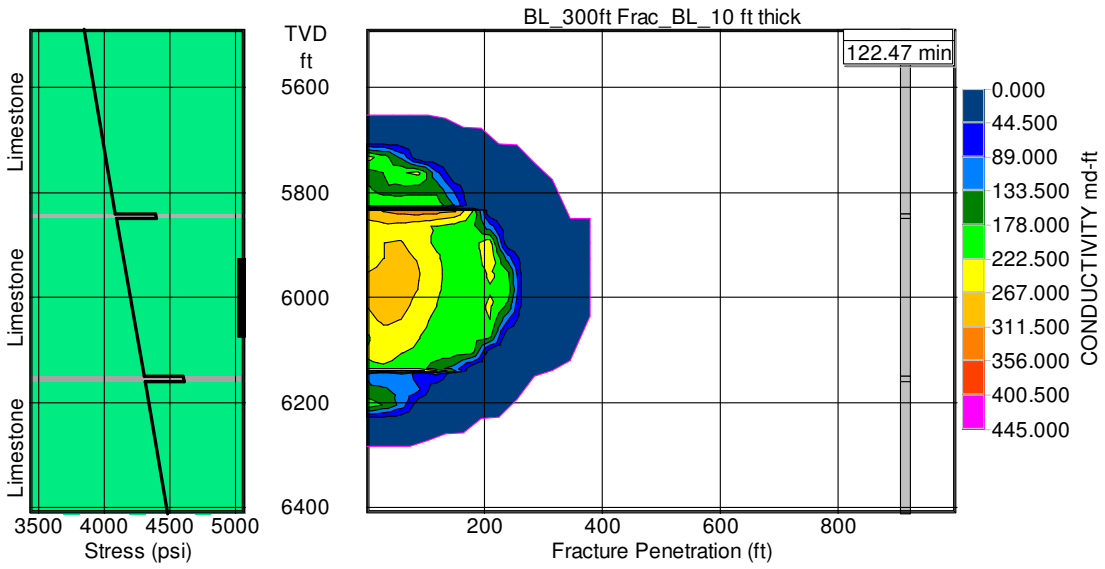

Figure 2.73 Conductivity for fracture simulated in 300 ft thick limestone formation with 10 ft thick adjacent layer

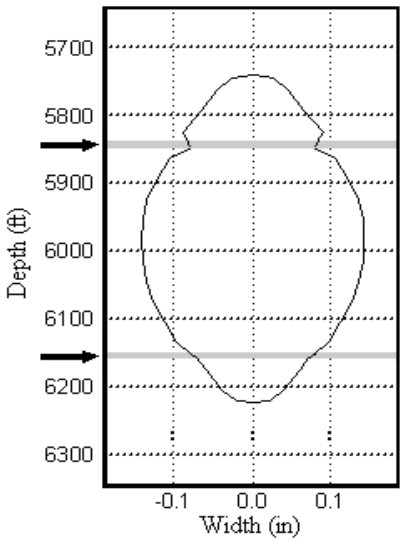

Figure 2.74 Cross section of fracture width for a fracture simulated in a 300 ft thick limestone formation with a 10 ft thick adjacent layer. Grey lines indicated by arrows represent the shale layer.

Adjacent Layer 25 Feet Thick

The simulation of a fracture in a 300 ft thick limestone formation bounded by shale layers 25 ft thick results in a fracture with a half-length of 427 ft with a propped length of 285 ft and an average conductivity of 118 md-ft (Figure 2.75). The maximum fracture height at the wellbore is 578 ft and the fracture completely breaches the shale layer. There is a region of higher conductivity near the perforated interval that extends into a lobe that is bounded by the upper shale layer, as well as an area of increased conductivity near the tip of the propped length (Figure 2.75).

The cross section of fracture width for a fracture in a 300 ft thick limestone formation bounded by shale layers 25 ft thick is roughly oval shaped within the limestone formation. When the fracture interacts with the upper shale layer, the fracture width is reduced by 50% from 0.2 to 0.10 in.

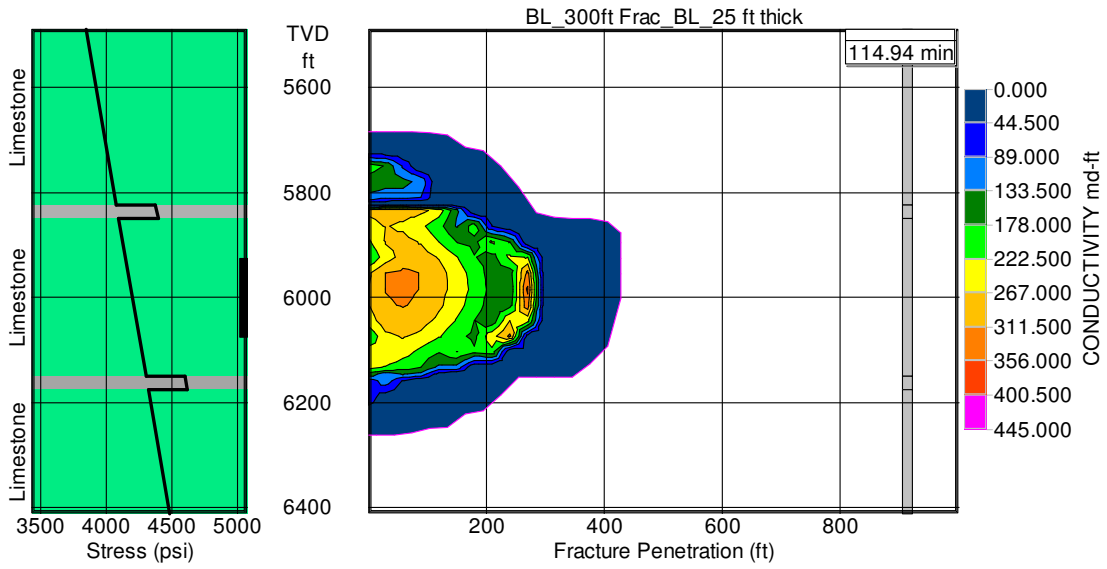

Figure 2.75 Conductivity for fracture simulated in 300 ft thick limestone formation with 25 ft thick shale adjacent layers

Above the shale layer the fracture width increases to 0.14 in and closes in an arch shaped that extends 66 ft into the layer above the shale (Figure 2.76). When the fracture crosses the lower shale layer, the fracture width is reduced from 0.20 to 0.09 in and continues to decrease below the shale layer. The fracture propagates 42 ft into the formation that is below the shale layer. The maximum pressurized width is 0.30 in at a depth of 6000 ft (Figure 2.76).

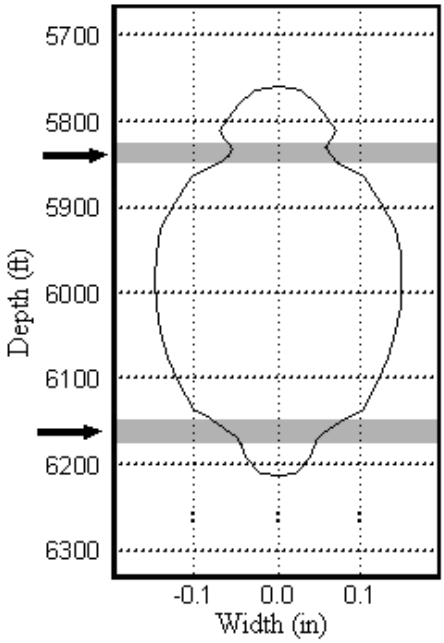

Figure 2.76 Cross section of fracture width for a fracture simulated in a 300 ft thick limestone formation with a 25 ft thick adjacent layer. Grey lines indicated by arrows represent the shale layer.

Adjacent Layer 50 Feet Thick

The simulation of a fracture in a 300 ft thick limestone formation bounded by shale layers 50 ft thick results in a fracture with a half-length of 486 ft with a propped length of 354 ft and an average conductivity of 149 md-ft (Figure 2.77). The maximum

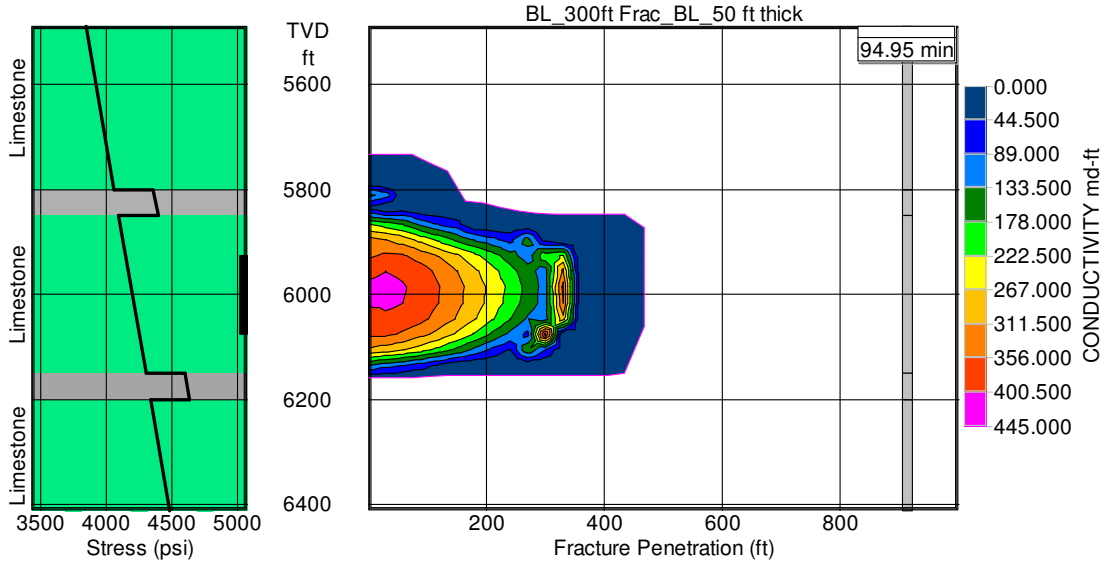

Figure 2.77 Conductivity for fracture simulated in 300 ft thick limestone formation with 50 ft thick shale layers

fracture height at the wellbore is 427 ft and the fracture completely breaches the shale layer. The conductivity distribution is relatively uniform with a region of higher conductivity near the perforated interval that decreases away from the well. There is also a region of increased conductivity near the tip of the propped length (Figure 2.77).

The cross section of fracture width for a fracture in a 300 ft thick limestone formation bounded by shale layers 50 ft thick is roughly oval shaped within the limestone formation (Figure 2.78). As the fracture approaches the lower shale layer, the curve flattens, penetrating 7 ft into the lower layer. When the fracture interacts with the upper shale layer, the fracture width reduces from 0.2 in

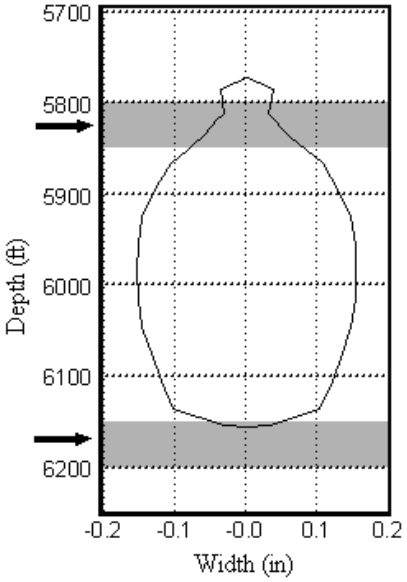

Figure 2.78 Cross section of fracture width for a fracture simulated in a 300 ft thick limestone formation with a 50 ft thick adjacent layer. Grey lines indicated by arrows represent the shale layer.

to 0.06 in 50 ft above the contact between the shale and the limestone. Above the shale layer the fracture width increases to 0.08 in and closes at a peak 30 ft into the layer above the shale (Figure 2.78). The maximum pressurized width is 0.31 in at a depth of 6000 ft.

Adjacent Layer 75 Feet Thick

The simulation of a fracture in a 300-ft-thick limestone formation bounded by shale layers 75 ft thick results in a fracture with a half-length of 482 ft, a propped length of 345 ft, and an average conductivity of 149 md-ft (Figure 2.79). The maximum fracture height at the wellbore is 344 ft, and the fracture is contained within the shale layer. The conductivity distribution is relatively uniform with a region of higher conductivity near the perforated interval that decreases away from the well. There is also an area of increased conductivity near the tip of the propped length (Figure 2.79).

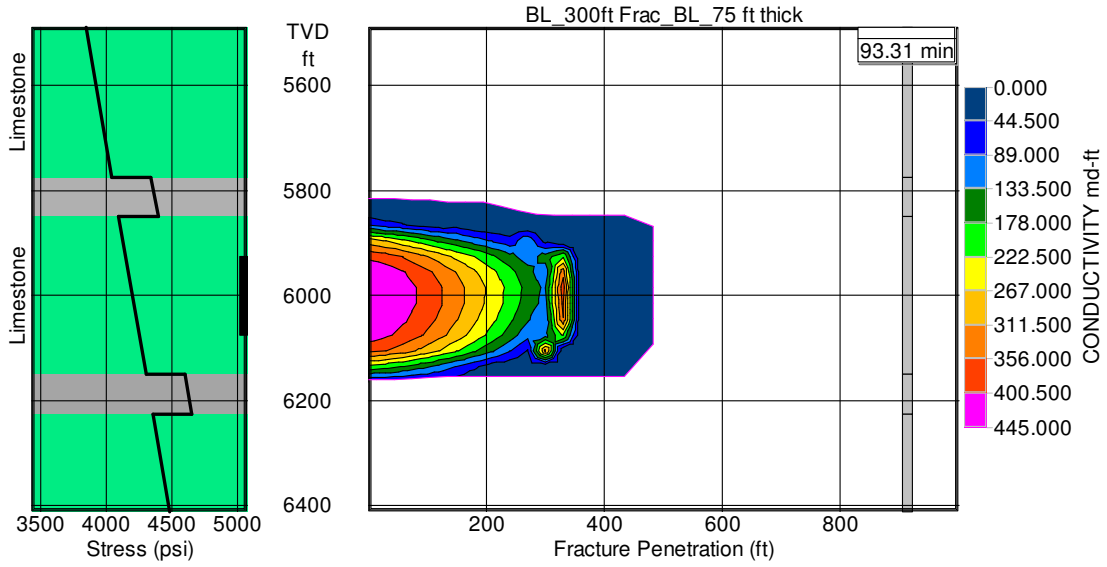

Figure 2.79 Conductivity for fracture simulated in 300 ft thick limestone formation with 50 ft thick shale layers

The cross section of fracture width for a fracture in a 300 ft thick limestone formation bounded by shale layers 75 ft thick is roughly oval shaped within the limestone formation (Figure 2.80). As the fracture approaches the lower shale layer, the curve becomes flatter, penetrating 11 ft into the lower layer. As the fracture interacts with the top layer, the curve of the fracture gets tighter and terminates approximately 42 ft above the limestone shale interface. This leaves 33 ft of clearance between the upper fracture terminus and the layer above the shale. The maximum pressurized width is 0.31 in at a depth of 6000 ft (Figure 2.80).

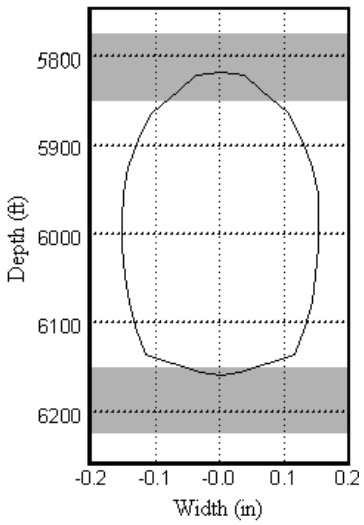

Figure 2.80 Cross section of fracture width for a fracture simulated in a 300 ft thick limestone formation with a 75 ft thick adjacent layers. Grey boxes represent the shale layers.

Adjacent Layer 100 Feet Thick

The simulation of a fracture in a 300 ft thick limestone formation bounded by shale layers 100 ft thick results in a fracture with a half-length of 469 ft with a propped length of 345 ft and an average conductivity of 156 md-ft (Figure 2.81). The maximum fracture height at the wellbore is 352 ft and the fracture is contained within the shale layer. The conductivity distribution is relatively uniform with a circular region of higher conductivity near the perforated interval that decreases away from the well. There is also a lobe of increased conductivity near the tip of the propped length (Figure 2.81).

The cross section of fracture width for a fracture in a 300 ft thick limestone formation bounded by shale layers 100 ft thick is roughly egg shaped within the limestone formation (Figure 2.82). As the fracture approaches the lower shale layer, the curve becomes flatter, penetrating only 12 ft into the lower layer. As the fracture interacts with the top layer, the curve of the fracture gets tighter and terminates approximately 18 ft above the limestone shale interface. This leaves 82 ft of clearance between the upper fracture terminus and the layer above the shale. The maximum pressurized width is 0.31 in at a depth of 6000 ft (Figure 2.82).

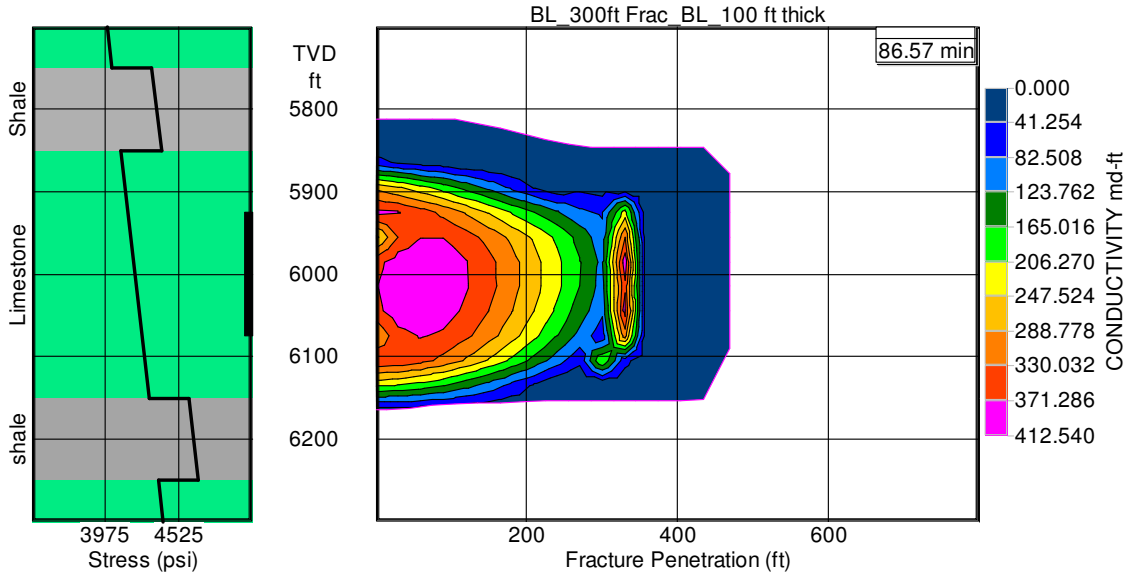

Figure 2.81 Contour plot of conductivity for fracture simulated in 300 ft thick limestone formation with 100 ft thick shale layers

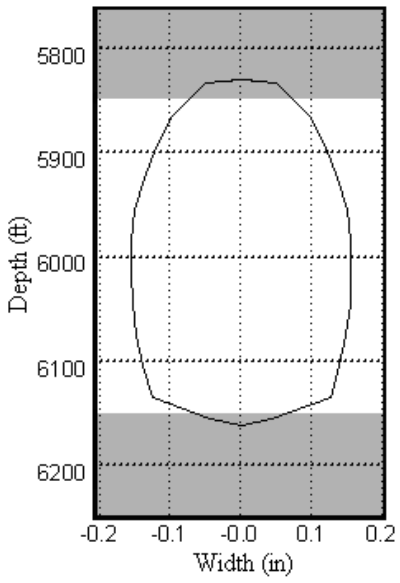

Figure 2.82 Cross section of fracture width for a fracture simulated in a 300 ft thick limestone formation with a 100 ft thick adjacent layers. Grey boxes represent the shale layers.

Adjacent Layer 150 Feet Thick

The simulation of a fracture in a 300 ft thick limestone formation bounded by shale layers 150 ft thick results in a fracture with a half-length of 475 ft with a propped length of 345 ft and an average conductivity of 149md-ft (Figure 2.83). The maximum fracture height at the wellbore is 361 ft and the fracture is contained within the shale layer. The conductivity distribution is relatively uniform with a circular region of higher conductivity near the perforated interval that decreases away from the well. There is also a lobe of increased conductivity near the tip of the propped length (Figure 2.83).

The cross section of fracture width for a fracture in a 300 ft thick limestone formation bounded by shale layers 150 ft thick is roughly egg shaped within the limestone formation (Figure 2.84). As the fracture approaches the lower shale layer, the curve becomes flatter, intruding only 13 ft into the lower layer. As the fracture interacts with the top layer, the curve of the fracture gets tighter and terminates approximately 19 ft above the limestone-shale interface. This leaves 131 ft of clearance between the upper fracture terminus and the layer above the shale. The maximum pressurized width is 0.31 in at a depth of 6000 ft (Figure 2.84).

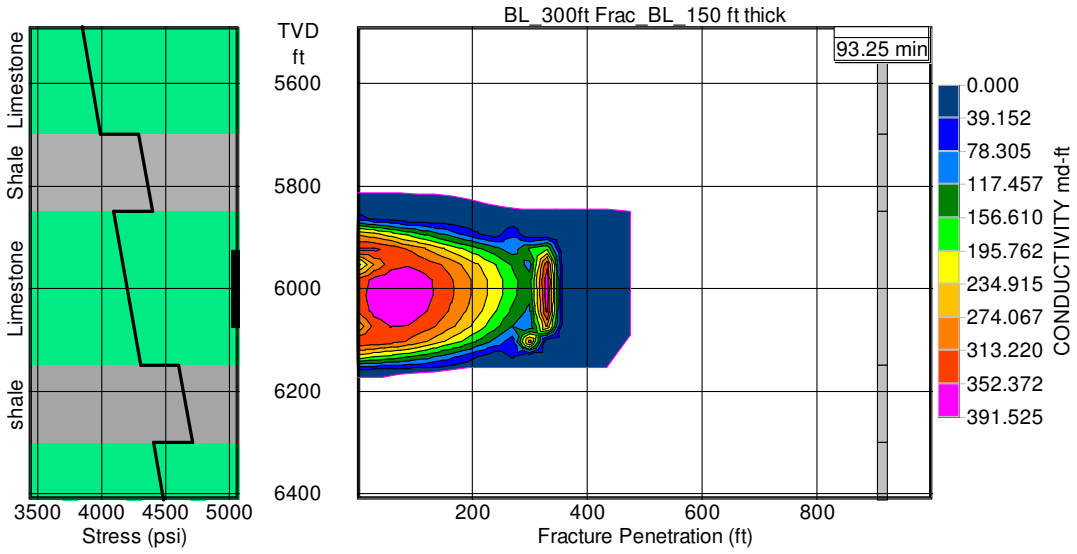

Figure 2.83 Conductivity for fracture simulated in 300 ft thick limestone formation with 150 ft thick shale layers

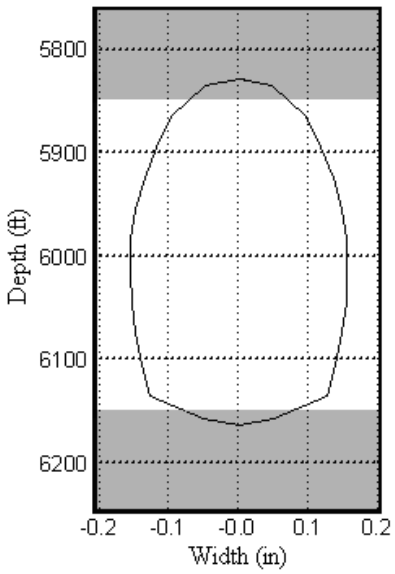

Figure 2.84 Cross section of fracture width for a fracture simulated in a 300 ft thick limestone formation with a 150 ft thick adjacent layer. Grey boxes represent the shale layer.

Adjacent Layer Thickness

Variations in the thickness of the adjacent layers (1 ft, 10 ft, 25 ft, 50 ft, 75 ft, 100 ft, 150 ft and 200 ft) were simulated to predict the effects of adjacent formation thickness on fracture height. As the thickness of the adjacent layers increases, the total fracture height decreases (Figure 2.85). There is a steep decrease in fracture height as the adjacent layer thickness increases from 1 ft to 75 ft and there is less variation in the total fracture height at adjacent formation thicknesses greater than 75 ft (Figure 2.85).

Intrusion into the upper layers as a result of variations in adjacent layer thickness has a similar trend. There is a steep decrease in vertical growth up to a 75-ft-thick adjacent layer with less variation when the adjacent layer thickness is greater than 75 ft (Figure 2.86). The fracture completely breaches the adjacent layer and intrudes into the formation above the adjacent layer for thickness less than 75 ft. When the adjacent layer

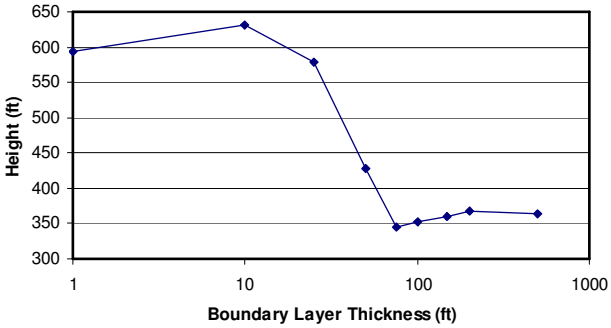

Figure 2.85 Total vertical fracture height at well bore for variations in adjacent layer thickness

thickness is 75 ft or greater, there is clearance between the fracture and the limestone above the adjacent layer that increases with increasing thickness (Figure 2.87).

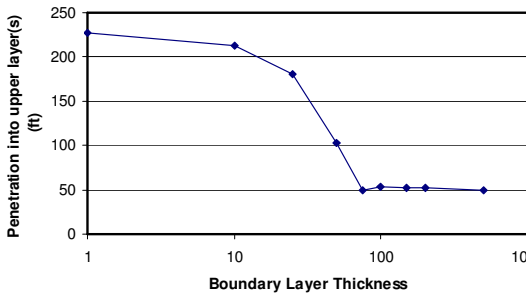

Figure 2.86 Fracture intrusion into upper formations as function of adjacent layer thickness

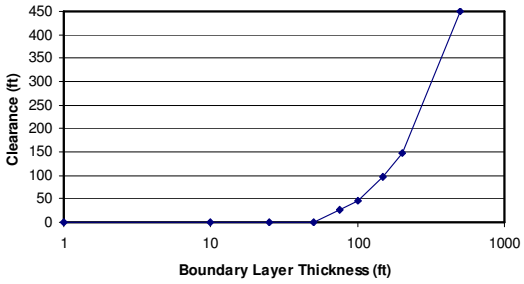

Figure 2.87 Clearance between material overlying the upper layer and upper fracture tip as a function of adjacent layer thickness

Summary of Fracture Modeling and Conclusions

Simulations of hydraulic fractures in limestone were conducted using a range of parameters representing expected conditions at a site for the creation of a gas storage facility by acid dissolution. Results indicate the typical characteristics for a baseline case, as well as ranges of fracture characteristics based on the expected parameters (Table 2.19). The simulations demonstrate how hydraulic fracturing can increase conductivity in a formation, and what factors influence fracture characteristics. Inherent properties such as the stratigraphy and in-situ stress for the rock layers have a significant impact on the resulting fracture characteristics. Whereas other factors such as perforated interval,

Table 2.19 Range of fracture characteristics for all simulations

	Low	Baseline	High
Half-length (ft)	43 ft	291 ft	485 ft
Propped length (ft)	28 ft	200 ft	353 ft
Height (ft)	175 ft	363 ft	790 ft
Avg. Width (in)	0.05 in	0.19 in	1.74 in
Avg. Conductivity (md-ft)	115 md-ft	396 md-ft	8166 md-ft

pumping schedule, pumping rate, proppant and fracturing fluid can be modified to influence the predicted fracture geometry. The data presented in this report demonstrate the influence of different parameters on fracture characteristics and estimate fracture characteristics expected in typical limestone formations. Prior to any fracturing job, detailed information about the physical characteristics and stratigraphy of the site should be collected and simulations should be run in order to predict the ideal pumping schedule and slurry combination that would produce a fracture with the optimal geometry and conductivity.

Development of a Numerical Model to Predict Formation of Storage Volume during the Dissolution Process (Task 8)

by Ron Falta and David Bruce

Modeling the Acid Dissolution of Carbonate Rocks

In order to accurately model the limestone dissolution process, it is essential that the thermodynamic parameters that determine phase equilibria and reaction equilibria be calculated accurately. After considering several options, the TOUGHREACT simulation code was selected to model the acid dissolution of carbonate rock. This code uses fundamental thermodynamic, kinetic, and transport equations in conjunction with a database of parameters to predict reaction and phase equilibria, rates of rock dissolution, and the composition of outlet streams exiting the cavern. Because TOUGHREACT was not specifically written to model the acid dissolution process, there are several parameter sets that needed to be customized so that more accurate simulation results could be obtained. The most important thermodynamic parameters in these calculations are those used to calculate (1) the density of the supercritical CO_2 phase that will exist above the aqueous acid/salt solution in the cavern during acid dissolution and (2) the vapor-liquid phase equilibria for CO_2, where the liquid phase is an aqueous solution rich in calcium chloride.

Calculation of CO_2 Pure Component Properties

Extensive studies of CO_2 properties (e.g., compressibility, heat capacity, fugacity, etc.) have been previously conducted and correlations developed to describe these properties; however, these correlations were commonly parameterized for a broader range of conditions than will likely be encountered in the dissolution process. Hence, the accuracy of these correlations could be improved if only the limited range of conditions experienced during acid dissolution were considered.

Upon examining the data used in the TOUGHREACT simulation program it was discovered that many of the correlations used for CO_2 compressibility, fugacity, and aqueous solubility were not optimal for studying the acid dissolution process. Thus, original experimental data for CO_2 was reparameterized so as to optimally describe the physical properties of CO_2 during acid dissolution of carbonate rock formations located 4,000 to 10,000 feet deep. Of particular importance were the compressibility of CO_2 and the solubility of CO_2 in the calcium salt rich dissolution media.

TOUGHREACT use the correlations below to describe the compressibility factor (Z) and fugacity coefficient (ϕ) of CO_2,

$$Z_{CO_2} = \frac{PV}{RT} = 1 + P\left(\frac{a}{T^2} + \frac{b}{T} + c\right) + P^2\left(\frac{d}{T^2} + \frac{e}{T} + f\right) \tag{3.1}$$

$$\ln\phi = \mathrm{P}\left(\frac{\mathrm{a}}{\mathrm{T}^2} + \frac{\mathrm{b}}{\mathrm{T}} + \mathrm{c}\right) + \frac{\mathrm{P}^2}{2}\left(\frac{\mathrm{d}}{\mathrm{T}^2} + \frac{\mathrm{e}}{\mathrm{T}} + \mathrm{f}\right) \tag{3.2}$$

where T is temperature (°C), P is pressure (bar), and the coefficients a through f are determined by a non-linear least squares curve fit of experimental P-V-T data. This equation was derived by Spycher and Reed (1988) and ignores all virial equation coefficients after the third term; thus, it is incapable of accurately describing the behavior of CO_2 near the critical point. The parameters for CO_2 compressibility in TOUGHREACT are shown in Table 3.1 for the temperature range of 50-350 °C and pressure range of 10-500 bars and were originally calculated by Spycher and Reed using the experimental data assembled by Angus et al. (1976). These parameters were calculated from a fit of data that included a relatively broad range of subcritical and supercritical conditions for CO_2. The error associated with this initial set of CO_2 compressibility parameters as a function of system temperature and pressure is shown in Figure 3.1. The percentage error associated with the phase equilibria calculations required to describe the entire acid dissolution process are in some cases as high as 30%. It is also important to note that the conditions likely to be observed during the course of the acid dissolution process include temperatures from 290 to 370 °C and pressures from 100 to 400 bars. Since the P-T conditions for acid dissolution are less broad than those originally used to parameterize Equation 3.1 for CO_2 compressibility, we sought to reparameterize this equation using a narrower set of the experimental data assembled by Angus et al. The non-linear least squares regression of P-V-T data for CO_2 was carried out using Dataplot, a robust solver package developed by researchers at NIST. The resulting parameters from this regression are shown in Table 1 alongside the previous results of Spycher and Reed. It was decided that the simulations be broken down into two types: (1) type I would only examine the phase and reaction behavior for CO_2 at depth in the cavern when CO_2 was supercritical and (2) type II would examine the phase behavior of CO_2 as it exited the well (going from supercritical to subcritical). Though the original set of parameters by Spycher and Reed appear to perform well under the conditions required for the acid dissolution, a closer examination of standard deviations between predicted and calculated values for Z indicated that the error with these intial parameters were on average 9.3%, while the optimized parameter set developed at Clemson for studying the dissolution process had an average error of only 3.2%. Type II simulations do not involve any reactions between carbonate rock and acid; hence, these simulations were conducted using Aspen Plus process simulation software and an equation of state model with sufficient number of virial coefficient terms so as to accurately describe the flow behavior of material (especially CO_2) exiting the underground cavern. This information will be included in the final report for Year 3 of this project as statistical analysis of these results has yet to be performed.

Table 3.1. Gas compressibility and fugacity coefficient parameters for CO_2.

Gas	CO_2 (TOUGHREACT)	CO_2 (Clemson)
Temperatures (°C)	50 - 350	290 - 370
Pressures (bars)	10 - 500	100 - 400
A	-1430.87	-254.801
B	3.598	-10.852
C	-2.27×10^{-3}	0.0300
D	3.48	31.4858
E	-0.0104	-0.149125
F	8.46E-06	1.75E-04

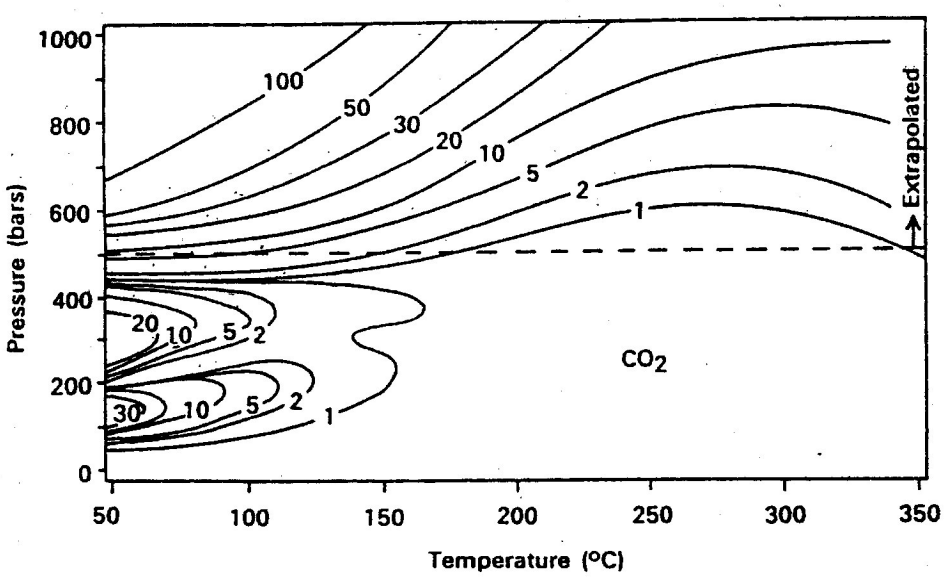

Figure 3.1. Deviation, in percent, between experimental data (Angus etal., 1976) and calculated values (Spycher and Reed, 1988) of CO_2 compressibility (Z).

The remainder of our report chapter on Task 8 is organized into three sections, a section dealing with three-dimensional patterns of rock dissolution, where in-situ CO_2 production is neglected; a section that describes one-dimensional simulations of acid-carbonate dissolution in which the full geochemical reactions are included; and a section that investigates the long-term storage of natural gas in solution mined caverns.

Three-Dimensional Simulation of Cavern Formation Neglecting CO_2 Production

Salt solution mining is an old process that started in the 1800's, and the use of solution mined salt caverns for hydrocarbon storage started in the 1940's. Typical dimensions of salt caverns used for strategic petroleum reserve storage are 2000 ft high and a 300 ft diameter. Salt caverns used by the private sector for hydrocarbon storage are generally smaller than the strategic petroleum reserve caverns.

From a chemical standpoint the process of salt cavern creation by solution mining is different from acid cavern dissolution in carbonates, primarily due to the production of CO_2 during the carbonate reaction. However, there are many similarities including the fact that both are essentially mass transfer limited rock dissolution processes in which there are very strong buoyancy gradients. Because salt dissolution is not reaction rate limited, the mass transfer of fresh water to the fluid-salt interface controls the rate of dissolution (Saberian and Podio 1977). Reaction rates between carbonate and HCl are also fast, therefore the reaction is also often mass transfer limited and the rate at which acid is delivered to the reaction surfaces has a dominating influence on the rate of carbonate dissolution (Williams et al. 1979). Numerical simulations of the carbonate dissolution process therefore must be able to account for the rate of acid and product mass transfer to and from the rock-solution boundary. Consideration of local reaction kinetics is probably of secondary importance.

Salt (NaCl) has a very high solubility in water, 311.3 g/l (CRC, 1987). As fresh water with a density of 1000 kg/m^3 becomes saturated with salt, its density rises to 1199 kg/m^3, an increase of 20%. The resulting buoyancy forces thus play a central role in the fluid flow as they will in the acid dissolution of limestone. Considering the solubility of salt in fresh water, and rock salt density of 2170 kg/m^3, the equivalent dissolving power of fresh water is 0.168, which is remarkably close to the volumetric dissolving power of 30% HCl on pure limestone (.175). With important exception of CO_2 generation, the processes of salt solution mining with fresh water and HCl dissolution of limestone are very similar.

In last years report (Falta et al., 2004), we showed how a modified version of the DOE T2VOC simulator was capable of accurately modeling field salt cavern formation using fresh water injection. In this section, we use the modified T2VOC code to simulate cavern dissolution for several 3-dimensional geometries. While these simulations do not consider the production of CO_2, they provide basic insights into solution mining strategies are most promising for developing the natural gas storage caverns in carbonates.

T2VOC considers the three-phase flow of gas, water, and a nonaqueous phase liquid (NAPL) in three-dimensional porous or fractured media. The model is fully compositional, so that the NAPL phase can dissolve into the aqueous phase with associated aqueous phase density effects (calculated assuming volume additivity). Since T2VOC does not directly consider rock dissolution or precipitation, the NAPL phase in the code was given the properties of rock salt. Thus the "rock" component in T2VOC had a density of 2170 kg/m^3, zero relative permeability, infinite viscosity, and an aqueous solubility of 311 g/l.

The porosity of the model domain was then set to one, and is not used as a variable in this case. With this formulation, the water phase saturation, S_w is used to

model the dynamic rock porosity, and the NAPL phase, with a volumetric saturation of S_R, is used to model the fraction of rock. Therefore, in this model the "porosity" is

$$\phi_R = 1 - S_R = S_w \tag{3.3}$$

and when S_R=0, the rock has completely dissolved away.

Multiphase flow formulations model phase permeabilities as the product of the rock intrinsic permeability with a phase saturation dependent relative permeability. For the aqueous (water) phase,

$$k_w = k_{rock} k_{rw} \tag{3.4}$$

where k_{rock} is the rock intrinsic permeability, and k_{rw} is the relative permeability of the aqueous phase. In the present work, the water saturation is an analogue for porosity, so when S_w=1, there is no rock present, and k_{rw}=1. The T2VOC model assumes darcian flow, so the "permeability" of the open sections of a cavern, k_{rock}, was set to a very high value, 10^{-6} or 10^{-5} m^2 (one to ten million darcys). While this neglects possibly important turbulent flow effects, it allows for fluids to freely flow in open parts of the cavern in response to buoyancy and pressure effects. The change in rock intrinsic permeability as a function of porosity was modeled using the aqueous phase relative permeability function:

$$k_{rw} = S_w^3 \tag{3.5}$$

so the effective intrinsic permeability of the dissolving rock depends on the cube of the rock porosity. Other porosity-permeability models could be used (see, for example, Pruess et al., 1999), but as will be shown, this cubic model is theoretically correct for a dissolving fracture embedded in an element.

Using Equations 3.4 and 3.5, the rock permeability can vary from zero to the assumed effective cavern permeability (k_{rock}). In the current simulations, the initial intact rock permeability was assumed to be 10^{-17} or 10^{-16} m^2, or 10-100 microdarcy. This is obtained in the model using Equation 3.5 by initializing the water saturation (S_w) at a value of 0.0002154 to get a permeability reduction of 10^{-11}. Therefore, the intrinsic permeability in each dissolving rock gridblock in this model will vary by eleven orders of magnitude during a simulation of cavern formation. This rapid change causes the problem to be extremely nonlinear, but the multiphase numerical treatment in T2VOC and similar multiphase codes is designed to specifically to deal with this numerical issue as long as all terms are fully coupled in the Jacobian Matrix during the Newton Raphson iteration process. For a non-zero initial rock porosity, Equation 3.5 could easily be modified by using a scaled saturation with k_{rw} equal to zero at a nonzero S_w value.

The modified version of T2VOC used here includes aqueous diffusion. Mathematically, the diffusive flux is calculated as the product of an effective diffusion coefficient with the concentration gradient between two adjacent finite difference cells. This is mathematically equivalent to a first order mass transfer expression driven by the concentration difference in the adjacent cells. Therefore, the aqueous diffusion in T2VOC was used to model a first order mass transfer reaction between open parts of the

cavern, and the cavern walls (see, also, Williams et al., 1979). Following Falta (2000), the mass transfer reaction between the open cavern and the rock is modeled in adjacent gridblocks by:

$$Q_{C-R} = \frac{D' A_{C-R}}{d_{C-R}} (C_{w,R} - C_{w,C}) \tag{3.6}$$

where $Q_{C\text{-}R}$ is the rate of mass transfer of rock into solution at the cavern-rock interface ($kg/(s*m^3)$), $A_{C\text{-}R}$ is the interfacial area of the cavern-rock interface normalized to the cavern-rock gridblock volume, $d_{C\text{-}R}$ is the average distance from center of the cavern gridblock to the center of the rock gridblock, and D' is a diffusion-like fitting parameter. The concentration gradient between the open cavern element and the rock element, ($C_{w,R}$-$C_{w,C}$), drives this first order reaction. For simple rock salt dissolution, the mass transfer rate, and the rate of rock dissolution are maximized when the salt concentration in the cavern gridblock is zero. The rate of mass transfer is zero when the salt concentration in the cavern gridblock is equal to the concentration in local equilibrium with the rock salt. As the rock dissolves away, the location of the cavern-rock interface changes with time, and this is automatically accounted for with this approach. Based on the field scale salt cavern simulations we reported last year, D' was set to a value of 10^{-4} m^2/s.

One of the most important operational issues to be addressed in this study is the basic configuration of the rock dissolution scheme. Our original proposal called for hydraulic fracturing, followed by acid dissolution. However, salt caverns are commonly formed without fracturing, using open boreholes. A series of three-dimensional simulations were used to investigate three different dissolution configurations: a) injection into an open borehole with production from that same borehole and no fracture; b) injection into an open borehole with production from that same borehole, with an open fracture; and c) injection into an open borehole connected by a fracture to an adjacent borehole from which the fluids are produced.

The three-dimensional grid consists of 2520 gridblocks, and it is aligned parallel to a fracture face (Figure 3.2). The model has dimensions of 40 m in the y-direction, parallel to the fracture, 12 m in the z-direction, perpendicular to the fracture, and 51 m in the z-direction. Due to symmetry, only one-half of the problem is simulated, using the center of the fracture as the plane of symmetry. The open boreholes are simulated by a columns of gridblocks that are initialized with S_w=1. An initial effort to model this problem involved discretizing a small 3 mm fracture, with element sizes slowly increasing in the x-direction. This resulted in unacceptable numerical behavior, so a new approach was developed that uses a coarser discretization, but still captures the important physics of this problem. A fracture transmissivity, T_f can be defined as the product of the fracture aperture, b, and the fracture permeability, k_f:

$$T_f = k_f b \tag{3.7}$$

In a porous media model, the equivalent gridblock transmissivity would be

$$T_m = k_{rock} k_{rw} \Delta x \tag{3.8}$$

where Δx is the horizontal thickness of the gridblock perpendicular to the fracture. Using Equation 3.5, the initial S_w value that produces the desired fracture transmissivity can be calculated:

$$S_w = \left(\frac{k_f b}{k_{rock} \Delta x} \right)^{\frac{1}{3}} \tag{3.9}$$

The hydraulic fracture modeling discussed elsewhere in this report has indicated that it is feasible to make a vertical fracture with an aperture of approximately 3mm and dimensions of at least 25 m in the horizontal direction and 50 m in the vertical direction. This fracture will be initially held open with a proppant. If we assume that the proppant filling the fracture has an intrinsic permeability of $2x10^{-10}$ m^2, then the effective fracture transmissivity, T_f is $6x10^{-13}$ m^2. Using Equation 3.9, this initial fracture transmissivity can be obtained in a 2 cm thick gridblock with k_{rock} equal to 10^{-5} m^2 by using an initial S_w equal to 0.0144. In the field, as the fracture dissolves, the proppant will drop away, leaving an open fracture or channel with higher permeability than the propped fracture. The numerical model can account for this through the k_{rw} term. This is illustrated in Table 3.2 which shows the equivalent gridblock transmissivity (T_m) as a function of the fracture element S_w. The equivalent open fracture aperture calculated using the cubic law:

$$T_f = \frac{b^3}{12} \tag{3.10}$$

is also shown. As the rock in the fracture element dissolves, the permeability increases and approaches the open fracture cubic law transmissivity.

Table 3.2. Effective fracture transmissivity in the 2 cm thick fracture elements during dissolution.

S_w	**T_m, m^3**	**Equivalent b using cubic law for open fractures, mm**
0.0144	$6.0x10^{-13}$	0.19
0.02	$1.6x10^{-12}$	0.27
0.05	$2.5x10^{-11}$	0.67
0.10	$2.0x10^{-10}$	1.34
0.20	$1.6x10^{-9}$	2.68
0.40	$1.3x10^{-8}$	5.36
0.60	$4.3x10^{-8}$	8.03
0.80	$1.0x10^{-7}$	10.72
1.00	$2.0x10^{-7}$	13.40

Based on these arguments, the grid spacing in the x-direction, beginning at the center of the fracture (only one-half of the problem is modeled) is 1 cm, 3 cm, 6 cm, 10 cm, 20 cm, 60 cm, expanding to 2m. Parallel to the fracture, in the y-direction coarser spacing is used. The wells are assumed to have a 20 cm diameter (~8 inch), so the y-

spacing at the wells is 20 cm, increasing between the wells up to 6m. The vertical spacing is 7 m, except for the bottom 3 layers, which have thicknesses of 4 m. Each well occupies one gridblock in the y-direction, 3 gridblocks in the x-direction, and the boreholes extend from the second layer from the top, to the layer above the bottom.

The first set of simulations do not include a fracture, so the S_w in the fracture is set equal to 0.0002154 as in the other rock gridblocks. The k_{rock} value was set to 10^{-6} m^2 giving a formation intrinsic permeability of 10^{-17} m^2. Only a single well is simulated, with fresh water injection at a rate of 100 gallons per minute (full well basis) near the vertical center of the well. The brine is produced from the bottom of the well against a downhole well pressure of 20.2 MPa, or 2900 psi. Images of the cavern formation during the 140 day injection period are shown in Figures 3.3 through 3.9. By the end of the simulation, the cavern has just extended to the model boundaries, and the cavern volume (full basis) is 10,384 m^3 (366,700 ft^3). The total water injection (full basis) was 73,306 m^3, so the injected water to cavern volume ratio is 7.35, giving an average volumetric dissolving power of 0.136. Comparing this value to the theoretical maximum of 0.168, it can be seen that this process operated at 81% efficiency, which is typical of field salt solution mining efforts. Many approximations and assumptions were used in calculating the mass transfer during this simulation (darcy flow in cavern; constant mass transfer coefficient; equilibrium reaction between rock and fluid), so the predicted efficiency should be viewed with some caution. Nonetheless, this model predicts that a single-well configuration without a fracture could be viable for cavern formation.

The second case that was considered was similar to the first one, except that a 3 mm aperture fracture was considered, and k_{rock} was increased to 10^{-5} m^2, giving a formation intrinsic permeability of 10^{-16} m^2. The fracture is initially assumed to contain a 200 darcy permeability proppant, and as it dissolves, the permeability follows Table 3.2. As in the previous example, water is injected at 100 gpm in the center of the borehole, and brine is produced from the bottom against a constant wellbore pressure. The dissolved rock pattern is similar to the previous case, but it becomes elongated somewhat in the direction of the fracture (Figures 3.10 through 3.16). This elongation is particularly evident in the plot at 56 days (Figure 3.12). At the end of water injection, this cavern has a volume (full basis) of 11,474 m^3. Using the cumulative water injection of 73,306 m^3, the injected water to cavern volume ratio is 6.39, giving an average volumetric dissolving power of 0.156. This represents 93% efficiency, and it can be concluded that the presence of the fracture improved the mass transfer in this case relative to the unfractured case.

The final case involves water injection into the center of one borehole, with production from the bottom of the other borehole, located 23 m away. The boreholes are connected by a 3 mm fracture initially filled with a 200 darcy proppant. Otherwise, this simulation is identical to the previous case. Here the pattern of dissolution is much different, because flow is forced into the fracture (Figures 3.17 through 3.23).

Initially, the cavern forms around the injection borehole (Figures 3.17 and 3.18), but by 56 days of injection (Figure 3.20), a strong influence of the fracture is seen. A strong buoyancy flow is apparent in the fracture, as the dissolution occurs preferentially near the top of the fracture. After about 70 days of injection (Figure 3.21), the rock dissolution front breaks through into the production well, and after this time rock dissolution occurs throughout the cavern, including the production borehole. The

resulting cavern at the end of the 140 day injection (Figure 3.23) has a complex geometry that is clearly dominated by the effects of the fracture. A similar simulation that used a lower permeability proppant (20 darcy) did not produce this type of pattern, and the cavern that formed was more spherical in shape. Therefore, it appears that the transmissivity of the fracture is a critical parameter in the dissolved cavern morphology.

The two-well cavern shown in Figure 3.23 has a volume (full basis) of 12,508 m^3. Using the cumulative water injection of 73,306 m^3, the injected water to cavern ratio is equivalent to an average volumetric dissolving power of 0.170. This is slightly greater that the theoretical maximum dissolving efficiency (101%), so it may indicate a small mass balance error during the simulation. Despite this small inconsistency, it is apparent that this two-well configuration maximizes the overall mass transfer from the rock to the fluid, but it results in a complex cavern shape.

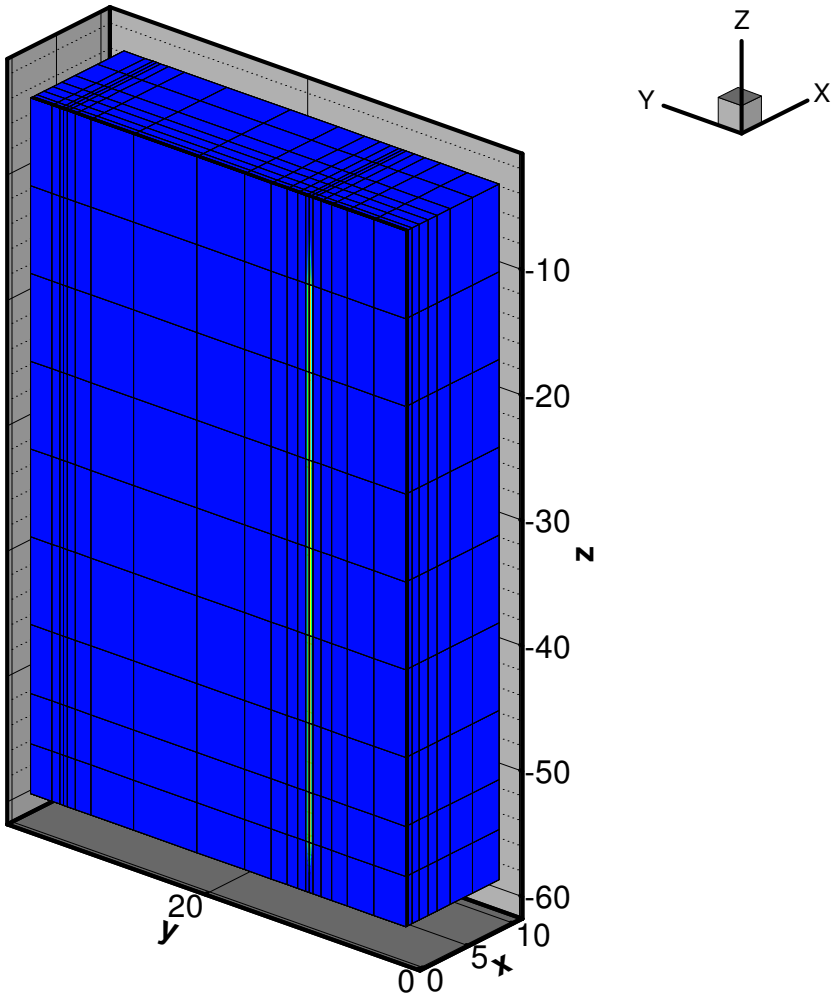

Figure 3.2. Numerical grid used in 3-D rock dissolution simulations. One well is shown, and the fracture extends along the x=0 face.

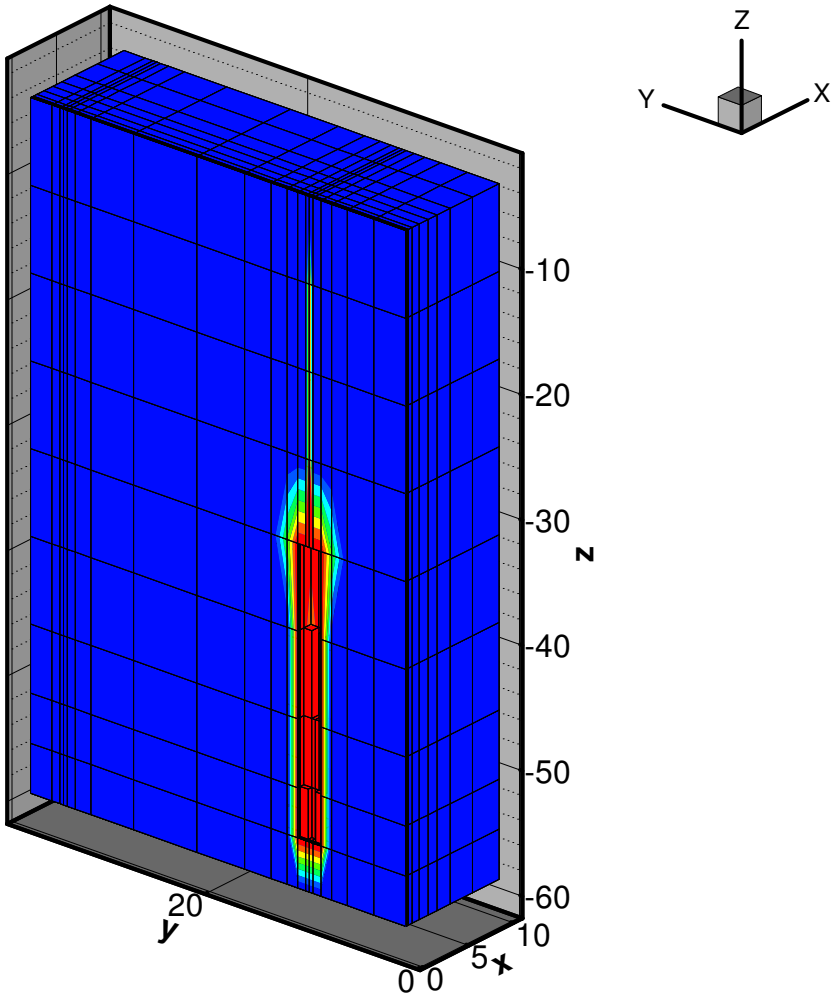

Figure 3.3. Single borehole with no fracture, inject 100 gpm for 5.5 days.

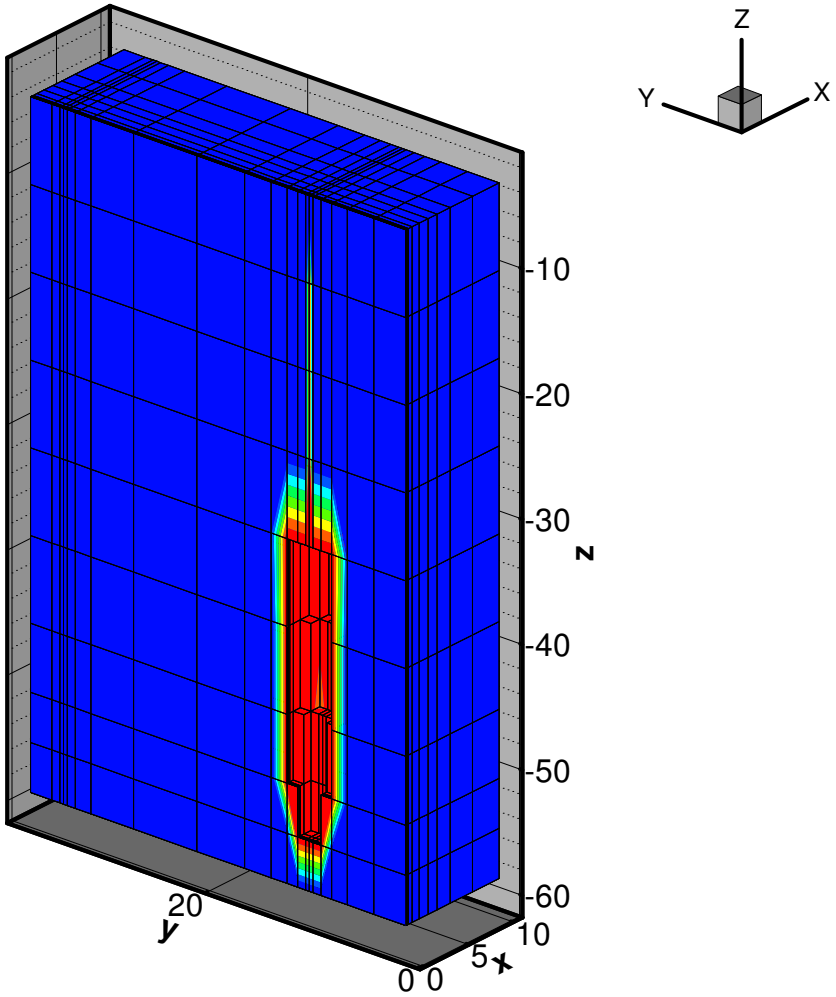

Figure 3.4. Single borehole with no fracture, inject 100 gpm for 14.0 days.

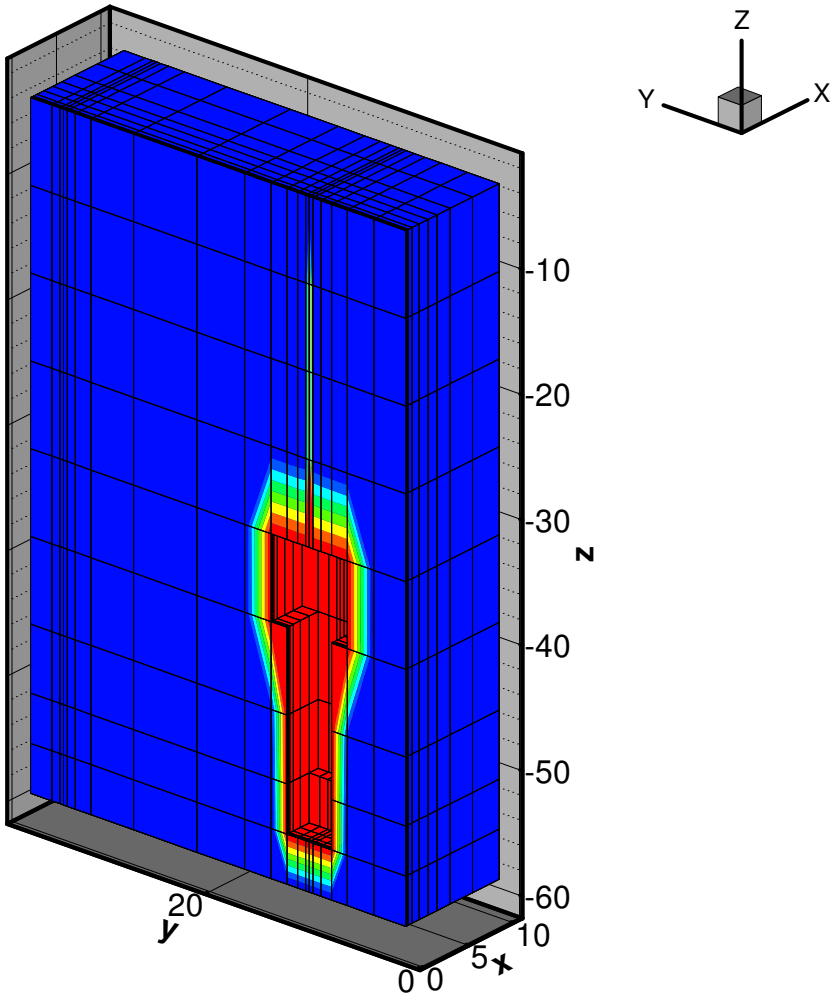

Figure 3.5. Single borehole with no fracture, inject 100 gpm for 28 days.

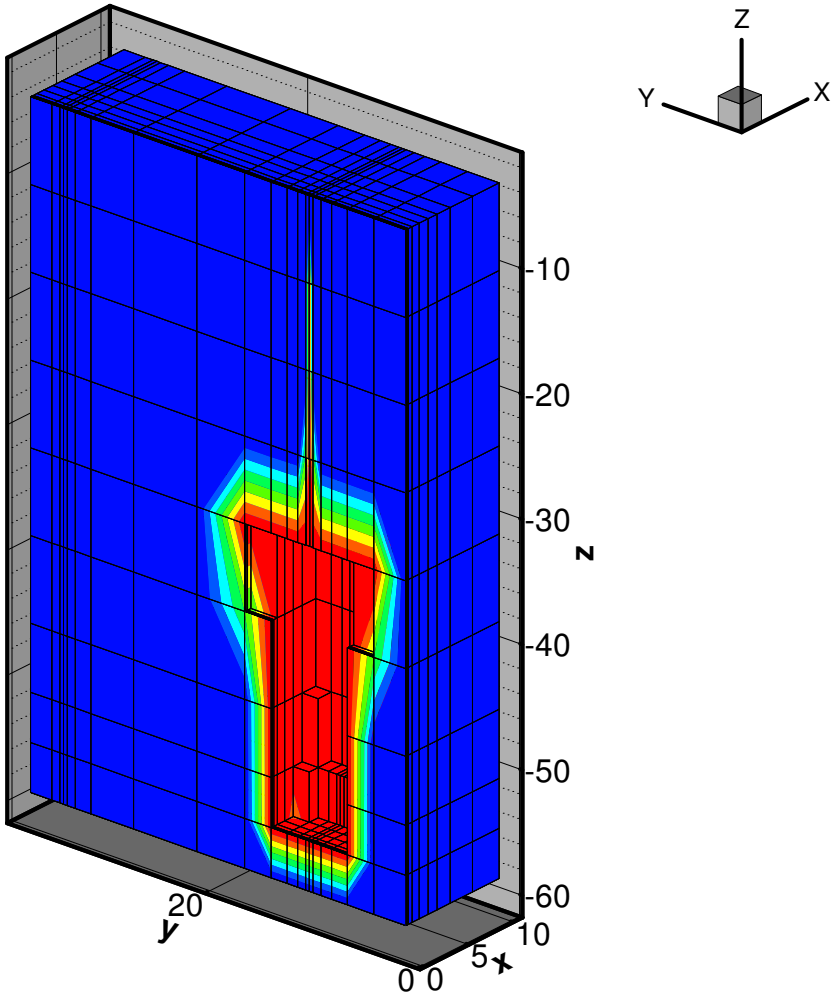

Figure 3.6. Single borehole with no fracture, inject 100 gpm for 56 days.

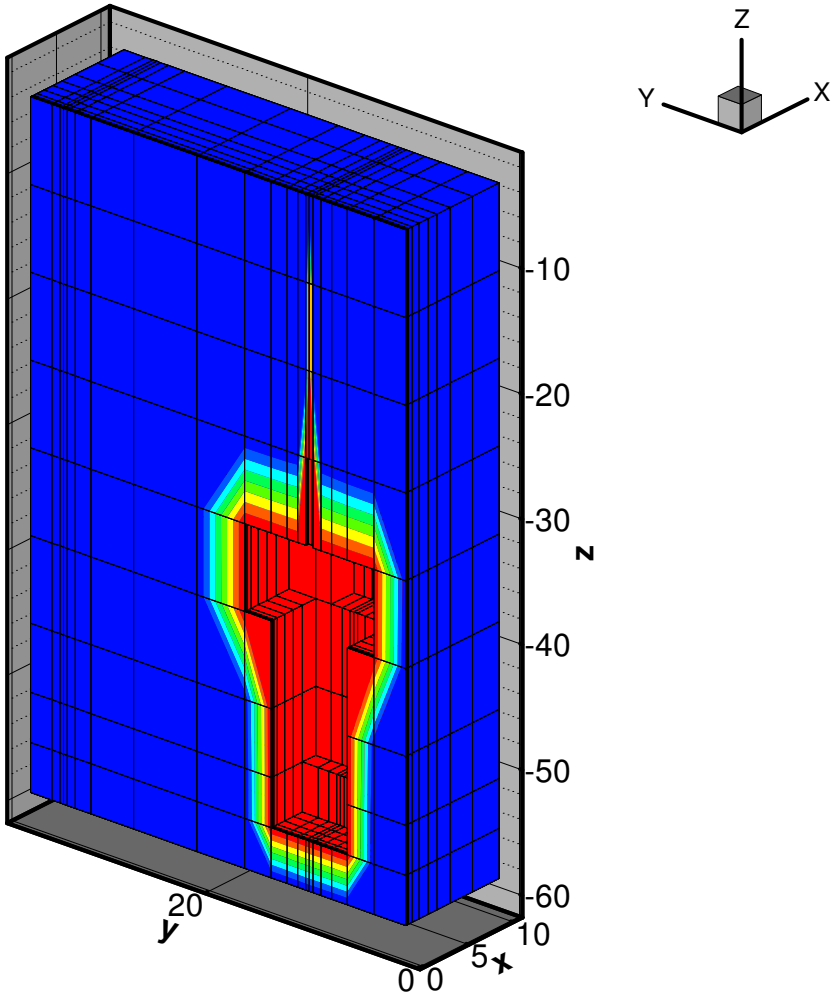

Figure 3.7. Single borehole with no fracture, inject 100 gpm for 70 days.

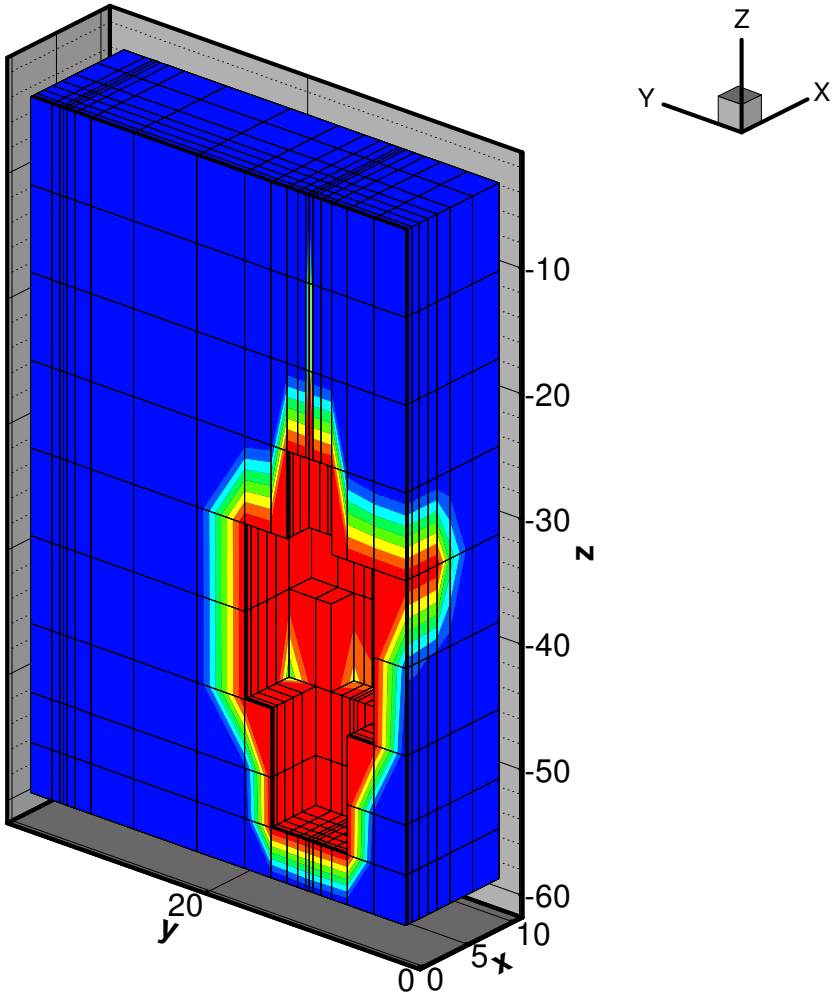

Figure 3.8. Single borehole with no fracture, inject 100 gpm for 98 days.

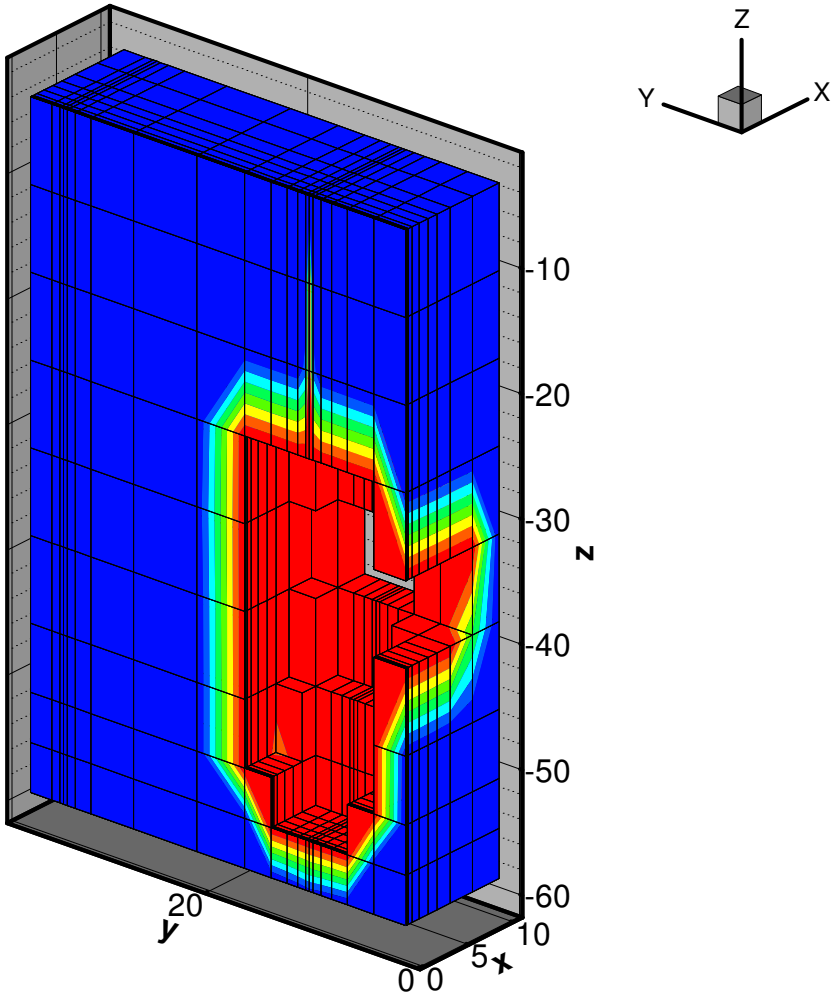

Figure 3.9. Single borehole with no fracture, inject 100 gpm for 140 days.

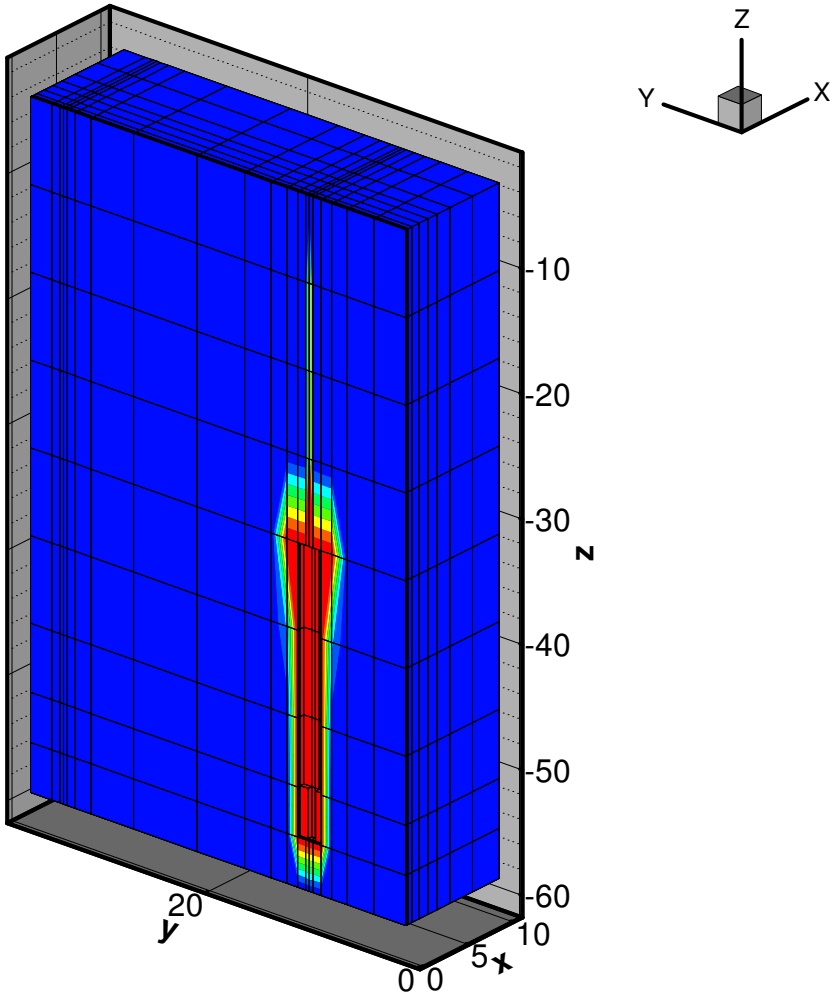

Figure 3.10. Single borehole with a 3 mm fracture, inject 100 gpm for 4 days.

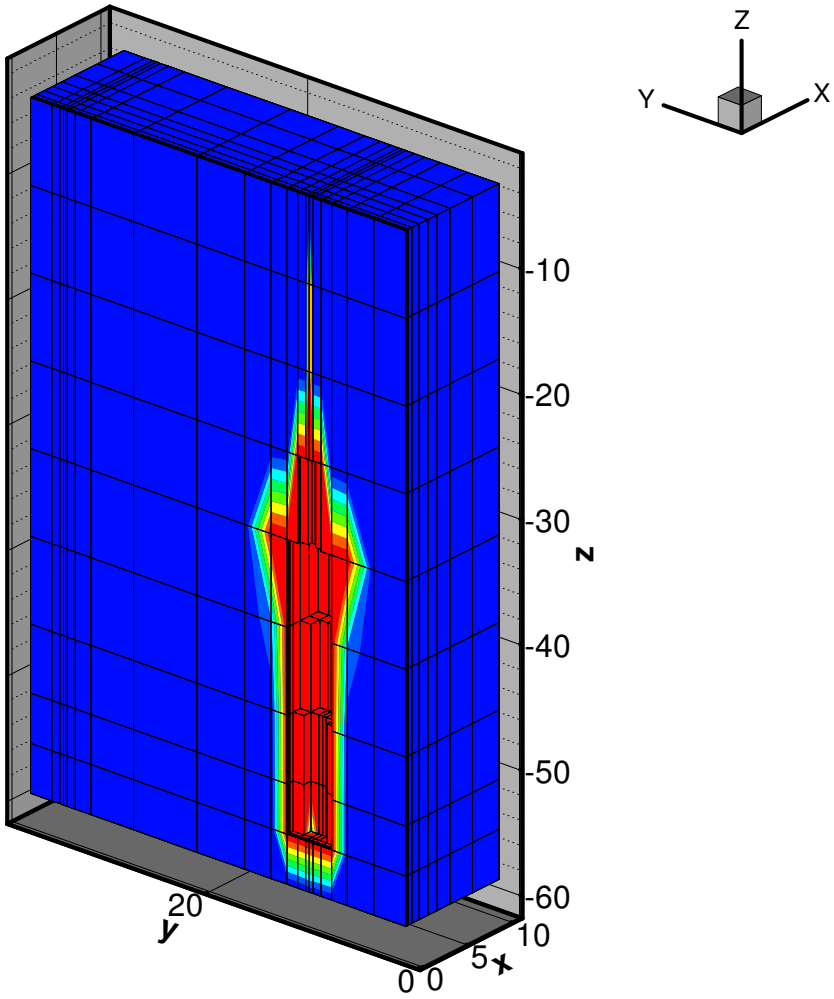

Figure 3.11. Single borehole with a 3 mm fracture, inject 100 gpm for 14 days.

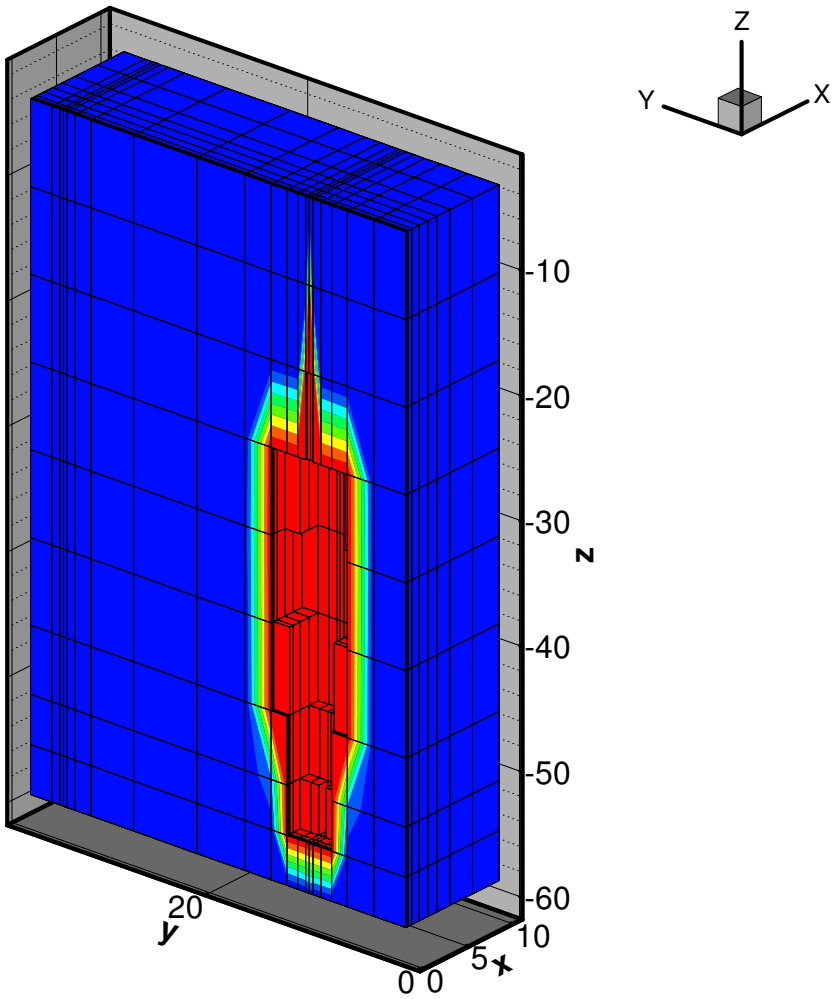

Figure 3.12. Single borehole with a 3 mm fracture, inject 100 gpm for 28 days.

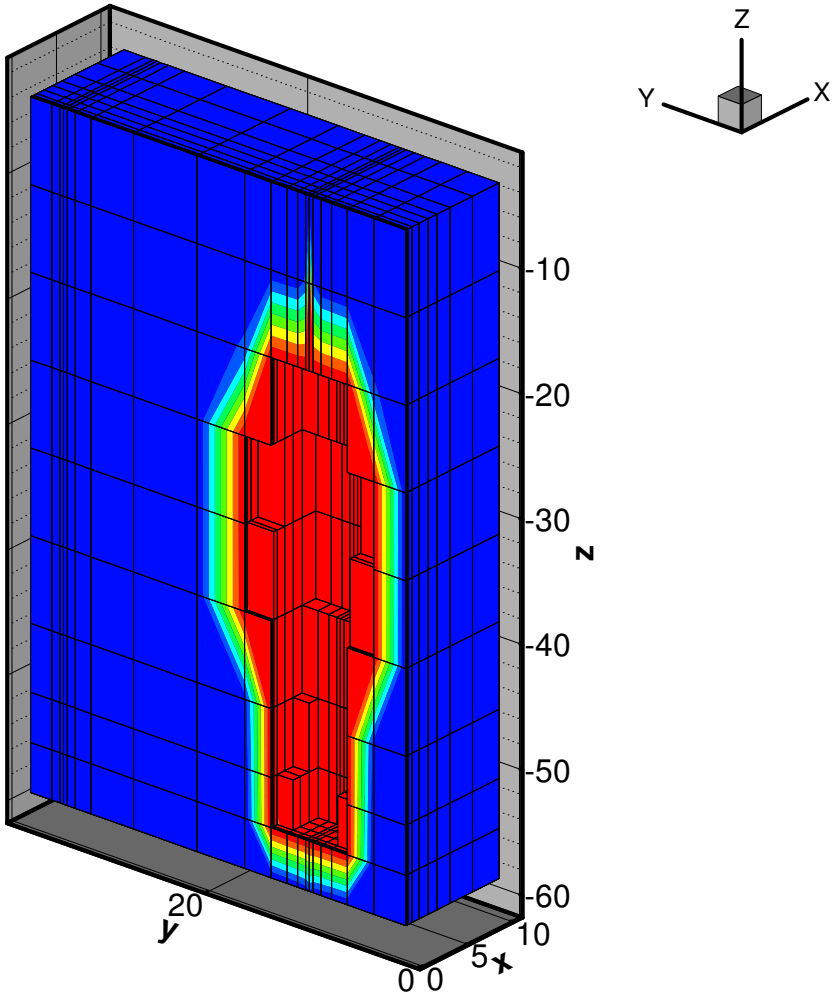

Figure 3.13. Single borehole with a 3 mm fracture, inject 100 gpm for 56 days.

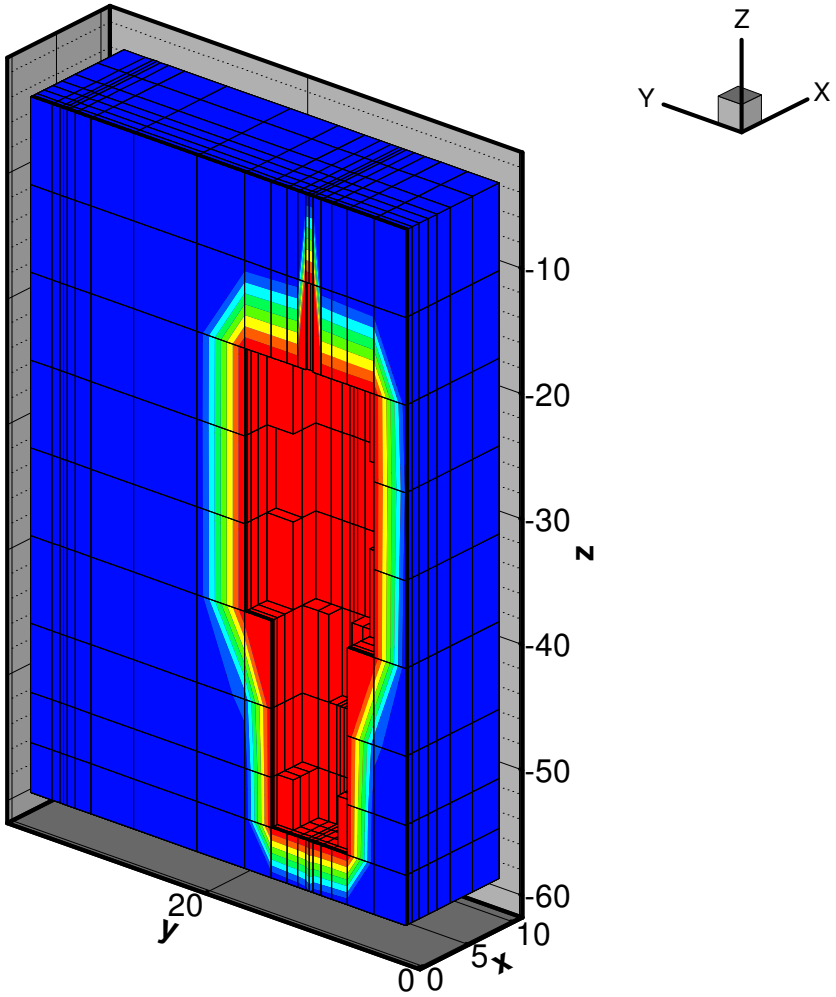

Figure 3.14. Single borehole with a 3 mm fracture, inject 100 gpm for 70 days.

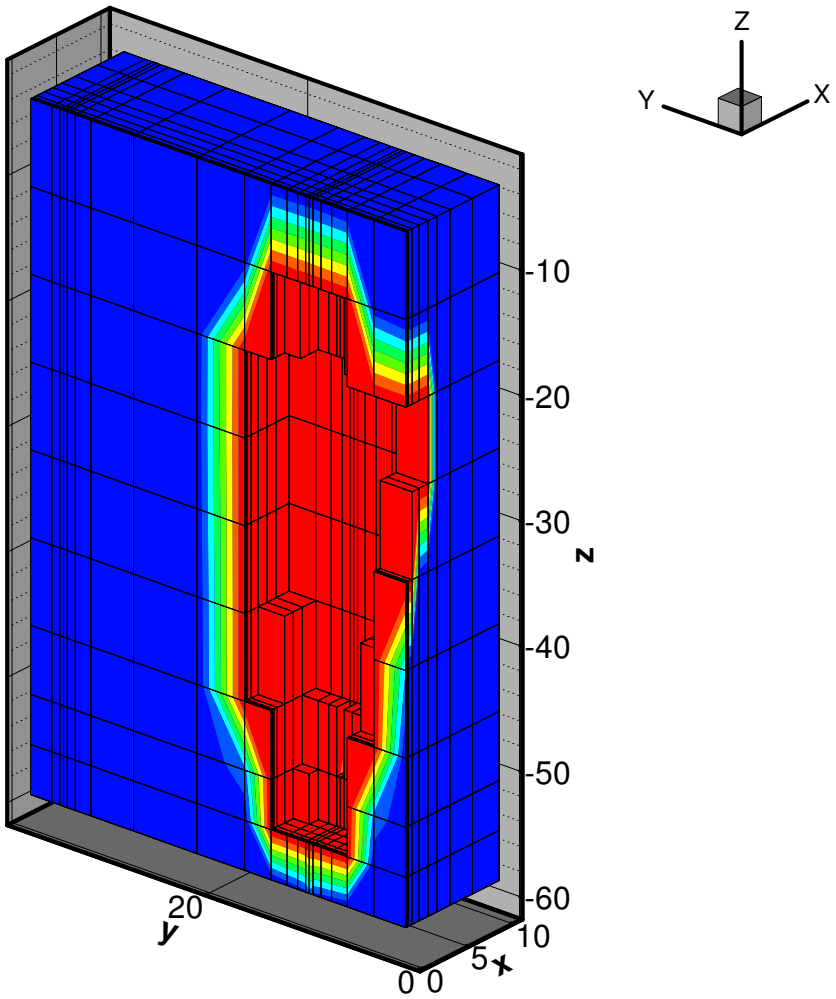

Figure 3.15. Single borehole with a 3 mm fracture, inject 100 gpm for 98 days.

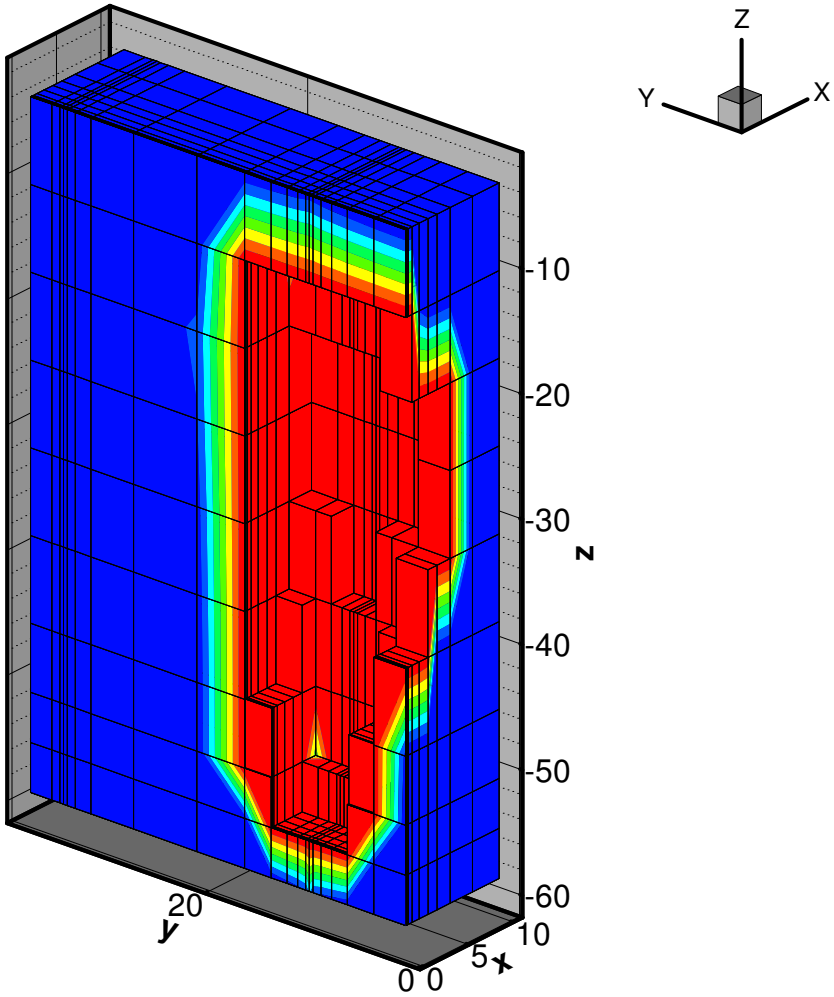

Figure 3.16. Single borehole with a 3 mm fracture, inject 100 gpm for 140 days.

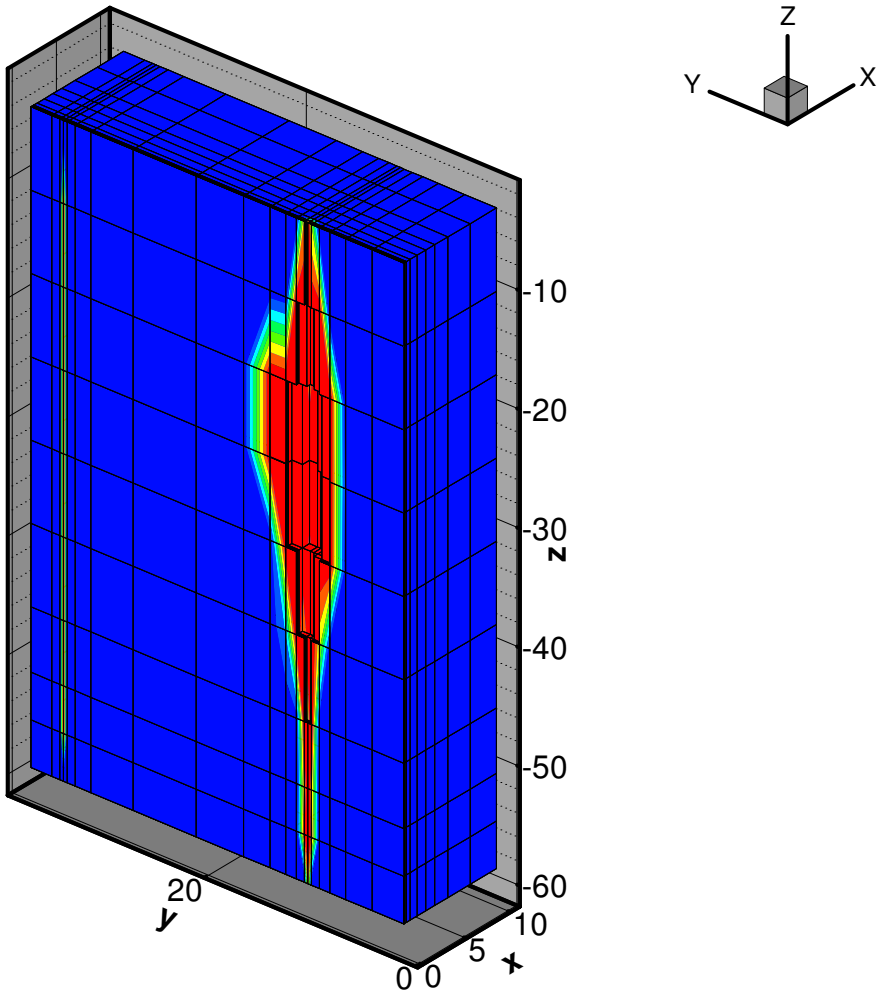

Figure 3.17. Two boreholes connected by a 3 mm fracture, inject 100 gpm for 4.9 days.

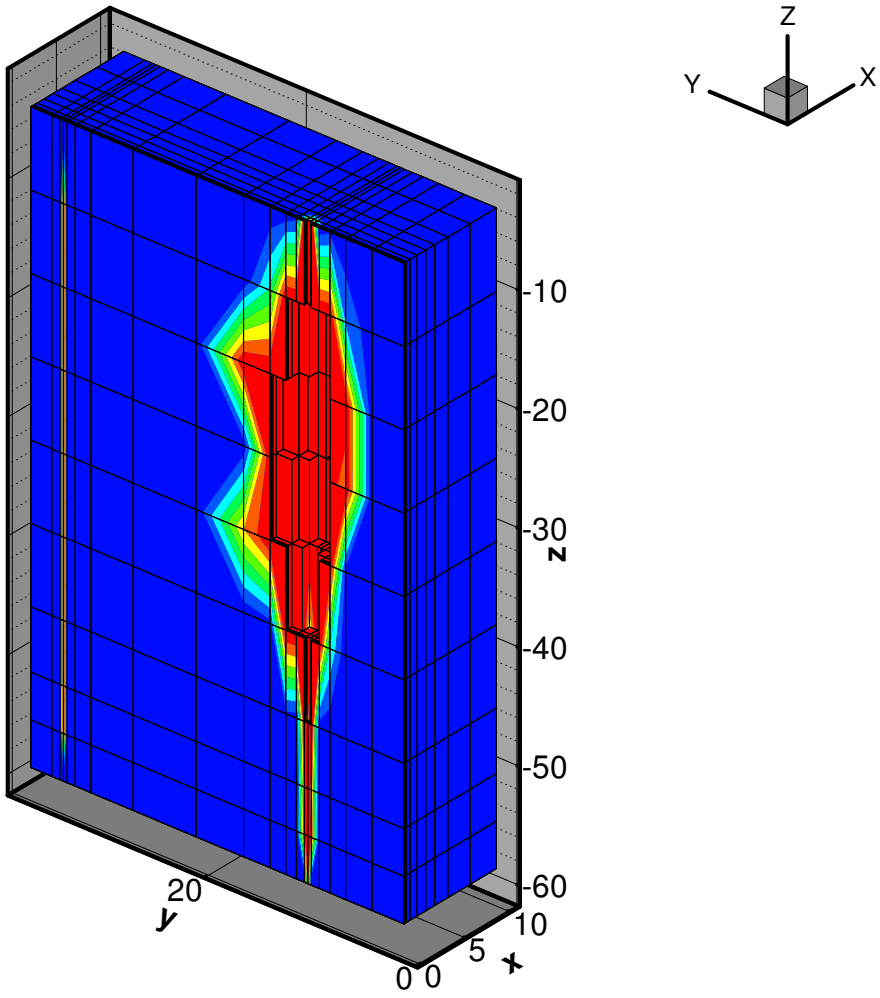

Figure 3.18. Two boreholes connected by a 3 mm fracture, inject 100 gpm for 14 days.

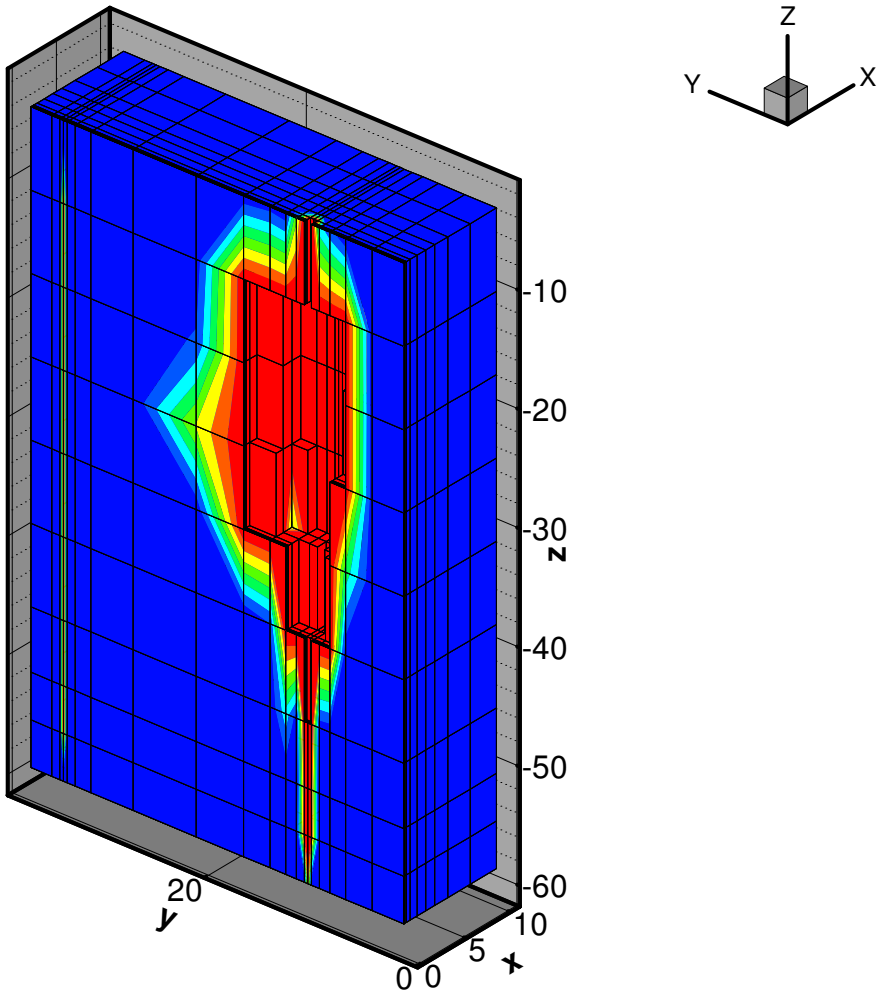

Figure 3.19. Two boreholes connected by a 3 mm fracture, inject 100 gpm for 28 days.

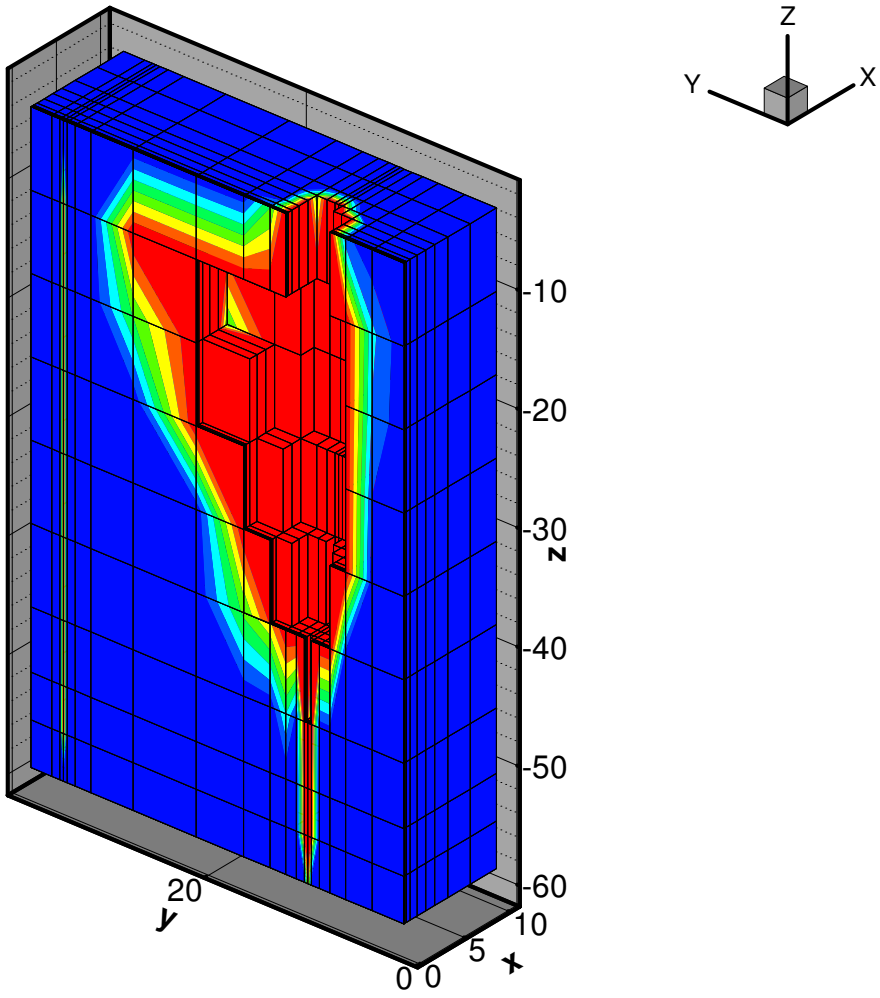

Figure 3.20. Two boreholes connected by a 3 mm fracture, inject 100 gpm for 56 days.

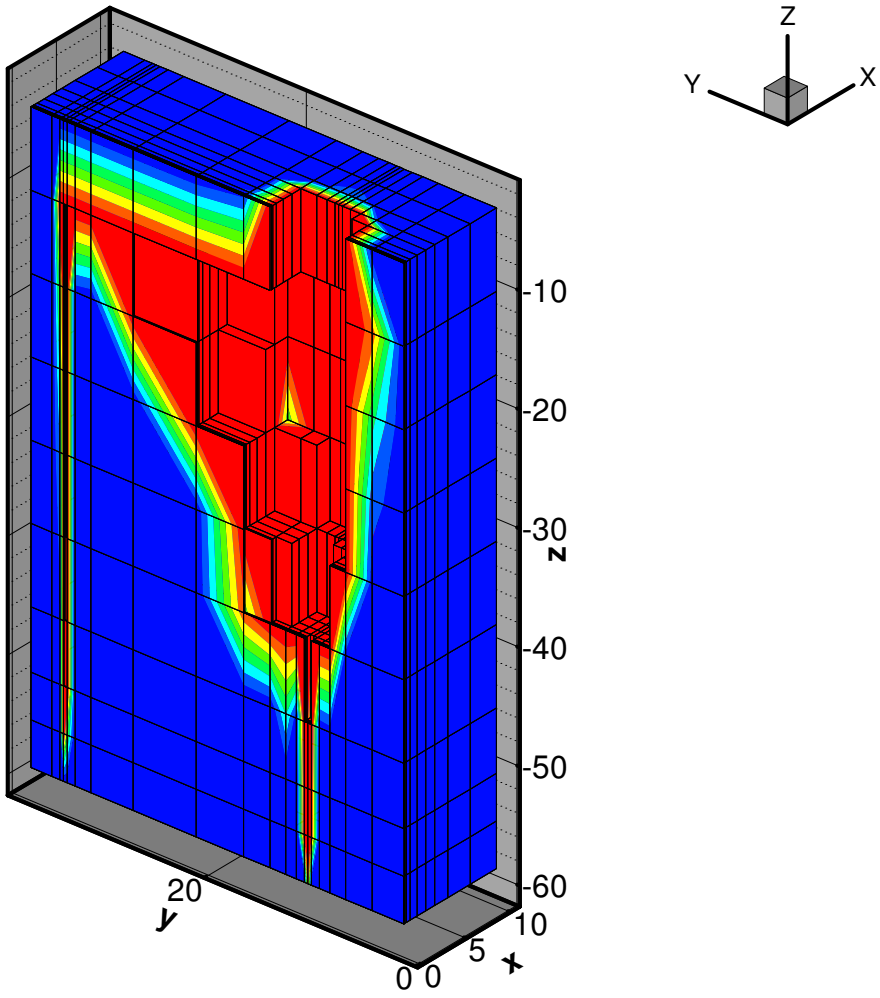

Figure 3.21. Two boreholes connected by a 3 mm fracture, inject 100 gpm for 70 days.

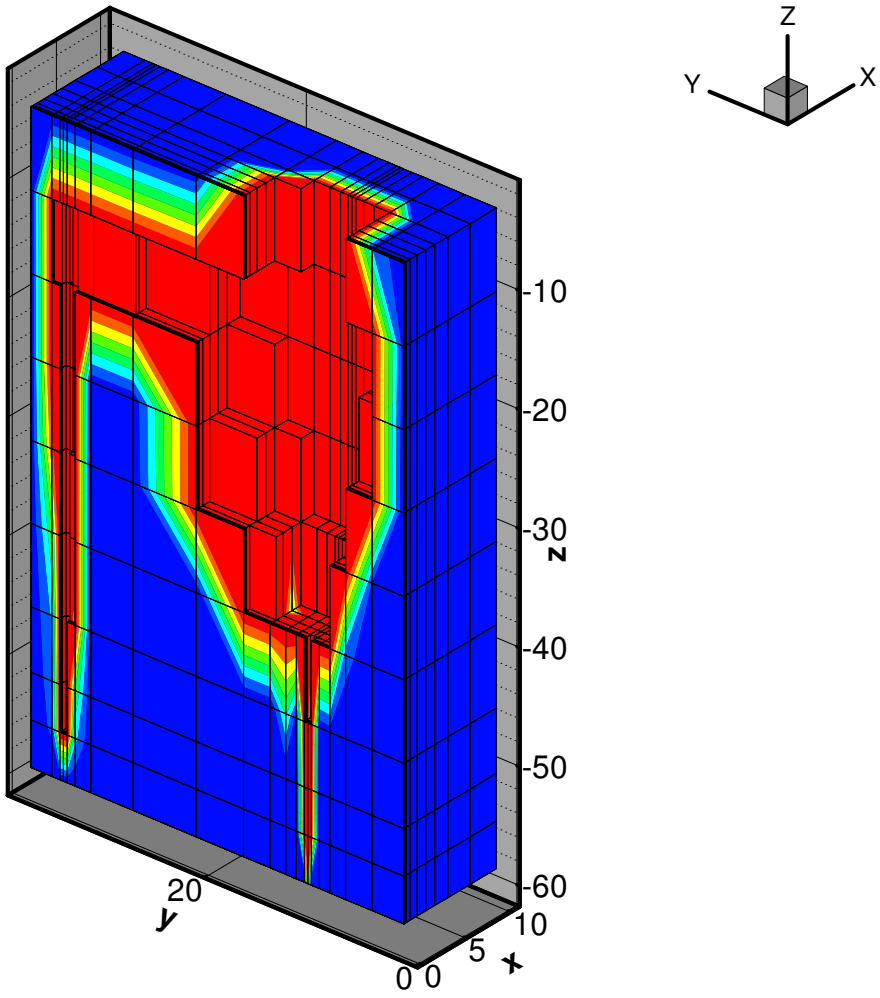

Figure 3.22. Two boreholes connected by a 3 mm fracture, inject 100 gpm for 98 days.

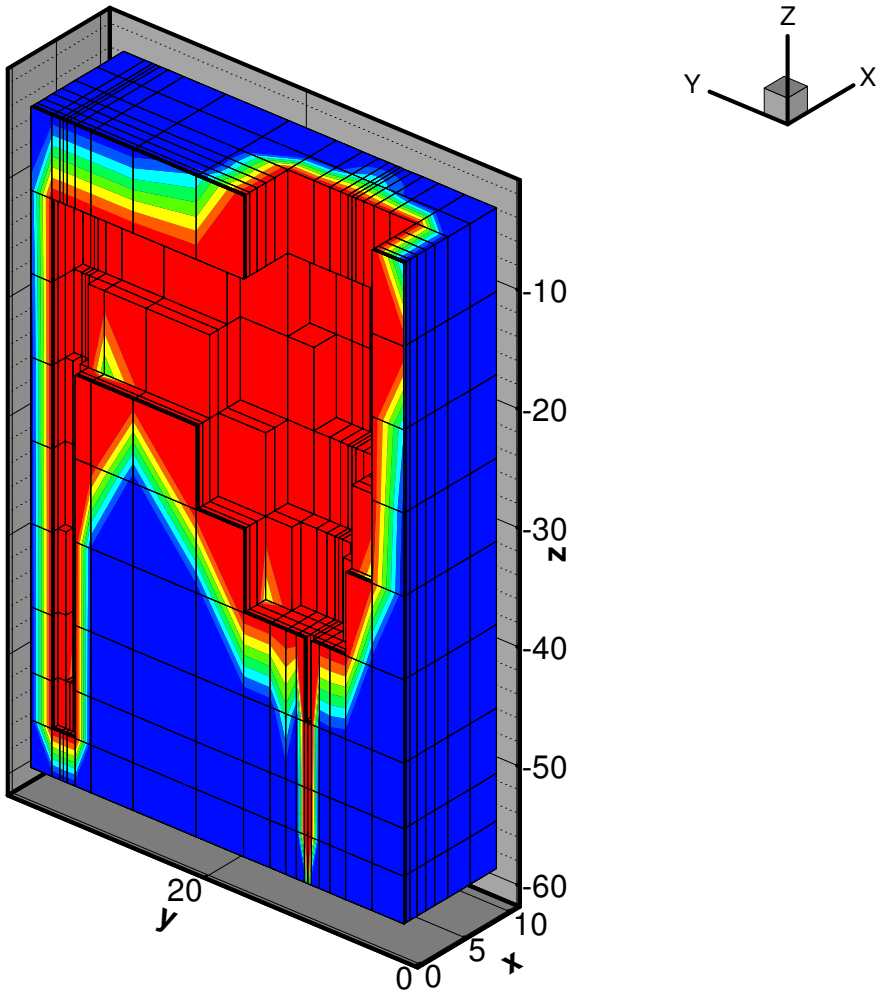

Figure 3.23. Two boreholes connected by a 3 mm fracture, inject 100 gpm for 140 days.

Simulation of the Full Geochemical Reaction with Supercritical CO_2 Production

As we have documented, the production of a supercritical CO_2 phase is an important aspect of the subsurface acid dissolution process. We have been using the new DOE TOUGHREACT/ECO2 code developed at the Lawrence Berkeley National Laboratory (Xu et al., 2003a) to simulate this process. TOUGHREACT/ECO2 is a three-dimensional multiphase flow integral finite difference code based on the TOUGH2 formulation (Pruess, 1991). TOUGHREACT couples a comprehensive geochemical treatment (see, for example Xu et al., 1999) with the TOUGH2 nonisothermal multiphase multicomponent transport capability. TOUGHREACT therefore can simulate reactive chemical transport in two-phase gas-aqueous systems with heat transfer and phase change in both porous and fractured (and porous fractured) rocks. TOUGHREACT allows for permeability changes as the porosity changes due to mineral dissolution or precipitation. However these effects are not fully coupled in the Newton-Raphson interations in the flow model, and Xu et al. (2003a, 2004) have noted that have noted that including the dynamic permeability changes with porosity changes results in a large computational penalty. The mineral precipitation and dissolution process can be simulated using equilibrium or kinetic reaction models.

The TOUGHREACT/ECO2 model (Xu et al., 2003a) couples a full thermodynamic model for supercritical CO_2 behavior with TOUGHREACT. The ECO2 module for TOUGH2 was developed by Pruess and Garcia (2002) for simulating CO_2 disposal in deep saline aquifers. It provides an accurate model for the thermophysical behavior of mixtures of CO_2 and water at temperatures between 5 and 103 C, and pressures between 75 and 400 bar (Pruess and Garcia, 2002).

One major shortcoming of the TOUGHREACT/ECO2 model for the present work is that the aqueous phase density and viscosity are assumed to be constant, and are not linked to the production or consumption of chemical species in the reactions (Xu et al., 2004). As we have noted the fluid density effects are quite important in the field acid dissolution process.

TOUGHREACT is now distributed (for a fee) by the DOE Energy Science and Technology Software Center, but we received an early version of the code directly from Dr. Xu at the Lawrence Berkeley National Lab in June, 2004, just prior to the public release of the code. Our initial attempts to simulate the injection of a concentrated HCl solution into a pure limestone with the TOUGHREACT/ECO2 version were somewhat disappointing. It did not appear as though the chemical reactions (the REACT module) were correctly communicating with the flow part of the code (the TOUGH ECO2 module). However, when we ran TOUGHREACT using a subcritical CO_2 module (TOUGHREACT/EOS2), the results were more reasonable. After some communication with Dr. Xu, we received an updated version of TOUGHREACT that fixes a bug in the REACT to ECO2 coupling. Subsequent TOUGHREACT simulations have been performed using this new version (dated January, 2005).

So far, we have been focusing on the chemistry and phase behavior of the problem, using one-dimensional simulations. TOUGHREACT can consider hundreds of aqueous species and minerals, but we are primarily concerned with only those components that appear in the basic limestone dissolution reaction, Equation I-1. The primary aqueous species in our simulations are: H_2O, H^+, HCO_3^-, Cl^-, and Ca^{+2}, while the

only mineral considered is calcite, $CaCO_3$, and the only gas (actually supercritical fluid) considered is pure CO_2. TOUGHREACT can automatically compute the secondary aqueous species that can appear due to various reactions, and for our case, these include: CO_2^{-2}, CO_2(aq), OH^-, $CaCl^+$, $CaCl_2$(aq), $CaCO_3$(aq), $CaHCO_3^+$, $CaOH^+$, and HCl(aq).

TOUGHREACT problems are initialized using an initial water composition, saturation, and pressure. Injected water can have a different composition, but as mentioned above, the density is constant. For our 30% HCl solution, we have about 10 moles of acid per liter of acid solution. In the simulations, this is specified using a "boundary water" composition that contains 10 moles per liter of the H^+ and Cl^- primary species. The calcite rock mineral is assumed to undergo equilibrium reactions with the acid, due to the rapid reaction rate.

A one-dimensional problem 10 m long and 1 m in cross section has been used to study the process. This horizontal limestone column initially has a porosity of 10%, and a high permeability of 10^{-12} m^2 (one darcy). Acid is injected at one end of the column at a rate of 1 m^3 per day, and fluids are produced at the other end against a constant pressure of 20 MPa (2900 psi). The temperature is maintained at 60 C. Due to the very large amounts of CO_2 produced in the dissolution reaction, simulation pressures can easily go out of the range of the code if some outlet for the fluids is not available. These simulations usually run quickly, although the model can be very sensitive to the exact initial and boundary conditions. The results of the 1-D simulations are shown in Figures 3.24 through 3.27.

As the acid is injected, a supercritical CO_2 phase quickly appears, and flows towards the outlet (Figure 3.24). Within one day, the model has predicted CO_2 breakthrough at the outlet. CO_2 phase saturations on the order of 0.1 persist in the column until all of the limestone has dissolved. The CO_2 phase pressure quickly jumps by 4 bar at the injection end of the column during the first day (Figure 3.25). At this time, all of the CO_2 is being produced in this first gridblock from the dissolution reaction, and this CO_2 flows out the other end of the column under its own pressure gradient. With time, the CO_2 phase pressure gradient diminishes due to the increasing permeability of the dissolving rock. Note that this pressure gradient would be much higher if the limestone permeability were lower in this simulation. We also noted that the pressure gradient is more than two times larger if the simulation is run at atmospheric boundary pressure due to the higher compressibility factor (z~1) at this pressure compared to the compressibility factor at 20 MPa and 60 C of about 0.44. At this temperature and pressure, the supercritical CO_2 phase density is 730 kg/m^3, and the viscosity is 0.061 cP. At this temperature, pure water viscosity is 0.47 cP, so the supercritical CO_2 phase has a liquid-like density, but a gas-like viscosity, and it is more than twice as compressible as an ideal (room temperature and pressure) gas.

The initial pH in the column (Figure 3.26) was 6.44, but this quickly drops as acid reacts with the limestone to produce CO_2 and carbonic acid, with a resulting pH of 4.24. As the dissolution reaction proceeds, the dissolution front can be tracked by the step pH change that occurs where the rock has been completely dissolved. In these locations, the pH is –0.53, reflecting the unreacted HCl solution.

The calculated dissolution pattern (Figure 3.27) shows the dissolution and removal of the rock from the upstream end of the column. While these results seem qualitatively correct, the calcite dissolution process was specified to be an equilibrium

reaction. We would expect such a reaction to proceed as a step function (like the pH in Figure 3.26), so it is rather surprising that these porosity profiles in the column are smooth, showing some rock dissolution throughout the column. Given the volumetric dissolving power of 30% HCl of 0.175, we would expect all of the rock (9 m^3) to be dissolved with 51.4 m^3 of acid, or after 51.4 days. However the simulation shows that the calcite does not disappear until after 60 days. We have not been able to determine a plausible geochemical reason for this behavior, and at the present time, we are trying to track down and fix this apparent inconsistency.

Despite the somewhat perplexing rock dissolution behavior noted above, we have gained useful insights into the acid dissolution process with our TOUGHREACT simulations so far. During the coming year, we will continue to use this code (with the appropriate modifications) to model the acid dissolution process.

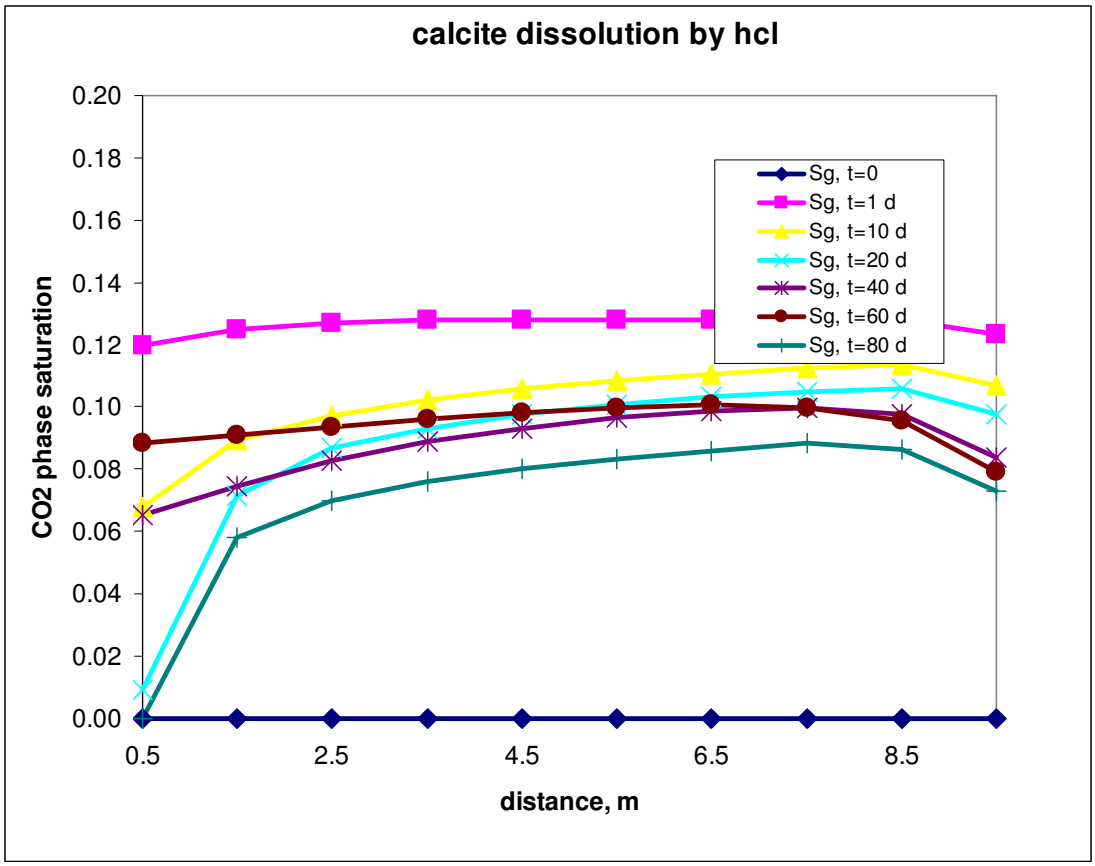

Figure 3.24. Supercritical CO_2 phase saturation in the 1-D column simulation.

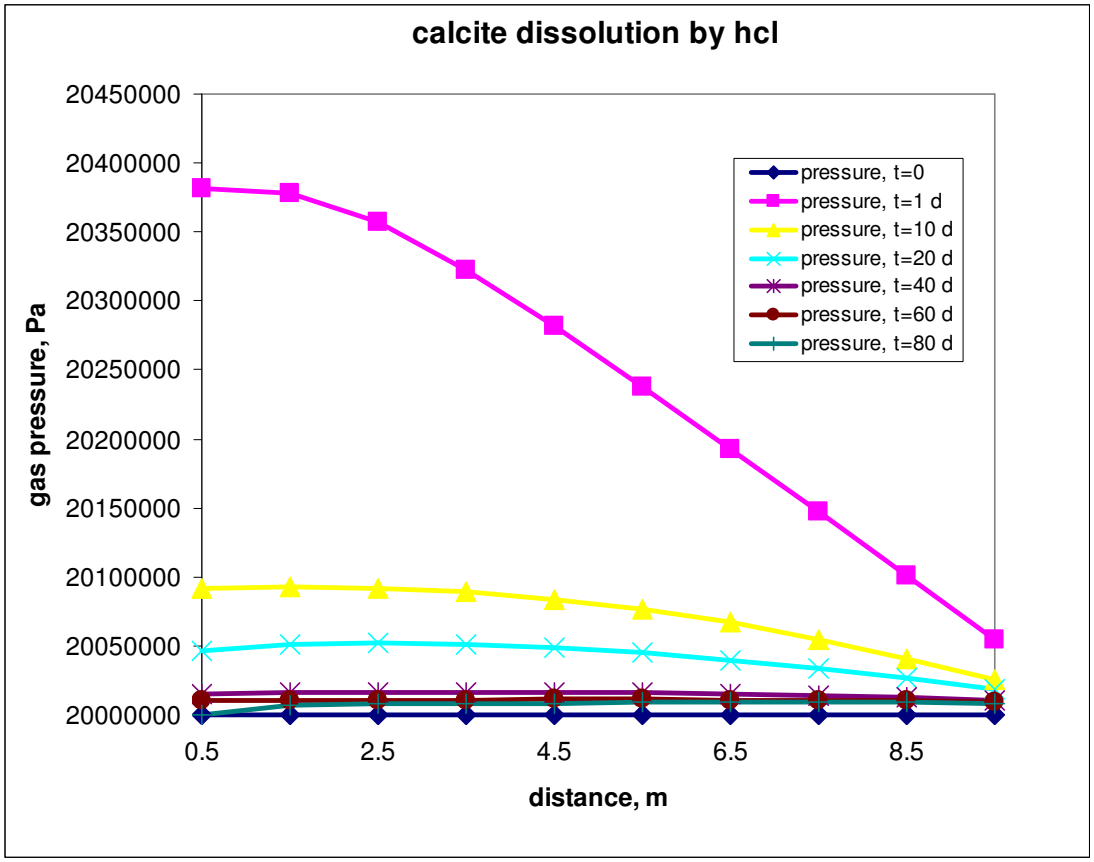

Figure 3.25. CO_2 phase pressure in the 1-D column simulation.

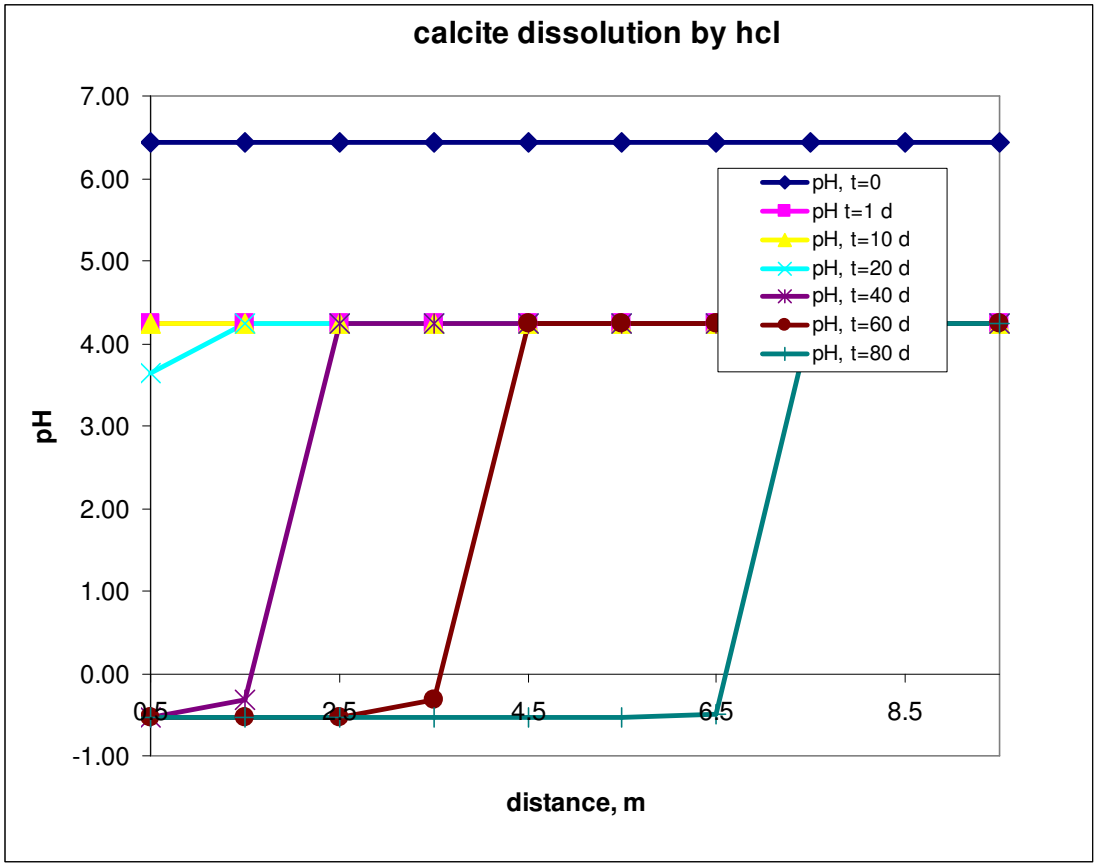

Figure 3.26. Aqueous pH in the 1-D column simulation.

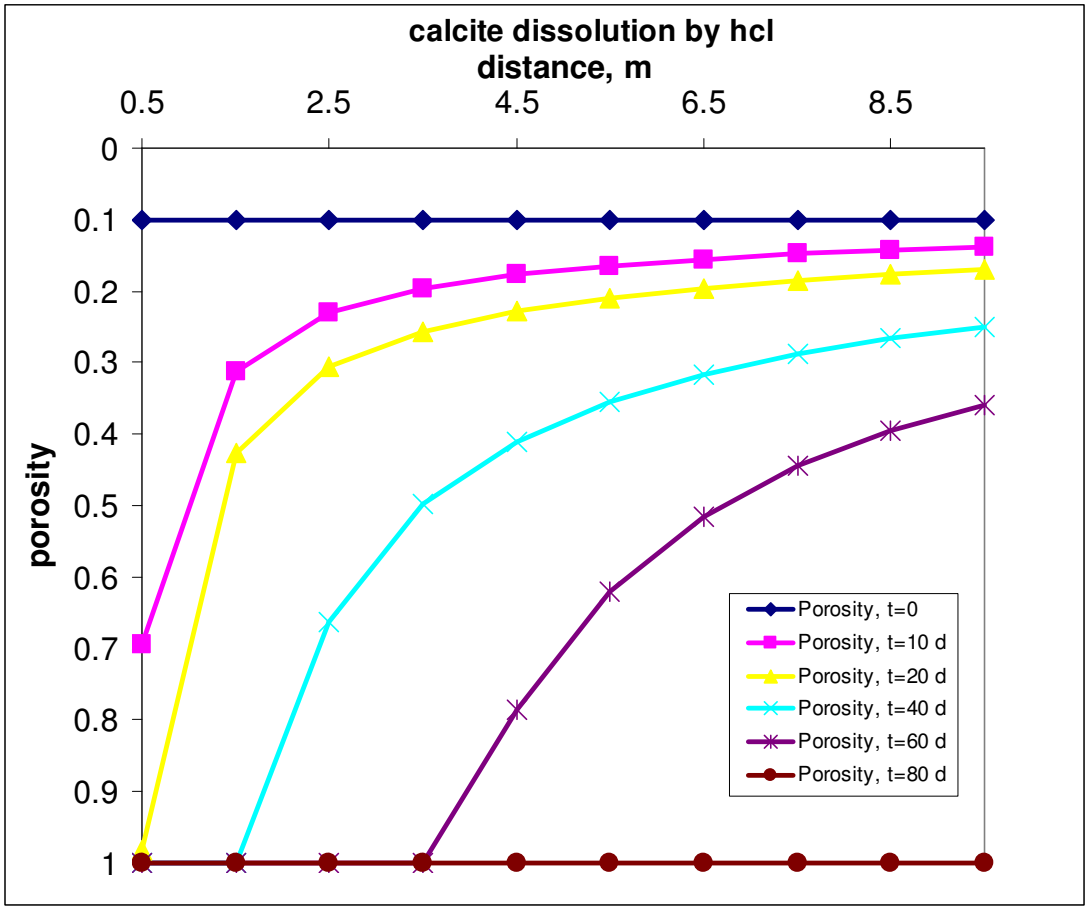

Figure 3.27. Calcite porosity in the 1-D column simulation.

Simulation of Cavern Storage of Natural Gas

A series of numerical simulations were performed to evaluate the ability of an open cylindrical cavern in a porous media to store natural gas. These simulations were performed using the TMVOC multiphase simulator (Pruess and Battistelli, 2002). This simulator can consider multiple condensable and noncondensable hydrocarbon gases, using the real gas law. The simulations of cavern storage only considered the injection of pure methane (CH_4), but other gas mixtures could be considered. The simulations used a radially symmetric r-z grid with 20 elements in the radial dimension, and 52 elements in the vertical dimension. The cavern was discretized as a vertical cylinder, with a radius of 10 m, and a height of 180 m. The volume of this cavern is therefore 56,549 m^3, or 2,000,000 ft^3. The numerical grid extends out to a radius of 500 m, and it is 525 m tall (Figure 3.28).

The top of this cavern is located at a depth of 1840 m (6000 ft), and hydrostatic boundary conditions are used on all of the model boundaries (top, bottom, outer edge) to reflect this depth. The reservoir temperature is assumed to be constant at 65C. Each simulation consists of two parts. In the first part, methane is injected into the top of the cavern, displacing water from the bottom of the cavern against a downhole pressure of 19.8 MPa (2850 psi). Methane is injected for 60 days at a constant mass rate of 1.3 kg/s. for a total of 6,740,000 kg, or about 360 MCF. This is just enough gas to fully fill the cavern if there is no gas leakage into the surrounding formation, and the gas compression at this temperature and pressure is about a factor of 180 times above standard conditions, yielding a downhole methane gas density of about 120 kg/m^3. Following this gas injection period, the gas is stored for 5 years.

Simulations were run using formation permeabilities of 10^{-18} m^2 to 10^{-15} m^2, or from 1 microdarcy to 1 millidarcy. The formation porosity was set to 0.1 in each case, and standard two-phase gas-water relative permeability curves were used in the formation. The cavern was given a porosity of 1 and permeability of 10^{-9} m^2.

The gas phase saturation after the 60 day injection period for the 1 microdarcy case is shown in Figure 3.28. As can be seen, all of the gas is contained in the cavern with no leakage into the surrounding formation. After 5 years of storage (Figure 3.29), virtually all of the methane remains in the cavern.

The case with a formation permeability of 10 microdarcies behaves in a similar fashion. After the 60 day injection period, virtually all of the methane is contained in the cavern. After a 5 year storage period (Figure 3.30), almost all of the methane is still contained by the cavern. When the formation permeability is increased to 100 microdarcies (0.1 millidarcy), the behavior starts to change. After the 60 day injection period, almost all of the gas is contained within the cavern. However, after 5 years, about 15% of the gas has leaked out of the top of the cavern into the formation (Figure 3.31).

When the formation permeability is increased to 1 millidarcy, the behavior of the gas in the cavern is dramatically different. The gas distribution at the end of the 60 day injection period is shown in Figure 3.32. Although most of the gas is contained in the cavern at this time, there is also significant gas leakage into the formation. After 180 days (60 days of injection, 120 days of storage), more leakage is evident (Figure 3.33), although most (~85%) of the gas is still contained in the cavern. However, after 1 year (Figure 3.34), much of the gas has leaked out of the cavern, and the bottom of the cavern

is filling with water. At this time, the cavern only contains about two-thirds of the injected amount. After 2 years, more than half of the methane has leaked out of the cavern, and by 3 years (Figure 3.35), less than a third of the methane remains in the cavern. By a time of 5 years the cavern is full of water, and all of the methane is in the permeable formation.

These simulations suggest that formation permeabilities that are greater than 1 millidarcy may allow for substantial gas leakage out of the cavern. If the top of the cavern is bounded by a lower permeability formation, this may be acceptable, but if the formation is continuous, the leakage rate may be too high, depending on storage requirements.

The cavern geometry used in these simulations was a long, narrow vertical cylinder. Due to the low methane density at reservoir temperature and pressure (about 120 kg/m^3), as the cavern is filled with gas, a pressure imbalance with respect to the formation water develops. The formation water is at hydrostatic pressure, and in order to displace water from the cavern, the gas pressure at the bottom of the cavern is at least as high as the hydrostatic pressure at this elevation. However, because the gas density is much lower than that of water, the gas pressure at the top of the cavern is substantially greater than the hydrostatic pressure at this elevation. This results in gas leakage out of the top of the cavern if the formation permeability is high. This pressure imbalance would be reduced if the vertical dimensions of the cavern were reduced.

During the next year, we will examine several different cavern configurations with various formation properties and boundary conditions.

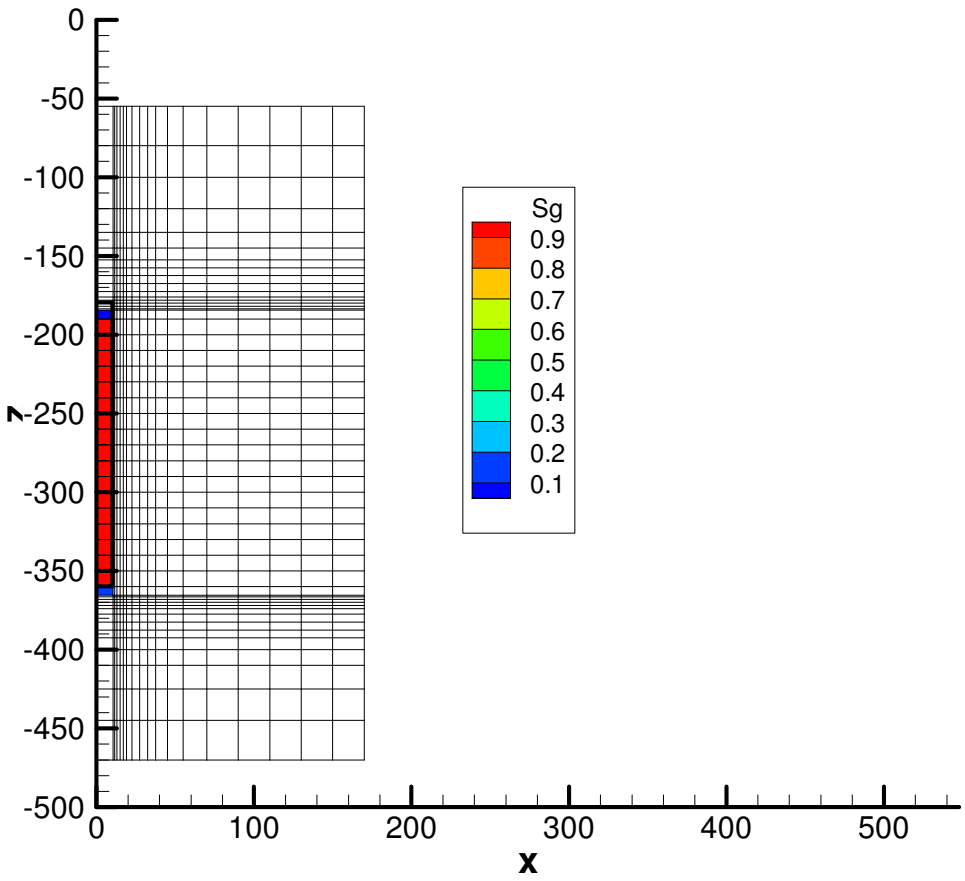

Figure 3.28. Radially symmetric grid used for gas storage simulations. The cylindrical cavern has been filled with methane for the case where the formation permeability is 1 microdarcy.

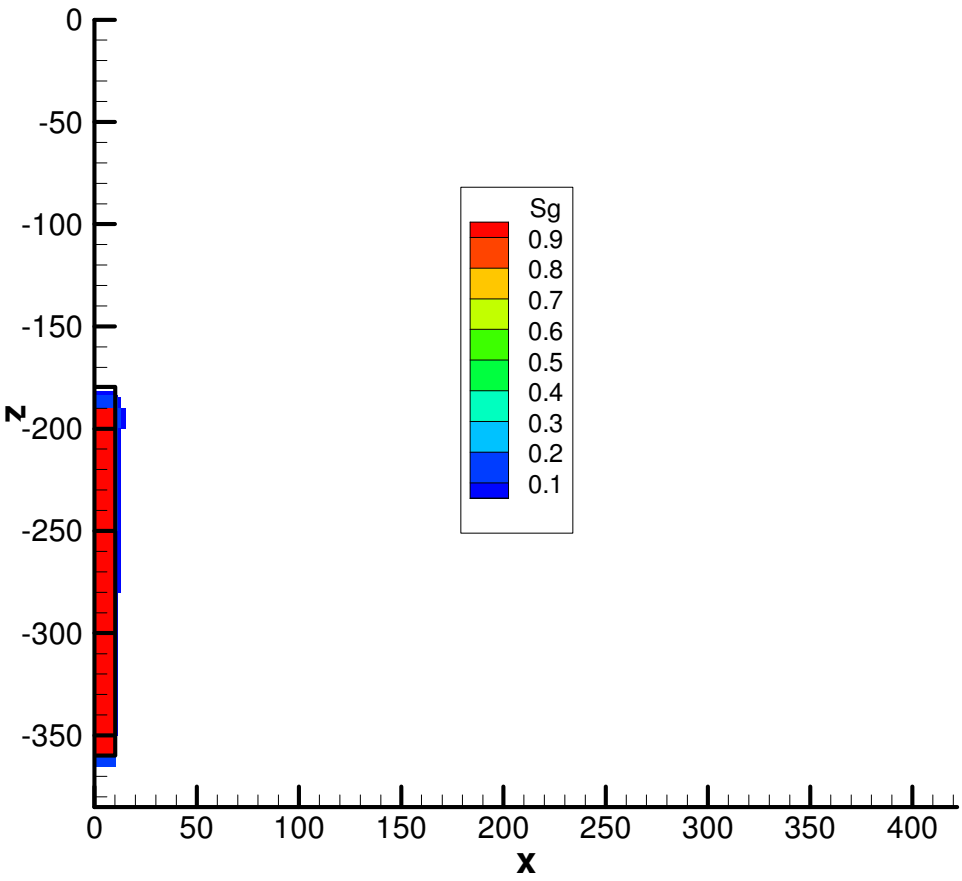

Figure 3.29. Methane gas distribution after 5 years of storage for the 1 microdarcy case.

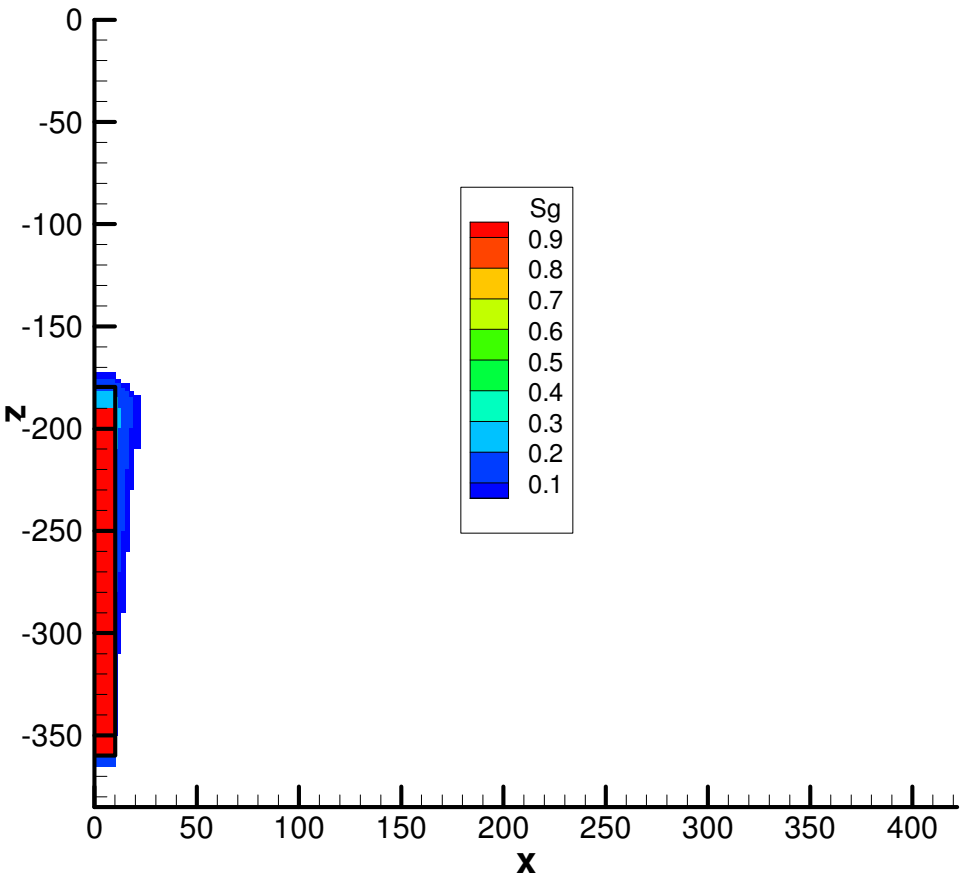

Figure 3.30. Methane gas distribution after 5 years of storage for the 10 microdarcy case.

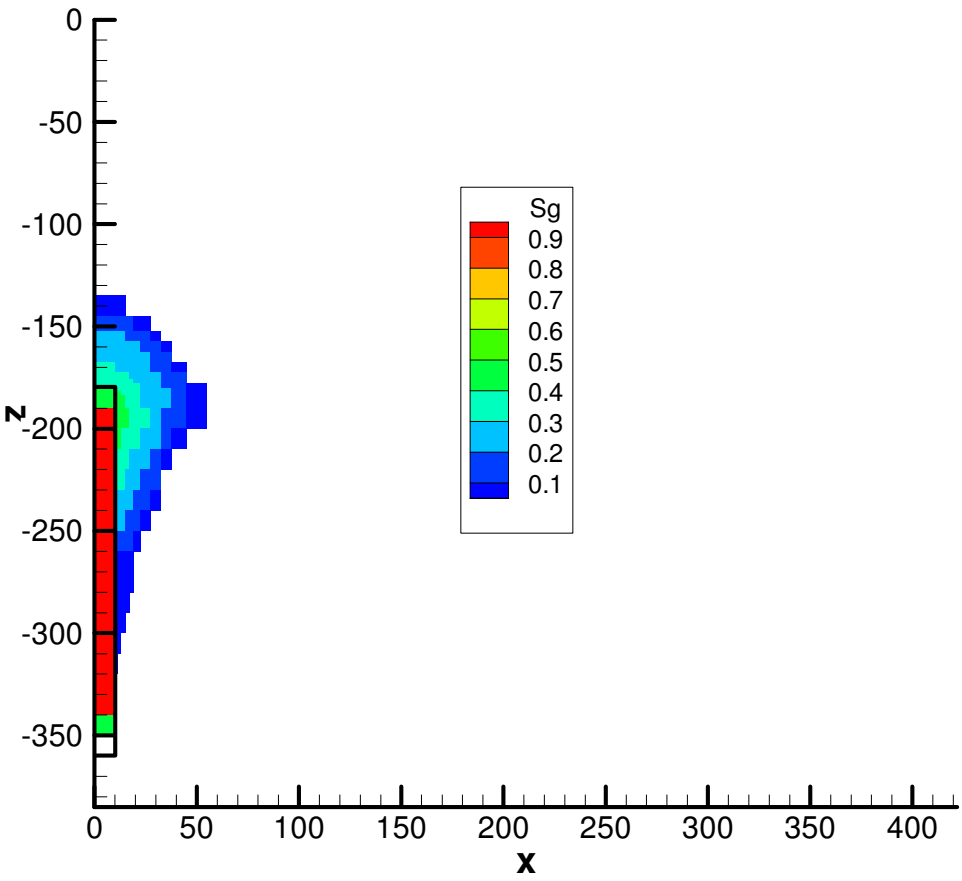

Figure 3.31. Methane gas distribution after 5 years of storage for the 100 microdarcy case.

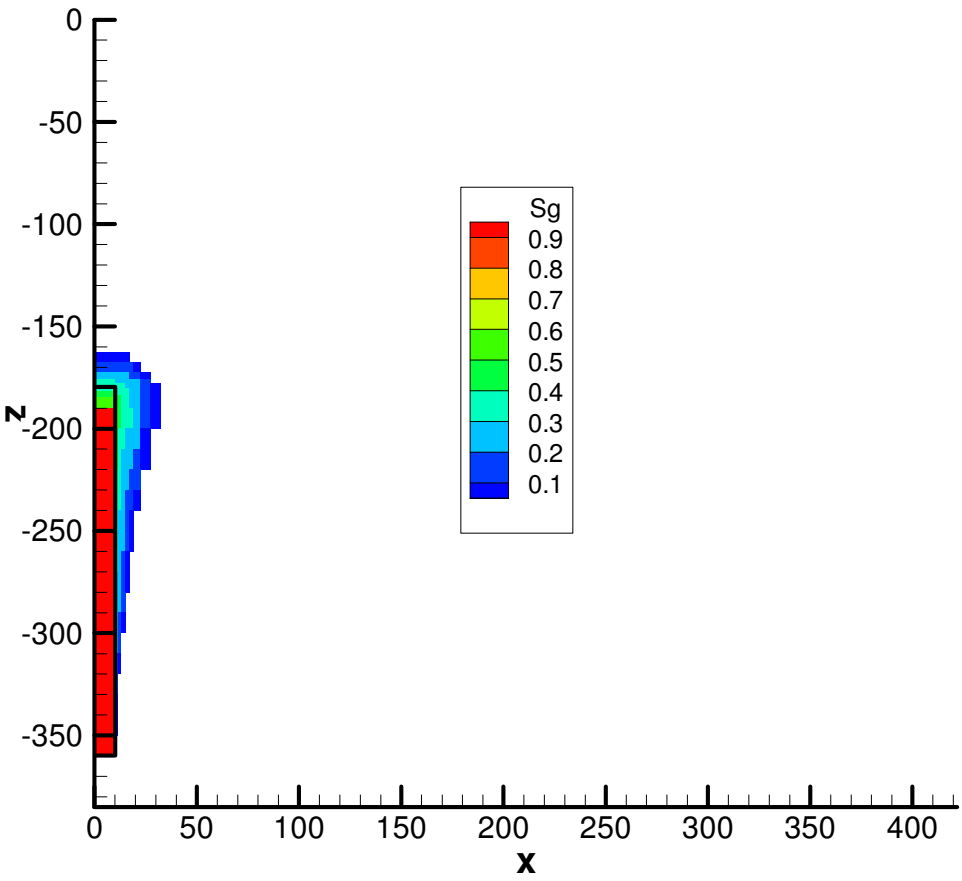

Figure 3.32. Methane gas distribution at the end of the 60 day injection period for the 1 millidarcy case.

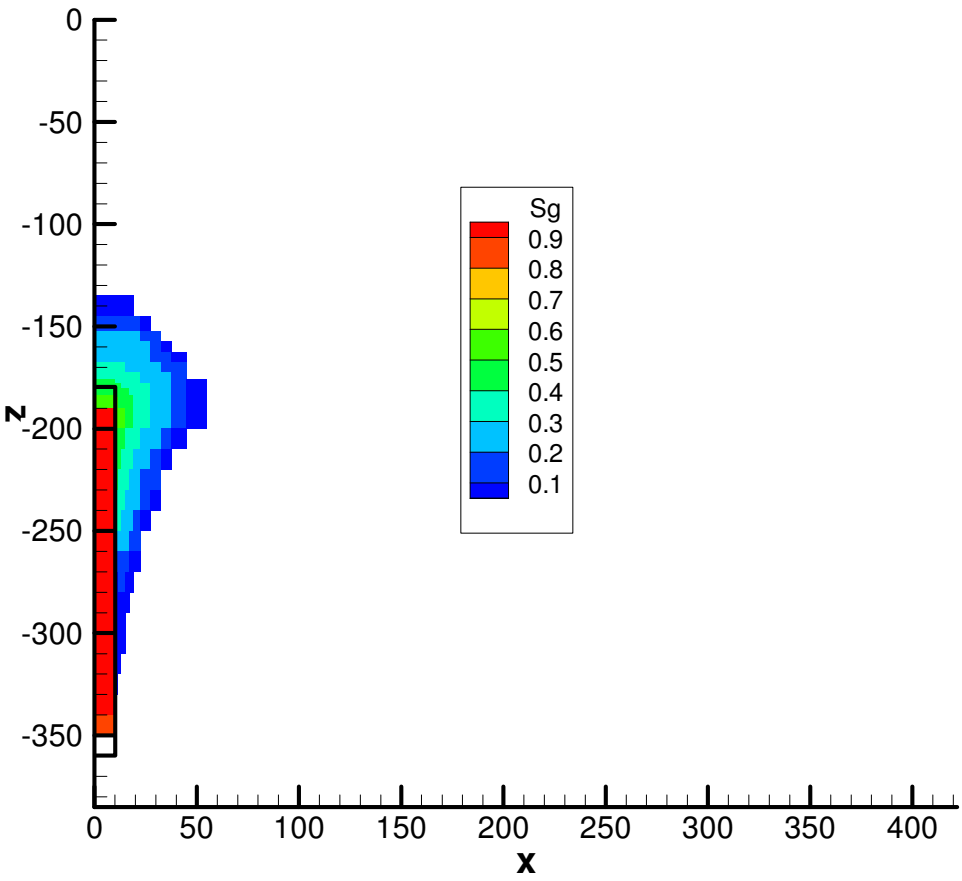

Figure 3.33. Methane gas distribution after 180 days of storage (including the 60 day injection period) for the 1 millidarcy case.

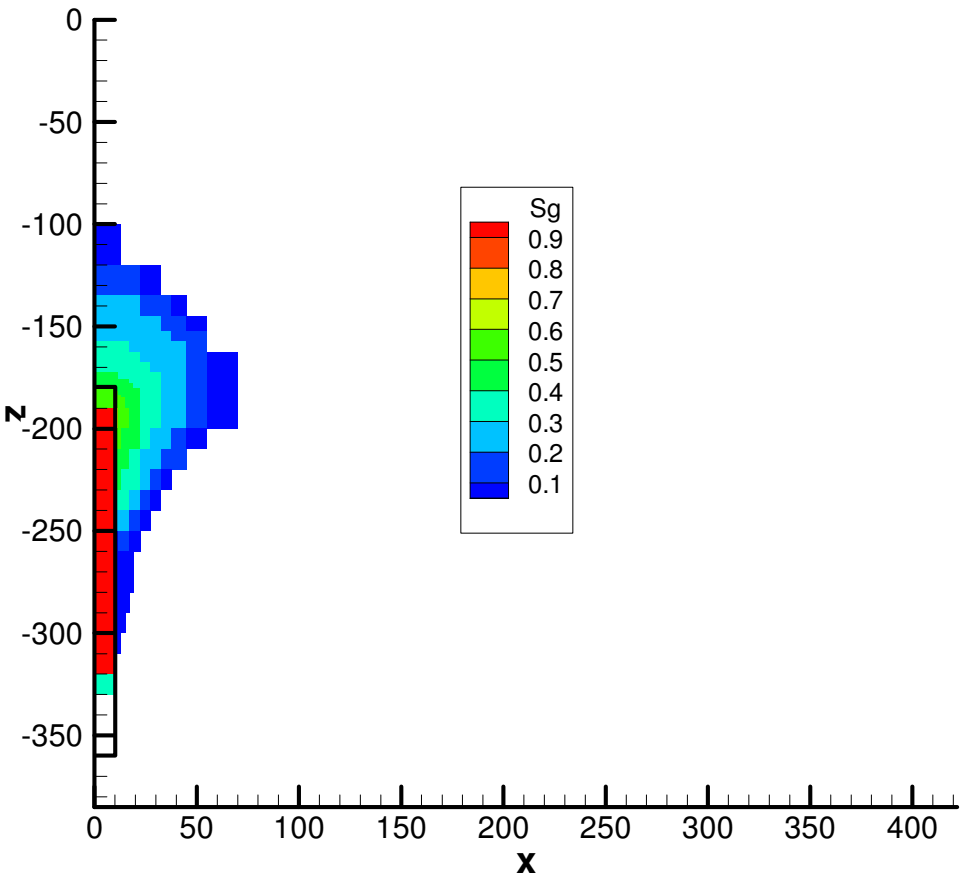

Figure 3.34. Methane gas distribution after 1 year of storage (including the 60 day injection period) for the 1 millidarcy case.

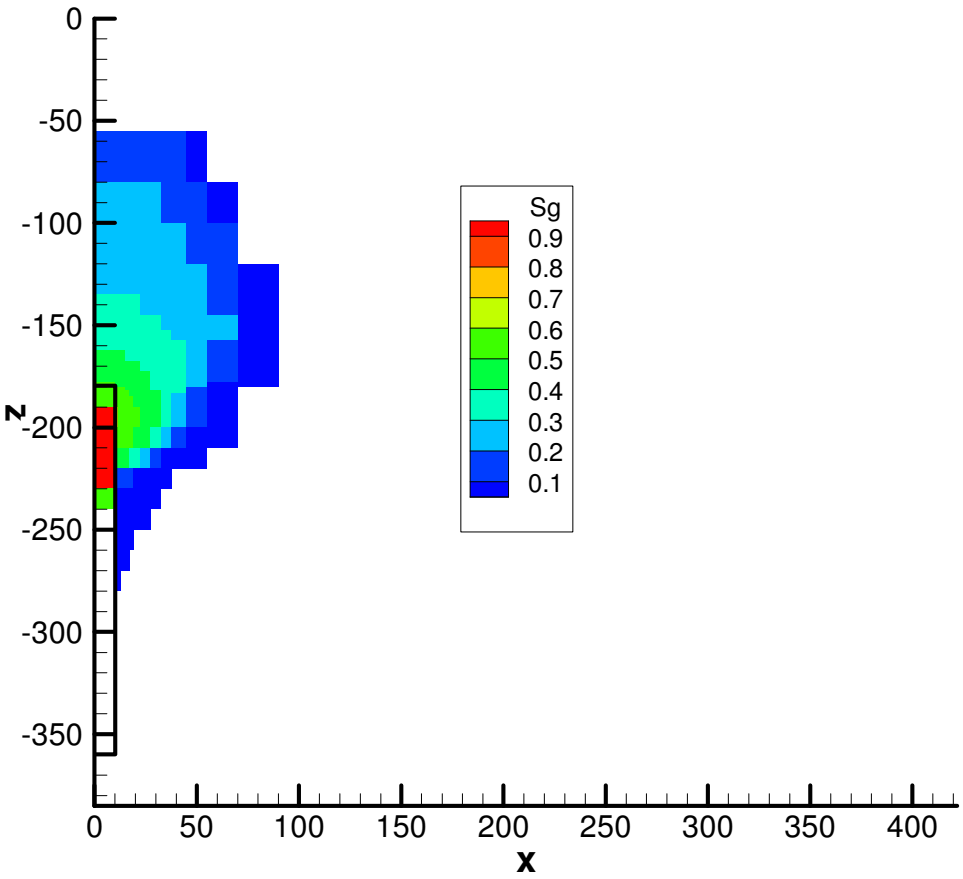

Figure 3.35. Methane gas distribution after 3 years of storage for the 1 millidarcy case.

CONCLUSIONS

The first phase of the project (Budget Period 1) involved preliminary geologic and economic analysis of this new method for creating gas storage. This information contributed to providing an initial assessment of the cost and feasibility of applying the new technology. Hydrochloric acid was determined to be the best acid to use because of low cost, high acid solubility, fast reaction rates with carbonate rock, and highly soluble products (calcium chloride) that allow for the easy removal of calcium waste from the well. A process design was developed for the dissolution process that incorporates proven technologies for drilling wells, storing and pumping acid, and treating the aqueous waste streams exiting the underground storage cavern. A preliminary economic analysis of this design considered capital costs, well-design options and costs, waste treatment options, and comparison with other gas storage costs. Results of this analysis showed that the fracture-acid dissolution method is competitive with other means for creating underground gas storage.

The second phase of the investigation (Budget Period 2), which is the focus of this report, includes analysis and modeling of the processes involved in creating storage capacity, including induced fracturing and acid dissolution of the rock.

Physical and chemical analysis of core samples taken from prospective geologic locations for the acid dissolution process revealed that many of the limestone samples readily dissolved in concentrated hydrochloric acid. Further, some samples contained oily residues that may help to seal the walls of the final cavern structure. These results suggest that there exist carbonate rock formations well suited for the dissolution technology and that the presence of inert impurities had no noticeable effect on the dissolution rate for the carbonate rock.

A sensitivity analysis was performed for characteristics of hydraulic fractures induced in carbonate formations to enhance the dissolution process. A realistic range of physical parameters for Paleozoic limestone formations at 4000 to 8000 ft depth in the northeastern United States was estimated and used to predict the characteristics of fractures that could be created. Multiple fracture simulations were conducted using modeling software that has a fully 3-D fracture geometry package. The simulations, which predict the distribution of fracture geometry and fracture conductivity, show that the stress difference between adjacent beds is the physical property of the formations that has the greatest influence on fracture characteristics by restricting vertical growth. The results indicate that by modifying the fracturing fluid, proppant type, or pumping rate, a fracture can be created with characteristics within a predictable range, which contributes to predicting the geometry of storage caverns created by acid dissolution of carbonate formations.

The TOUGHREACT simulation code was selected as the optimal simulation package to examine the acid dissolution of limestone. A series of three-dimensional simulations were used to investigate three different dissolution configurations: a) injection into an open borehole with production from that same borehole and no fracture; b) injection into an open borehole with production from that same borehole, with an open fracture; and c) injection into an open borehole connected by a fracture to an adjacent borehole from which the fluids are produced. The two-well configuration maximizes the

overall mass transfer from the rock to the fluid, but it results in a complex cavern shape. We have gained useful insights into the acid dissolution process with the TOUGHREACT simulations so far. During the coming year, we will continue to use this code (with appropriate modifications).

The third phase (Budget Period 3) of the project will include modeling field performance, preparing a final design, and performing an economic analysis. The purpose of the final design is to facilitate full-scale deployment of the new technology. Demonstration of the commercialization potential of gas storage in carbonate rocks will open up new geographic areas for developing storage capacity. The technology is expected to have general application to many geographic areas because of the widespread occurrence of carbonate formations.

ACKNOWLEDGEMENTS

We gratefully acknowledge the contributions of individuals at Clemson University who contributed to the project. Jeff Atteberry, graduate research assistant, has provided important geological data, maps, and assessments of the suitability of various carbonate formations. Geoffrey Chambers, graduate research assistant, has contributed significantly to the dissolution modeling work.

We also thank the personnel of the state geological surveys (Indiana, Kentucky, Ohio, Pennsylvania, New York, and West Virginia) from which data have been obtained. In particular, we especially appreciate the time and assistance of the following individuals: Lee Avary (West Virginia Geological Survey), Justin Deming (New York State Museum), John Harper and Cheryl Cozart (Pennsylvania Geological Survey), Dave Harris (Kentucky Geological Survey), and John Rupp (Indiana Geological Survey).

Contributions from the industrial partners (Columbia Natural Resources, Cabot Oil & Gas Corporation, Dominion Transmission, and Halliburton) to this project are gratefully acknowledged. We especially thank John Leeson and Ron Walden (Dominion), Ed Rothman (CNR), John Abshire (Cabot), and Gary Rodvelt and Greg Kozera (Halliburton) for their interest, time, and many helpful suggestions.

We thank Anthony Zammerilli, USDOE, for his many helpful suggestions and interest in the project.

REFERENCES CITED

Advani, S. H., Lee, J. K. and Khattab, H., 1985, Hydraulic Fracture Geometry Modeling, Prediction, and Comparisons: Low Permeability Gas Reservoirs, p. 135-139. Paper SPE 13863.

Advantek, 2004, Advantek International: advanced solutions for reservoir geomechanics, completions, stimulation, http://www.advantekinternational.com/

Anderson, R. W., Cooke Jr., C. E. and Wendorff, C. L., 1989, Propping Agents and Fracture Conductivity, in J. L. Gidley, S. A. Holditch, D. E. Nierode and R. W. J. Veatch, eds., Recent Advances in Hydraulic Fracturing: Richardson, TX, Society of Petroleum Engineers, p. 109-146.

Angus, S.; Armstrong, B.; de Reuck, K.M., 1976, International Thermodynamic Tables of the Fluid State: Carbon Dioxide, Int. Union of Pure and Applied Chemistry, Pergamon Press: Oxford.

Atkinson, B. K. and Meredith, P. G., 1987, Experimental Fracture Mechanics Data for Rocks and Minerals, in B. K. Atkinson, ed., Fracture Mechanics of Rock: London, Harcourt Brace Jovanovich, p. 477-525.

Baidyuk, B. V. e., 1967, Mechanical properties of rocks at high temperatures and pressures: New York, Consultants Bureau, 75 p. p.

Benson, A., 2004, Stimlab Division GOHFER, Core Laboratories, http://www.corelab.com/stimlab/Depts/GOHFER_prodinfo.asp

Carter, R. D., 1957, Derivation of the General Equation for Estimating the Extent of the Fractured Area, Appendix to Optimum Fluid Characteristics For Fracture Extension, by G.C. Howard and C.R. Fast: Drilling and Production Pratice, API 261-270.

Castle, J. W., Bruce, D., Falta, R. W., Murdoch, L., Brame, S. E., and Brooks, D., 2004a, Fracture Dissolution of Carbonate Rock: An Innovative Process for Gas Storage: Topical Report (Budget Period One), DE-FC26-02NT41299, March 5, 2004, 163 p.

Castle, J. W., Bruce, D. A., Brame, S. E., Brooks, D. A., Falta, R. W. and Murdoch, L. C., 2004b, Design and Feasibility of Creating Gas-Storage Caverns by Using Acid to Dissolve Carbonate Rock Formations: SPE Eastern Regional Meeting, Society of Petroleum Engineers, Paper SPE 91436, 10 p.

CFCFF, 1996, Rock Fractures and Fluid Flow: Contemporary Understanding and Applications: Washington, D.C, National Academy Press. http://www.netlibrary.com/urlapi.asp?action=summary&v=1&bookid=750

Chen, M. and Zhang, G.-q., 2004, Laboratory measurement and interpretation of the fracture toughness of formation rocks at great depth: Journal of Petroleum Science and Engineering, v. 41, p. 221-231.

Clark, J. B., 1949, A Hydraulic Process for Increasing the Productivity of Wells: Trans. AIME, v. 186 1-8.

Clifton, R. J., 1989, Three-Dimensional Fractrue-Propagation Models, in J. L. Gidley, S. A. Holditch, D. E. Nierode and R. W. J. Veatch, eds., Recent Advances in Hydraulic Fracturing: Richardson, TX, Society of Petroleum Engineers, p. 95-108.

Coates, D. F., 1970, Rock mechanics principles: Ottawa, Information Canada, 1 v. (various pagings) p.

De Laguna, W., 1966, Disposal of radioactive wastes by hydraulic fracturing, Part I: General concept and first field experiments: Nuclear Engineering and Design, v. 3 338-352.

Economides, M. J. and Boney, C., 2000, Reservoir Stimulation in Petroleum Production, in M. J. Economides and K. G. Nolte, eds., Reservoir Stimulation: Chinchester, England, John Wiley & Sons, LTD, p. 1.1-1.30.

Economides, C., Harrison, D. and Jones, L., 2004, Oilfield Glossary, Schlumberger http://www.glossary.oilfield.slb.com/Display.cfm?Term=fracture%20conductivity

EIA, 2004, The Basics of Underground Natural Gas Storage, Energy Infromation Administration, Washington, D.C., http://www.eia.doe.gov/pub/oil_gas/natural_gas/analysis_publications/storagebasics/storagebasics.html

EPA, 1997, Analysis of Selected Enhancemants for Soil Vapor Extraction: Office of Solid Waste and Emergency Response, v. EPA/542/R/97/007.

Falta, R.W., 2000, Numerical Modeling of Kinetic Interphase Mass Transfer During Air Sparging Using a Dual-Media Approach, Water Resources Research, Vol., 36, No. 12, 3391-3400.

Falta, R.W., L.C. Murdoch, and G.K. Chambers, 2004, Fracture Dissolution of Carbonate Rock: An Innovative Process for Gas Storage, Review of Current Technology for Acid Dissolution and Hydraulic Fracturing (Task 5), Report Submitted to DOE, February 28, 2004.

Falta, R.W., K. Pruess, S. Finsterle, and A. Battistelli, T2VOC User's Guide, *Lawrence* Berkeley Laboratory Report LBL-36400, March, 1995

Geertsma, J. and De Klerk, F., 1969, Rapid Method of Predicting Width and Extent of Hydraulically Induced Fractures, v. 21 (12), p. 1571-81.

Goodman, R. E., 1980, Introduction to rock mechanics: New York, Wiley, xii, 478 p.

Gregorowicz, J., Peters, C. J., de Swaan Arons, J., Friedrichs, G. and Jaeschke, M., 1996, Phenomena related to the storage of natural gas in underground caverns: Fluid Phase Equilibria, v. 117 (1-2), p. 249-256.

Hatheway, A. W. and Kiersch, G. A., 1989, Engineering Properties of Rock, in R. S. Carmichael, ed., Pratical Handbook of Physical properties of Rocks and Minerals: Boca Raton, FL, CRC Press.

Hoffman, E. L., 1993, Effects of Cavern Spacing on the Performance and Stability of Gas-Filled Storage Caverns, SAND92-2545, Sandia National Laboratories, Albuquerque, NM.

Horton, A. I., 1981, A comparative analysis of stimulations in the Eastern Gas Shales: Morgantown, WV, Department of Energy.

Hu, X. and Nied, H. F., 2003, FRAC3D-Finite Element Based Software for 3-D and Generalized Plane Strain Fracture Analysis: Bethlehem, PA, Mechanical Engineering and Mechanics Department, Lehigh University, 59 p.

Khristianovic, S. A. and Zheltov, Y. P., 1955, Formation of vertical fractures by means of highly viscous liquid, Proceedings of the 4th World Petroleum Congress, v. 2: Rome, p. 579-586.

Lacy, L. L. and Smith, M. B., 1989, Fracture Azimuth and Geometry Determination, in J. L. Gidley, S. A. Holditch, D. E. Nierode and R. W. J. Veatch, eds., Recent Advances in Hydraulic Fracturing: Richardson, TX, Society of Petroleum Engineers, p. 341-356.

Mack, M. G. and Warpinski, N. R., 2000, Mechanics of Hydraulic Fracturing, in M. J. Economides and K. G. Nolte, eds., Reservoir Stimulation: Chichester, England, John Wiley & Sons, LTD, p. 6.1-6.49.

Marketec, B. A., 2005, Oilfield Glossary, Schlumberger, http://www.glossary.oilfield.slb.com/default.cfm.

Matsuki, K., 1989, Size effect and size requirement in fracture toughness evaluation of rock, in H. Mihashi, H. Takahashi and F. H. Wittmann, eds., Fracture Toughness and Fracture Energy: Rotterdam, A.A. Balkema, p. 287-303.

McVey, D. S., Mohaghegh, S., Aminian, K. and Ameri, S., 1996, Identification of parameters influencing the response of gas storage wells to hydraulic fracturing with the aid of a neural network.: SPE Computer Applications Journal, v. Apr. 54-57.

Mendelsohn, D. A., 1984a, A Review of Hydraulic Fracture Modeling-Part I: General Concepts, 2D Models, Motivation fro 3D Modeling: Journal of Energy Resources Technology, v. 106 (3), p. 369-376.

Mendelsohn, D. A., 1984b, A Review of Hydraulic Fracture Modeling-II: 3D Modeling and Vertical Crack Growth in Layered Rock: Journal of Energy Resources Technology, v. 106 (4), p. 543-553.

Meredith, P. G., 1989, Comparative fracture toughness testing of rocks, in H. Mihashi, H. Takahashi and F. H. Wittmann, eds., Fracture Toughness and Fracture Energy: Rotterdam, A.A. Balkema, p. 265-277.

Miller II, W. K. and Smith, M. B., 1989, Reanalysis of the MWX Fracture Stimulation Data From the Paludal Zone of the Mesaverde Formation: 64th Annual Technical Conferene and Exhibition of the Society of Petroleum Engineers, p. 671-680. Society of Petroleum Engineers, Paper SPE 19772.

Mohaghegh, S., Balanbb, B., Platonc, V. and Ameria, S., 1999, Hydraulic fracture design and optimization of gas storage wells: Journal of Petroleum Science and Engineering, v. 23 (3-4), p. 161-171.

Murphy, H., 1983, Hot Dry Rock Reservoir Development and Testing in the USA, in S. Nemat-Nasser, H. Abe and S. Hirakawa, eds., Hydraulic fracturing and geothermal energy: The Hague, Martinus Nijhoff Publishers, p. 33-58.

Nathenson, M. and Guffanit, M., 1988, Geothermal Gradients in the Conterminous United States: Journal of Geophysical Research, v. 93 (B6), p. 6437-6450.

Nemat-Nasser, S., 1983, Thermally Induced Cracks and Heat Extraction From Hot Dry Rocks, in S. Nemat-Nasser, H. Abe and S. Hirakawa, eds., Hydraulic fractureing and geothermal energy: The Hague, Martinus Nijhoff Publishers, p. 11-31.

Nolte, K. G., 2000, Appendix: Evolution of Hydraulic Fracturing Design and Evaluation, in M. J. Economides and K. G. Nolte, eds., Reservoir Stimulation: Chinchester, England, John Wiley & Sons, LTD, p. A5.1-A5.22.

Nordgren, R. P., 1972, Propagation of a vertical hydraulic fracture: Society of Petroleum Engineers Journal 306-314.

NSI, 2004, NSI Fracturing Technologies Inc., http://www.nsitech.com/

NSI, 2004b, StimPlan Users manual, NSI Technologies Inc., Tulsa Okalahoma

Ouchterlony, F., 1989, Fracture toughness testing of rock with core based specimens, the development of an ISRM standard, in H. Mihashi, H. Takahashi and F. H. Wittmann, eds., Fracture Toughness and Fracture Energy: Rotterdam, A.A. Balkema, p. 231-251.

Pearson, C. M., 1982, Exploitation of Hot Dry Rock Geothermal Energy in the United Kingdom: International Journal of Ambient Energy, v. 3 19-26.

Perkins, T. K. and Kern, L. R., 1961, Widths of Hydraulic Fractures: Journal of Petroleum Technology (September), p. 937-949.

Pruess, K., 1991, TOUGH2: A general numerical simulator for multiphase fluid and heat flow, Lawrence Berkelely National Lab. Report LBL-29400, Berkeley, CA.

Pruess, K., and A. Battistelli, 2002, TMVOC, A Numerical Simulator for Three-Phase Non-Isothermal Flows of Multicomponent Hydrocarbon Mixtures in Saturated-Unsaturated Heterogeneous Media, Lawrence Berkeley National Laboratoroy Report LBNL-49375, 192 p.

Pruess, K., and J. Garcia, 2002, Multiphase flow dynamics during CO_2 disposal into saline aquifers, Environmental Geology, Vol. 42, 282-295.

Queipoa, N. V., Verdea, A. J., Canelónb, J. and Pintos, S., 2002, Efficient global optimization for hydraulic fracturing treatment design: Journal of Petroleum Science and Engineering, v. 35 (3-4), p. 151-166.

Randolph, P. L., 1976, Pinedale Unit MHF Experiments: ERDA Symposium on Enhanced Oil & Gas Recovery, p. E-2/1-31. The Petroleum Publishing Company.

Ranostaj, E. J., 1976, Massive Hydraulic Fracturing the Eastern Devonian Shales: ERDA Symposium on Enhanced Oil & Gas Recovery, p. C-3/1-11. The Petroleum Publishing Company.

Robertson, E. C., 1959, Physical Properties of Limestone and Dolomite Cores from the Sandhill Well, Wood County, West Virginia, Charleston, West Virginia Geological Society, p. 112-144.

Rummel, F., 1987, Fracture Mechanics Approach to Hydraulic Fracturing Stress Measurements, in B. K. Atkinson, ed., Fracture Mechanics of Rock: Orlando, Academic Press Inc., p. 217-239.

Saberian, A., and Podio, A. L., 1977, A Computer Model for Describing the Development of Solution-Mined Cavities. IN SITU, V. 1, n. 1, pp 1-36.

Schlumberger, 2004, Schlumberger Information Solutions, FracCADE, http://www.sis.slb.com/content/software/production/fraccade.asp

Schmidt, R. A., 1976, Fracture-toughness Testing of Limestone: Experimental Mechanics, v. 16 (5), p. 161-167.

Settari, A., 2004, Personal Communication

Shumbera, D. A., Ellis, R. C. and Loya, D., 2003, Design and Long-Term Production Performance of Frac Pack Completions in a Gulf of Mexico Deepwater Turbidite Field Having Inverted Sand-Shale Stress Contrasts: Case History: SPE Annual Technical Conference and Exhibition, Proceedings-Mile High Meeting of the Minds, Oct 5-8 2003, Denver, CO, United States, p. 1789-1796. Society of Petroleum Engineers, Paper SPE 84259.

Smith, M. B., Miller II, W. K. and Haga, J., 1987, Tip Sreenout Fracturing: A Technique for Soft, Unstable Formations: Paper SPE 13273.

Smith, M. B. and Shlyapobersky, J. W., 2000, Basics of Hydraulic Fracturing, in M. J. Economides and K. G. Nolte, eds., Reservoir Stimulation: Chichester, England, John Wiley & Sons, LTD, p. 5.1-5.28.

Smith, M. B., 2004a, Personal Communication

Somerton, W. H., Esfandiari, F. and Singhal, A., 1969, Further Studies of the Relation of Physical Properties of Rock to Rock Drillability: Fourth Conference on Drilling and Rock Mechanics. Society of Petroleum Engineers of AIME.

Spycher, N. F.; Reed M.H., 1988, Fugacity Coefficients of H2, CO2, CH4, H2O, and of H2O-CO2-CH4 mixtures: A Virial Equation Treatment for Moderate Pressures and Temperatures Applicable to Calculations of Hydrothermal Boiling, Geochimica et Cosmochimica Acta, 52, 739-749.

Stow, S. H., Haase, S. and Weeren, H. O., 1985, Waste Disposal by hydrofracture and application of the technology to the management of hazardous wastes, Proceedings of the International Conference in New Frontiers in Hazardous Waste Management, EPA/600/9-85/025, p. 138-144.

Terratek, 2004, TerraFRAC; A Three-Dimensional Hydraulic Fracturing System, http://www.terratek.com/

Thiercelin, M. C. and Roegiers, J.-C., 2000, Formation Characterization: Rock Mechanics, in M. J. Economides and K. G. Nolte, eds., Reservoir Stimulation: Chichester, England, John Wiley & Sons, LTD, p. 3.1-3.35.

Veatch, R. W. J. and Crowell, R. F., 1982, Joint Research/Operations Programs Accelerate Massive Hydraulic Fracturing Technology: Journal of Petroleum Technology, v. 34 (12), p. 2763-2775.

Veatch, R. W. J., 1983a, Overview of Current Hydraulic Fracturing Design and Treatment Technology-Part 1: Journal of Petroleum Technology, v. 35 (4), p. 677-687.

Veatch, R. W. J., 1983b, Overview of Current Hydraulic Fracturing Design and Treatment Technology-Part 2: Journal of Petroleum Technology, v. 35 (May), p. 853-864.

Veatch, R. W. J., Moschovidis, Z. A. and Fast, R. C., 1989, An Overview of Hydraulic Fracturing, in J. L. Gidley, S. A. Holditch, D. E. Nierode and R. W. J. Veatch, eds., Recent Advances in Hydraulic Fracturing: Richardson, TX, Society of Petroleum Engineers, p. 1-38.

Warpinski, N. R., 1989, Determining the Minimum in situ Stress from Hydraulic Fracturing through Perforations: International Journal of Rock Mechanics and Mining Sciences & Geomechanics Abstracts, v. 26 (6), p. 523-531.

Warpinski, N. R., Moschovidis, Z. A., Parker, C. D. and Abou-Sayed, I. S., 1994, Comparison study of hydraulic fracturing models - test case: GRI staged field experiment No. 3: SPE Production & Facilities, v. 9 (1), p. 7-16.

Whitehead, W. S., Gatens III, J. M. and Holditch, S. A., 1989, Determination of In Situ Stress Profiles Through Hydraulic Fracturing Measurements in Two Distinct Geologic Areas: International Journal of Rock Mechanics and Mining Sciences & Geomechanics Abstracts, v. 26 (6), p. 637-645.

Williams, B. B., Gidley, J. L., and Schechter, R. S., 1979, Acidizing Fundamentals. Soc. Pet. Eng., Richardson, TX, 124 pages.

Wolff, R. G., Bredehoeft, J. D., Keys, W. S. and Shuter, E., 1974, Stress Determination by Hydraulic Fracturing in Subsurface Waste Injection: Journal of American Water Works Association, v. 67 519-523.

Wu, M. and Wang, H. F., 1988, Influence of Nearby Fractures on Stress Measurements by Hydraulic Fracturing: International Journal of Rock Mechanics and Mining Science & Geomechanics Abstracts, v. 25 (1), p. 15-23.

Xu, T., J.A. Apps, and K. Pruess, 2003a, Reative geochemical transport simulation to study mineral trapping for CO_2 disposal in deep aranaceous formations, Journal of Geophysical Research, Vol. 108, No. B2, 2071, p. ECV 3-1 – ECV 3-13.

Xu, T., Pruess, K., and Brimhall, G., 1999, An Improved Equilibrium-Kinetics Speciation Algorithm for Redox Reactions in Variably Saturated Subsurface Flow Systems. Computers & Geosciences, v 25, p 655-666.

Xu, T., E. Sonnenthal, N. Spycher, and K. Pruess, 2003b, TOUGHREACT: A new code of the TOUGH family for non-isothermal multiphase reactive geochemical transport in variably saturated geologic media, Proceedings, TOUGH Symposium 2003, Lawrence Berkeley National Laboratory, Berkeley, CA, May 12-14, 2003.

Xu, T., E. Sonnenthal, N. Spycher, and K. Pruess, 2004, TOUGHREACT User's Guide: As Simulation Program for Non-isothermal Multiphase Reactive Geochemical Transport in Variably Saturated Geologic Media, Lawrence Berkeley National Laboratory Report LBNL/PUB-3179, 192p.

Yeager, V. J. and Shuchart, C. E., 1997, Acidizing gas storage wells: SPE Eastern Regional Conference and Exhibition, p. 113-124. Society of Petroleum Engineers, Paper SPE 39225.

LIST OF ACRONYMS, ABBREVIATIONS, AND SYMBOLS

#fm	pounds foam
°C	Degrees Celsius
°C/km	Degrees Celsius divided by kilometers
°F	Degrees Fahrenheit
°F/mile	Degrees Fahrenheit divided by miles
2D	Two Dimensional
3D	Three Dimensional
A_{C-R}	interfacial area of the cavern-rock interface
aq	aqueous solution
Avg	Average
b	fracture aperture
BHFP	Bottom Hole Flowing Pressure
BL	Baseline
BL	Bounding Layers
BPM	Barrels per minute
cP	centipoises
$C_{w,C}$	salt concentration in the open cavern element
$C_{w,R}$	salt concentration in the rock element
D’	diffusion-like fitting parameter
d_{C-R}	average distance from cavern gridblock to rock gridblock
E'	modulus (plane strain modulus)
E	Young's modulus
frac	Fracture
ft	feet
ft√min	feet multiplied by the square root of minutes
g	grams
in	inches
Int	Intermediate
k_f	fracture permeability
Kg	Kilograms
KGD	Khristianovich-Geertsma-de Klerk model
K_{IC}	fracture toughness
K-Ic	fracture toughness
K_o	poro-elastic formation constant
k_{rock}	rock intrinsic permeability
k_{rw}	relative permeability of the aqueous phase
k_w	aqueous phase permeability
L,l	Liter
lbm	pounds
LS	Limestone
m	meters
md	Millidarcy
md-ft	Millidarcy feet

Mgal	1000 Gallons
MHF	Massive Hydraulic Fracture
min	minutes
MLbs	1000 pounds
Mpsi	1000 pounds per square inch
P	Pressure
P3D	Psudo-Three Dimensional
Pa	Pascal
Pa-s	Pascal seconds
PC	Pre-cured
PKN	Perkins-Kern-Nordgren model
P-net	Net Pressure
PPG	pounds of proppant per fluid gallon
PR	Pumping Rate
P_{res}	reservoir pressure
psi	pounds per square inch
psi/ft	pounds per square inch divided by feet
psi√in	pounds per square inch multiplied by the square root of inches
PXD	Powder X-ray diffraction
Q	Quality
Q_{C-R}	rate of mass transfer of rock into solution
R	ideal gas constant
RC	Resin Coated
s	seconds
SD	Stress Difference
S_r	volumetric saturation used to represent fraction of undissolved rock
Std. Dev.	Standard Deviation
S_w	water saturation
T	Temperature
T_f	fracture transmissivity
T_m	equivalent gridblock transmissivity
TSO	Tip Screen Out
TVD	Total Vertical Depth
X-link	Cross Linked
Z_{CO_2}	Compressibility factor for CO_2
ϕ	Fugacity coefficient
γ_i	Thermodynamic activity coefficient for species *i*
ν	Poisson's Ratio
σ_{cl}	closure presure
σ_v	overburden pressure